OPTICAL PROPERTIES OF NANOPARTICLE DECORATED GOLD NANORODS AND CARBON NANOTUBES

THESIS SUBMITTED TO
THE COCHIN UNIVERSITY OF SCIENCE AND TECHNOLOGY
IN PARTIAL FULFILMENT OF THE REQUIREMENTS FOR THE
DEGREE OF DOCTOR OF PHILOSOPHY
IN CHEMISTRY UNDER THE FACULTY OF SCIENCE

By

PRAMOD P.

UNDER THE SUPERVISION OF
Dr. K. GEORGE THOMAS

PHOTOSCIENCES AND PHOTONICS
CHEMICAL SCIENCES AND TECHNOLOGY DIVISION
NATIONAL INSTITUTE FOR INTERDISCIPLINARY SCIENCE AND TECHNOLOGY (CSIR)
TRIVANDRUM - 695019
KERALA, INDIA

APRIL 2008

Dedicated To...

My Beloved Parents,

Teachers and Friends

STATEMENT

I hereby declare that the matter embodied in the thesis entitled, *"Optical Properties of Nanoparticle Decorated Gold Nanorods and Carbon Nanotubes"* are results of investigations carried out by me at the Photosciences and Photonics Section, Chemical Sciences and Technology Division of the National Institute for Interdisciplinary Science and Technology (CSIR), Trivandrum, under the supervision of Dr. K. George Thomas and the same has not been submitted elsewhere for a degree.

In keeping with the general practice of reporting scientific observations, due acknowledgement has been made wherever the work described is based on the findings of other investigators.

Pramod P.

i

April 10, 2008

CERTIFICATE

This is to certify that the work embodied in the thesis entitled, *"Optical Properties of Nanoparticle Decorated Gold Nanorods and Carbon Nanotubes"* has been carried out by Mr. Pramod P. under my supervision and the same has not been submitted elsewhere for a degree.

K. George Thomas

Thesis Supervisor

ii

ACKNOWLEDGEMENTS

iii

Pramod P.

CONTENTS

Page

Chapter 1. *Zero and One Dimensional Nanomaterials: An Overview*

Chapter 2. *Synthesis and Photophysical Properties of Ruthenium Trisbipyridine Functionalized Gold Nanoparticles*

Chapter 3. *Gold Nanoparticle Decorated Carbon Nanotubes for Light Induced Electron Transfer*

Chapter 4. Exploring the Edge Effects in Gold Nanorods

viii

PREFACE

Nanoscience and nanotechnology pertain to the synthesis, characterization and integration of materials which possess at least one of its dimensions in the nanometer scale (1-100 nm) and their utilization in devices. Materials in the nanoscale regime consist of a collection of few atoms or molecules, whose properties are distinctly different from that of the bulk system. Nanostructured materials thus constitute a bridge between single atoms/molecules and bulk systems and their novel properties originate from the confinement of electrons in this size regime. The main objectives of the present investigation is to explore (i) the photophysical properties of functionalized gold nanoparticles, (ii) their integration on to Au nanorods and single walled carbon nanotubes and (iii) probing the unique properties of the heterojunctions of these hybrid materials.

The thesis consists of four chapters. The first section of Chapter 1 provides an overview on zero dimensional nanomaterials such as Au nanoparticles and one dimensional nanomaterials (Au nanorods and carbon nanotubes). The second section of this Chapter provides an overview on the use of these nanostructured materials for various opto-electronic and biological applications.

The Chapter 2 presents a convenient method for the synthesis of nanohybrid systems possessing ruthenium trisbipyridine ($Ru(bpy)_3^{2+}$) chromophores on the surface of gold nanoparticles. $Ru(bpy)_3^{2+}$ chromophores were functionalized on to the surface of Au nanoparticles through place exchange reaction. The photophysical properties of these hybrid materials were tuned by varying the concentration of $Ru(bpy)_3^{2+}$ chromophores. Based on the steady-state and time-resolved investigations, a charge shift between the excited and ground state $Ru(bpy)_3^{2+}$ chromophores were observed leading to the formation of redox products. The electron transfer products were found to be stable for several nanoseconds, probably due to the stabilizing effect of the polar ethylene glycol moieties embedded between the chromophoric groups. Interestingly at lower concentrations of the chromophores, the emission properties of $Ru(bpy)_3^{2+}$ were retained on gold nanoparticles and no electron transfer products were observed.

ix

The modified electronic properties at the heterojunctions of Au nanoparticle decorated single walled carbon nanotubes (SWNT) have been utilized for photoinduced electron transfer and details are presented in Chapter 3. $Ru(bpy)_3^{2+}$ chromophores were linked on to single walled carbon nanotubes directly (SWNT-Ru^{2+}) and through Au nanoparticles (SWNT-Au-Ru^{2+}) and various light induced processes in these systems were investigated using steady-state and time-resolved techniques. A unidirectional electron flow was observed from the excited state of $Ru(bpy)_3^{2+}$ to carbon nanotubes when the chromophores were linked through Au nanoparticles. In contrast, photoinduced electron transfer was not observed from *$Ru(bpy)_3^{2+}$ to SWNT when these components were linked directly. The charge equilibration at the SWNT-Au heterojunctions, due to the differences in electrochemical potentials, result in the formation of a localized depletion layer on SWNT which may act as acceptor sites of electrons from the excited state of $Ru(bpy)_3^{2+}$.

The Chapter 4 deals with the edge effects in Au nanorods and their organization with nanoparticles/nanorods through electrostatic and covalent approaches. It was observed that the zeta potential of Au nanorods vary from high positive value in water to high negative value in H_2O-CH_3CN mixtures. Bathochromic shift in the longitudinal plasmon band of Au nanorods was observed on addition of Au nanoparticles whereas the transverse plasmon band remains unaffected. The enhanced negative potential at the edges of Au nanorods preferentially attracts the functionalized nanoparticles having positive zeta values, leading to their selective assembly in the longitudinal direction. The ability of thiol molecules to preferentially react with the [111] facets of Au nanorods was utilized for assembling them into one dimensional chains. Plasmon coupling in dimers of Au nanorods was investigated as a function of their orientation using a flexible (C_6DT) as well as rigid (PDT) linker groups. The plasmon coupling in PDT linked Au nanorod dimers is found to be more pronounced due to effective dipolar overlap along their long axes. Based on these studies it is concluded that the orientation between the nanorods plays a crucial role in plasmon coupling which can be modulated by varying the nature of the linker group.

CHAPTER 1

Zero and One Dimensional Nanomaterials: An Overview

1.1. An Introduction to Nanostructured Materials

Nanoparticles, nanostructures, nanoscience, nanotechnology .... are now some of the most widely used terms not only among scientific community but also in the discussions of common man. Nanoscience and nanotechnology pertain to the synthesis, characterization, exploration and utilization of materials, which possess at least one of its dimensions in the nanometer range (~1-100 nm). Then an obvious question arises: why are materials and processes in nanoscale so attractive? The materials in nanometer scale incorporate collections of atoms or molecules, whose properties are distinctly different from those of isolated atoms/molecules or bulk systems.[1-9] Thus, nanostructured materials constitute a bridge between single atoms/molecules and bulk systems. The newer properties at the nanoscale mainly arise from the confinement of electrons that do not scale linearly with size. The fascinating properties of nanostructured materials mainly depend on their size and shape, rather than the chemical composition.[1-9] Hence, reliable and continual changes in their properties can be achieved by manipulation of a single material. Some of the examples of nanostructured materials include metal and semiconductor

nanoparticles and nanostructured carbon based systems such as fullerenes, single and multi-walled carbon nanotubes. The noble metal nanoparticle based systems possess an attractive property: strong optical absorption arising from the surface plasmon resonance (yellow, red and blue color for Ag, Au and Cu, respectively). The larger surface to volume ratio is yet another unique feature of nanostructured materials which make them a suitable candidate in catalytic processes.

The underlying theme of nanoscience and nanotechnology is the building of functional materials and devices through the assembly of molecular and nanostructured components (bottom-up approach), as proposed in the visionary lecture by Richard Feynman in 1959,[10] titled as "*There's plenty of room at the bottom*". In the last 5-10 years, several synthetic protocols have been developed for the design of highly monodisperse nanoparticles with extreme control over size.[4-9] For example, monodisperse iron oxide nanoparticles in the size range of 6-13 nm, with continuous increments of 1 nm have been reported by Hyeon and coworkers (Figure 1.1).[11] Newer methods of characterization of nanoparticles based on electron and probe microscopic methods have enabled better understanding of their crystallographic properties.[12] Spectroscopic methods have been widely used for understanding the optical properties of these materials. Thus, our ability to construct nanostructured systems through atom by atom or molecule by molecule organization with high precision enabled the design of newer materials with diverse functionality and dimensionality (0D, 1D, 2D and 3D).
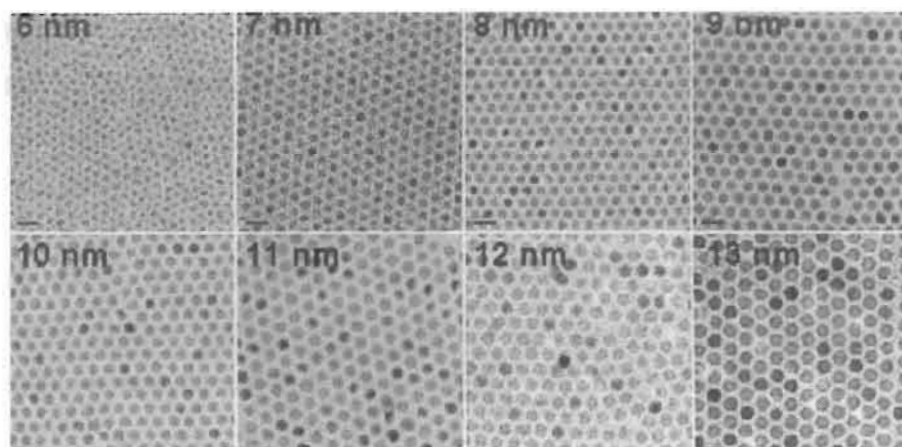
Figure 1.1. Transmission electron micrographs of iron oxide nanoparticles showing 1 nm increments in size (*adapted from reference 11*).

The synthesis, characterization and investigation of the properties of various nanomaterials are well documented as reviews.[4-9] In this thesis, three different nanomaterials, namely Au nanoparticles, Au nanorods and single walled carbon nanotubes are used as components for the design of hybrid nanostructures. In subsequent sections of Chapter 1, a brief overview on the synthesis and properties of these nanostructured materials is presented.

1.2. Gold Nanoparticles

Spherical gold nanoparticles are one of the most widely studied nanomaterials, mainly due to their stable and inert nature and ease of synthesis.[13] Gold nanoparticles possess size and shape dependant optical and electrical properties and proposed as components in optoelectronic devices.[4-9] Recent studies have shown that Au nanoparticles are promising

materials for biological applications due to their non-toxic nature.[14] A brief overview on the synthesis and properties of Au nanoparticles and nanorods are presented below.

1.2.1. Historic Overview

Colloidal metal nanoparticles have attracted mankind centuries ago due to their fascinating color and medicinal value.[15-17] Metal colloids have been used in East Asian countries, particularly in India, several centuries ago as traditional medicines for the cure of several diseases.[18,19] The fascinating colors of metal nanoparticles have been utilized for decorating glass windows in many cathedrals in Europe (stained glass windows).[20] Another interesting example is the famous Lycurgus cup of 4th century which is now displayed in British Museum.[21] This glass cup is embedded with colloidal metal nanoparticles which appears green when viewed in reflected light. Interestingly, when illuminated from inside, the glass transmits red color. Analysis of the glass reveals that it contains small quantity of an alloy of gold and silver having a diameter of ~70 nm in the molar ratio of (3:7).[21,22] The surface plasmon resonance (*vide infra*) of the alloy is responsible for the special color display in Lycurgus cup (Figure 1.2A).

The first systematic investigation and documentation on the synthesis of colloidal Au nanoparticles were provided by Michael Faraday, one hundred and fifty years ago, in the year 1857.[23] An aqueous solution of sodium tetrachloroaurate, ($Na[AuCl_4]$), was reduced with a solution of

Figure 1.2. (A) Lycurgus cup showing two different colors in reflected light (green) and transmitted light (red) (*adapted from the web site of The British Museum*). (B) Faraday's colloidal suspension of gold with a clearly visible red laser beam and (C) the high resolution transmission electron microscope images of individual colloidal gold particles (*adapted from reference 24*).

phosphorus in carbon disulfide. The reduction proceeds rapidly at room temperature and the bright yellow color of the $Na[AuCl_4]$ solution turned to deep ruby color, characteristic of colloidal gold. Faraday concluded that the gold was dispersed in the liquid in a very finely divided form and its presence could be detected by the reddish opalescence when a narrow intense beam of light is passed through the liquid (Figure 1.2B). The colloidal gold solutions prepared by Faraday are highly stable and still on display at the Museum of the Royal Institute in London (Figure 1.2B). High resolution electron microscopic investigations carried out nearly a century later on Faraday's ruby-colored solution of gold revealed the presence of nanoparticles in the size range of 3-30 nm.[25,26] The fascinating color of metal nanoparticles arises from the surface plasmon resonance and these aspects are discussed below.

1.2.2. Surface Plasmon Resonance

The collective oscillation of the electron in the conduction band under the influence of electromagnetic radiation is known as surface plasmon oscillation.[1-6,26,27] For Ag, Au and Cu nanoparticles, the oscillation frequency is usually in the visible region giving rise to the strong surface plasmon resonance absorption. According to the Drude-Lorentz model, metal is denoted as plasma consisting of an equal number of positive ions (fixed at the crystal lattice) and conduction electrons which are free and mobile. The mean free path of these electrons in gold and silver is ~50 nm: in the case of particles smaller than this dimension, no scattering is expected from the bulk and interactions are mainly with the surface.[27] Thus, when the wavelength of light is much larger than the nanoparticle size, it can set up standing resonance conditions as represented in Figure 1.3. As the wave front of the light passes, the electron density in the particle is polarized to one surface and oscillates in resonance with the light's frequency causing a standing oscillation. Since the standing oscillation is localized at the surface, it is often referred to as the surface plasmon resonance.
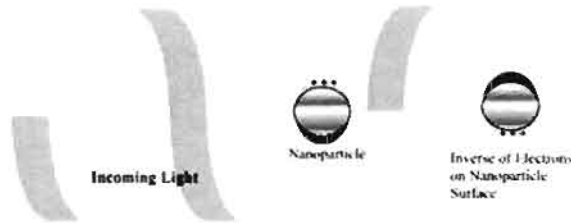
Figure 1.3. Origin of surface plasmon resonance due to coherent interaction of the electrons in the conduction band with light (*adapted from reference 27*).

Surface plasmons can be thus defined as electron coupled electromagnetic waves that propagate along the surface of a conductor. However, only metals with free electrons (essentially Au, Ag and Cu) possess plasmon resonances in the visible spectrum, which give rise to such intense colors.[27] Brilliant colors of noble metal nanoparticles originate from the surface plasmon absorption and several attempts have been made to provide a quantitative description on this.[4-7]

It was one of the great triumphs of classical physics when Gustay Mie[28] presented a solution to Maxwell's equations in 1908 which describes the extinction spectra (sum of scattering and absorption) of spherical particles of arbitrary size. Mie originally calculated the surface plasmon resonance by solving Maxwell's equations for small spheres interacting with an electromagnetic field. Mie's solution is of great interest even today, however, the recent advances in the design of anisotropic metal nanostructures have provided newer challenges. Gans later extended this theory for nanostructured material of ellipsoidal geometries.[29] Recent advances in theoretical methods such as discrete dipole approximation (DDA)[30-32] allow the simulation of surface plasmon resonance absorption of metal nanoparticles having arbitrary geometries.

1.2.3. Tuning the Surface Plasmon Resonance

By varying the size, shape and dielectric of metal nanoparticles, the properties of surface plasmons - in particular their interaction with light - can be tailored, which offers numerous possibilities for the development of photonic devices.[4,26] As the size or shape of the nanoparticle changes, the

surface electron density and hence electric field on the surface varies.[27] This causes dramatic variations in the oscillation frequency of the electrons, generating different optical cross-sections (including absorption and scattering). Bulk gold looks yellowish in reflected light, whereas, thin Au films transmit blue color. This characteristic blue color steadily varies to orange to purple and finally to red, as the particle size is reduced down to ~5 nm. The optical response of spherical gold nanoparticles exhibit a single absorption band at around 520 nm,[33] attributed to the collective dipolar oscillation (surface plasmon resonance). However, the classical electrostatic model predicts that the nanorods of gold and silver split the dipolar resonance into two surface plasmon bands wherein the induced dipole oscillates along the transverse and longitudinal axes.[34,35] Elongated nanoparticles (ellipsoids and nanorods) display two distinct plasmon bands related to transverse and longitudinal electron oscillations.[34] A strong dependence was observed on the longitudinal surface plasmon maximum by varying the aspect ratio, while the position of transverse surface plasmon band remains more or less unaffected.[33-37] Based on these results, it can be concluded that the dimensionality plays a crucial role in determining the optical properties of nanomaterials (Figure 1.4).[36]

The dielectric constant of the surrounding layer also influences the oscillation frequency due to the variation in electron charge density on the nanoparticles.[38] Both solvents and capping agents influence the surface electrons and can thereby affect the surface plasmon resonance.[38,39] The chemically bonded molecules on nanoparticle surface induce electron density variations, which results in a shift in the surface plasmon absorption maximum and these aspects are well documented in recent reviews.[4-9]
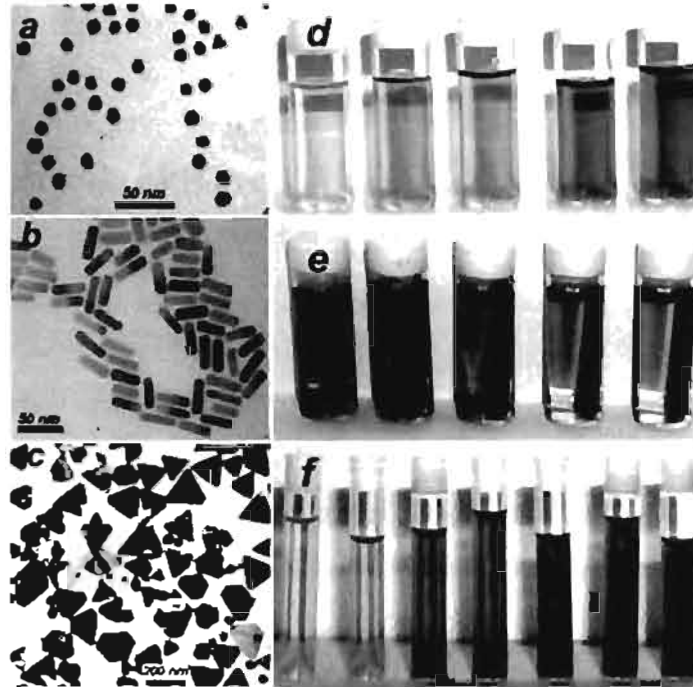
Figure 1.4. *Left:* (a-c) presents transmission electron micrographs of (a) Au nanospheres synthesized using citrate reduction method. (b) Au nanorods synthesized using seed mediated growth. (c) Ag nanoprisms synthesized using DMF reduction. *Right:* (d-f) presents photographs of nanoparticle solution of (d) Au-Ag alloy nanoparticles with increasing Au concentration, (e) Au nanorods with increasing aspect ratio and (f) Ag nanoprisms with increasing lateral size (*adapted from reference 36*).

1.2.4. Synthesis of Au Nanoparticles and Nanorods

Au Nanoparticles: Generally two different strategies, namely top-down and bottom-up approaches, have been adopted for the synthesis of nanomaterials.[8] Top-down approaches such as photolithography and electron beam lithography are practiced by physicists to fabricate Au nanostructures.[40] For the synthesis of Au nanoparticles, chemists usually adopt a bottom-up approach by reducing a metal salt by chemical,[8,9,41-45]

sonochemical,[46] electrochemical[47] and photochemical methods[48] in the presence of capping agents. Capping agents usually stabilize the Au nanoparticles from aggregation and precipitation and also arrest the growth of Au nanoparticles. The size and shape of Au nanomaterials can be further tuned by varying the reduction technique, time and concentration of capping agent.[45]

One of the most popular methods of preparing Au nanospheres is by boiling an aqueous solution of $HAuCl_4$ and sodium citrate.[41] This reduction method was developed by Turkevich[41] in 1951 and the appearance of deep wine color revealed the formation of uniform Au nanoparticles. The average particle diameter can be tuned over a wide range (~10-100 nm) by varying the molar ratio between the gold salt and sodium citrate. However, in the case of particles larger than 30 nm, deviation from a spherical shape as well as a polydispersity was observed.

The two-phase reduction method developed by Schiffrin, Brust and coworkers[42] is another popular method of synthesis of Au nanoparticles. $HAuCl_4$ dissolved in water was extracted to an organic phase by means of phase transfer agent namely, tetraoctylammonium bromide (TOAB). The complexed gold salt is further reduced using an aqueous solution of sodium borohydride, in the presence of thioalkanes or aminoalkanes, which readily bind to the crystalline Au nanoparticles (Figure 1.5) forming a protecting layer. Depending on the ratio of the gold salt and capping agent (thiol/amine), the particle size can be tuned in the range of 1-10 nm. This method have been modified by various groups and currently used for the synthesis of Au and Ag nanoparticles in non-aqueous medium.
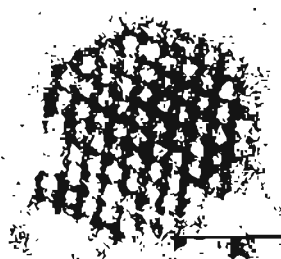
Figure 1.5. A high-resolution transmission electron microscopy image of an individual thiolate-protected gold nanoparticle (*adapted from reference 13*).

Murray and coworkers have reported an interesting and elegant alternative to the two-phase reduction method, which has opened a new field of preparative chemistry.[49] They explored new routes for the design of mixed monolayer-protected clusters by ligand or place exchange reactions. For example, addition of pre-synthesized nanoparticles possessing thiol bearing ligands to a solution of another thiolate molecule having diverse functionality results in the partial substitution of the protecting shell on the nanoparticle surface (Scheme 1.1).
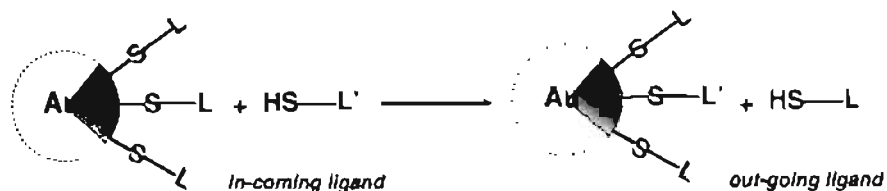
Scheme 1.1. An illustration of the place exchange reaction on the surface of Au nanoparticle.

The mechanism of the exchange reaction of Au nanoparticles with thiols was extensively studied by Murray's group.[49] They showed that the initial phase of the reaction is first order with respect to each reagent (e.g., Au nanoparticles and incoming ligands), consistent with an associative

reaction pathway. This was further supported by a recent observation of the sensitivity of the place-exchange reaction to the electronic effects of the incoming ligand.[50] On the other hand, molecular oxygen and positive electric charge were shown to substantially accelerate the rate of exchange, possibly inducing the formation of an intermediate Au(I) species. This intermediate then undergoes a dissociative pathway, perhaps competing with the main associative mechanism, resulting in the substitution of ligands.

Synthesis of Au Nanorods: Generally, rod-shaped metal nanostructures are synthesized either in rigid templates or in the presence of surfactants. In the former case, the metal ions are reduced inside the cylindrical pores of oxide or polymeric membranes, usually called 'hard template synthesis'.[51] In the latter method, neutral or charged surfactants are used for growing nanorods, usually known as 'soft template synthesis' by adopting electrochemical, photochemical or seed mediated methods.[52-56] Electrochemical synthesis of Au nanorods involves the reduction of $HAuCl_4$ in the presence of 'shape-inducing' cationic surfactants and other additives.[52] These cationic surfactants were found to favor rod formation and act as both the supporting electrolyte and stabilizer. Electrochemical synthesis is carried out in the presence of two cationic surfactants: cetyltrimethylammonium bromide (CTAB) and a hydrophobic surfactant such as tetradecylammonium bromide (TDAB). The ratio between the surfactants controls the average aspect ratio of the Au nanorods.

Murphy and coworkers later reported a seed mediated reduction method for the synthesis of Au and Ag nanorods with excellent aspect ratio control.[53] HAuCl$_4$ was reduced using a mild reducing agent (ascorbic acid) in the presence of Au nanoparticle seeds and CTAB. The addition of different volumes of the seed solution results in the formation of Au nanorods having different aspect ratios. Recently, this method has been improved by El-Sayed and coworkers,[54] resulting in a spectacular increase in nanorod yield. Another approach for the synthesis of Au nanorods is based on a photochemical method[56] which involves the reduction of HAuCl$_4$ in the presence of two surfactants namely CTAB and tetraoctyl ammonium bromide (TOAB) in the presence of a small quantity of AgNO$_3$ and other additives. In this case, authors could control the aspect ratio by varying the concentration of AgNO$_3$ added (Figure 1.6).
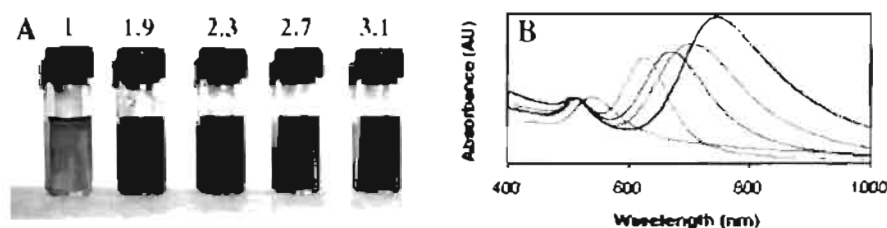
Figure 1.6. (A) Image of photochemically prepared gold nanorods solution (*aspect ratio indicated at the top*) and (B) corresponding UV-vis spectrum (*adapted from reference 56*).

1.2.5. Hybrid Au Nanostructures as Functional Materials

Electroactive Systems: Electrical conduction through molecules in hybrid systems depends critically on the delocalization of molecular orbitals and their connectivity to the metallic contacts.[57] Recently, Dadosh and

coworkers[58] have synthesized dimers of Au nanoparticles using organic molecules bearing dithiol groups and were trapped electrostatically between two microelectrodes (Figure 1.7). The authors have used three types of organic dithiols as linkers: (i) 4,4' -biphenyldithiol (BPD), a fully conjugated molecule, (ii) bis-(4-mercaptophenyl)-ether (BPE), a molecular system with conjugation broken at the centre by an oxygen atom and (iii) 1,4-benzenedimethanethiol (BDMT), which has a break in conjugation near the contacts due to the methylene group. Based on electrical conductivity measurements it was concluded that the linker groups, BPE and BDMT suppresses the conductance relative to BPD due to the breakage of conjugation.
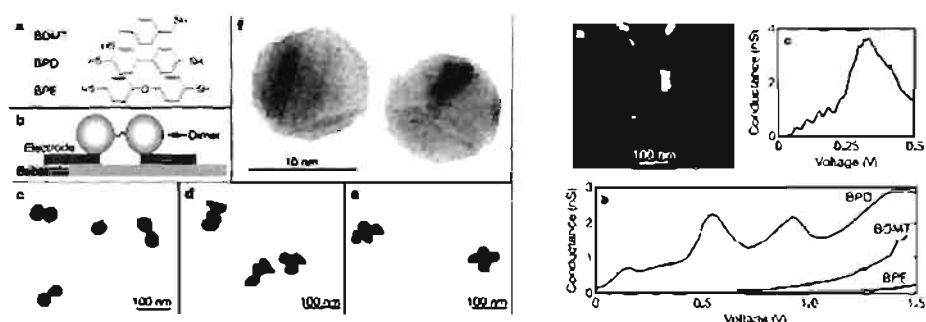
Figure 1.7. *Left:* (a) The structures of the three molecules, (b) the dimer contacting scheme, (c–e) TEM images of BDMT dimer, trimer and tetramer structures made of 50 nm colloidal gold particles, (f) TEM image of a BDMT dimer made of 10 nm colloidal gold particles. The 1 nm separation between the two particles corresponds approximately to the BDMT length (0.9 nm). *Right:* (a) SEM image of a dimer trapped between the two electrodes, (b) the differential conductance as a function of voltage measured for BPD, BDMT and BPE dimers at 4.2 K and (c) coulomb blockade oscillations of the colloidal gold particle which are superimposed on the conduction peak of BPD measured at 4.2 K *(adapted from reference 58).*

Photoactive Systems: Au nanoparticles in the size range of 2-5 nm can behave as conductor, semiconductor or insulator depending on its dimension due to quantum size effects.[59] Optoelectronic properties of hybrid nanomaterials can be tuned by anchoring chromophores on to Au nanoparticles in this size range. Photoinduced electron transfer process from a chromophoric system (pyrene; Chart 1.1A) to Au nanoparticle of ~2 nm was demonstrated by Ipe *et al.*, for the first time.[60] The effect of the transition behavior of metal nanoparticles was more clearly studied by Dulkeith *et al.*[61] by functionalizing lissamine molecules on gold nanoparticles (Chart 1.1B) of different size (1-30 nm) and isolated the resonant energy transfer rate from the decay rates of the excited dye molecules. The increase in lifetime with decrease in the nanoparticle size was indicative of the decreased efficiency of energy transfer.

A wide variety of chromophores have been functionalized on the surface of Au nanoparticles and detailed photophysical investigations were carried out. Ipe and Thomas[62] have demonstrated the role of linker group in modulating the monomer to excimer emission in pyrene functionalized Au nanoparticles and these aspects were investigated by following the steady state and time resolved spectroscopy. Fullerene chromophores containing thiol functionality were synthesized and linked on to the surface of gold nanoparticles by Sudeep *et al.*[63] TEM analysis showed the presence of larger clusters and time resolved studies indicated an efficient energy transfer from the photoexcited fullerene to Au nanoparticles.

A cartoonic representation of the various photophysical processes in chromophore functionalized Au nanoparticles is presented in Scheme 1.2.
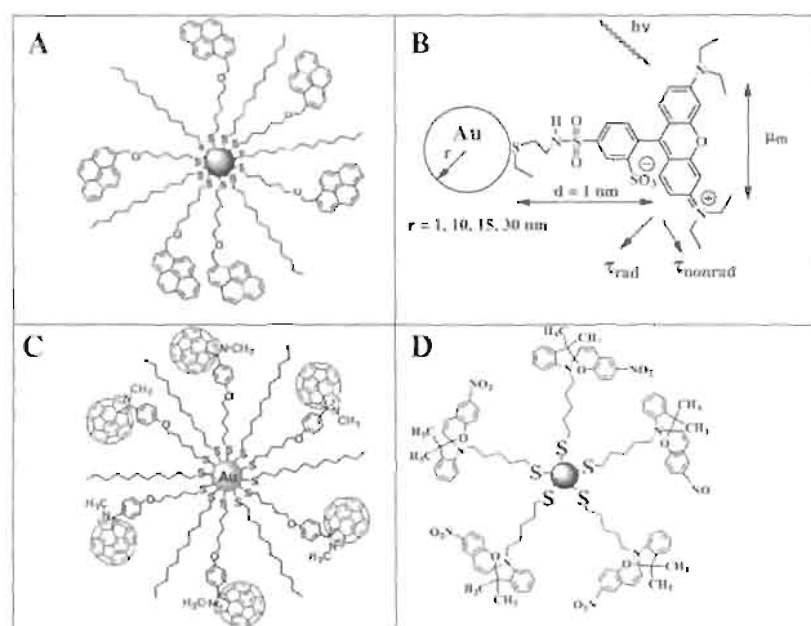
Chart 1.1. Au nanoparticles functionalized with various photoresponsive molecules (adapted from references 60-64).
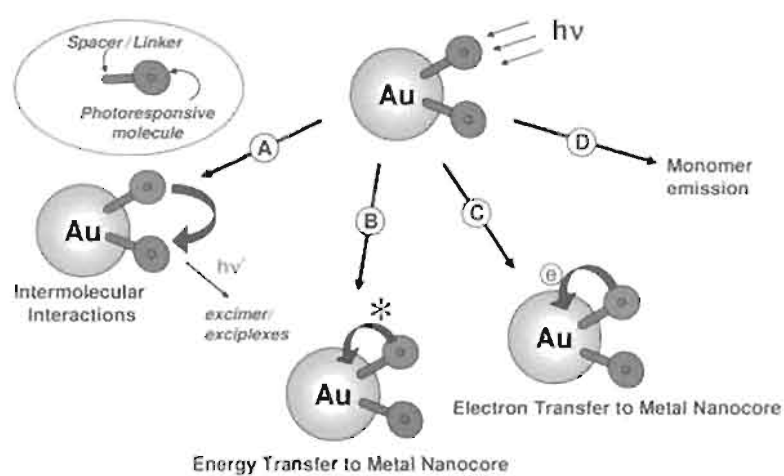
Scheme 1.2. Various deactivation channels in a chromophore functionalized Au nanoparticle (adapted from reference 9).

Ipe *et al.*[64] have reported the design of a photoswitchable double shell structure by anchoring spiropyrans on Au nanoparticles (Chart 1.1D). The light regulated changes in the topographic properties of spiropyran capped Au nanoparticles (i.e., interconversion between the zwitterionic and neutral forms) were exploited for the assembly and release of various amino acids. These observations offer intriguing possibilities for designing drug delivery systems with controlled release abilities.

Catalytic Systems: Bulk gold is viewed as an inert metal, however it was found that Au nanoparticles < 5 nm in diameter are catalytically active for several reactions.[65] Also, catalysts based on Au nanoparticles allow significantly lower reaction temperature than existing processes which offer newer possibilities in the development of energy efficient systems.[66] For example, the oxidation of CO (an automobile exhaust) is one of the reactions wherein Au nanoparticles are reported as efficient catalysts at room temperature (Figure 1.8).[65,66] Compilation of the experimental data of the CO oxidation activity as a function of size of Au nanoparticle catalyst
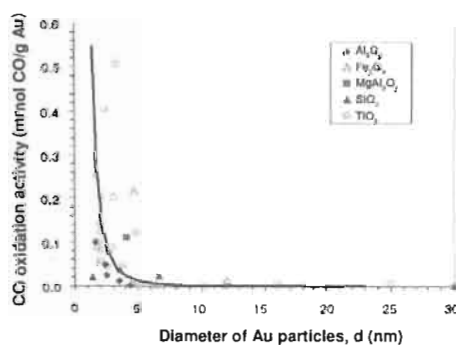
Figure 1.8. Catalytic activities for CO oxidation at 273 K as a function of Au nanoparticle size for different support materials (*adapted from reference 65*).

on various supports is presented in Figure 1.8. These studies clearly indicate that the catalytic activity of Au nanoparticles increases dramatically with decrease in particle size and are active only below 5 nm.

Biomedical Applications: Recent studies have shown that Au nanoparticles are nontoxic to human.[14] Another interesting property of Au nanoparticles/nanorods is the high optical cross-section of the surface plasmon absorption which is typically 4-5 orders of magnitude higher than conventional dyes.[67-69] These unique features of Au nanoparticles/nanorods provide excellent opportunities for their use in biomedical field for diagnosis,[70] imaging[71] and photothermal treatment[72,73] of cancer cells. The absorption cross-section of the surface plasmon band of an Au nanoparticle (product of the efficiency of absorption and the cross-sectional area of the nanoparticle) having a diameter of 40 nm is calculated as 2.93×10^{-15} m^2 at 528 nm which corresponds to a molar extinction coefficient of 7.66×10^9 M^{-1} cm^{-1}.[32] Au nanoparticles are poor emitters of light and the absorbed light is efficiently converted into localized heat and this strategy has been successfully used for the laser photothermal destruction of cancer cells.[72,73] Au nanoparticles/nanorods can be targeted to tumor site by conjugating them with bioactive molecules.[74]

The optical resonance of Au nanoparticles is strongly desired to be in the near infrared (NIR) region of the biological water window, wherein the optical penetration of tissue is the highest.[75] Surface plasmon absorption of Au nanorods can be conveniently tuned to this region by

varying the aspect ratio. For sensing and other diagnostic application,[70,72,73] it is desirable to have nanomaterials with a high absorption cross-section whereas, particles having strong optical scattering are useful for imaging applications.[71] The contributions of absorption/scattering to the total extinction for nanoparticles of varying dimension have been studied in detail.[76] For nanospheres and nanorods, increase in the diameter resulted in an increase in the extinction cross-section as well as in the relative contribution of scattering. However, an increase in the nanorod aspect ratio, at a constant radius, does not effect the extinction cross-section or the ratio of scattering to absorption. A representative example for imaging and photothermal damage using Au nanoparticles and nanorods are shown in Figures 1.9 and 1.10. respectively.
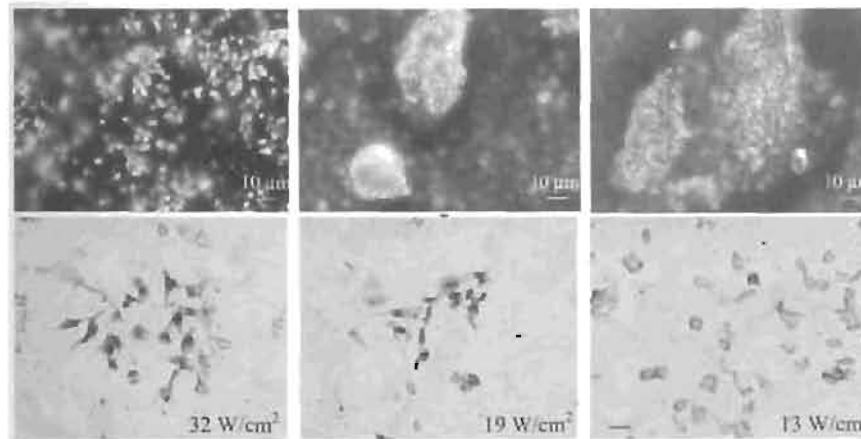
Figure 1.9. *Top:* Light scattering images of anti-EGFR/Au nanospheres after incubation with cells for 30 min at room temperature. *Bottom:* HOC malignant cells irradiated at different laser powers and then stained with trypan blue. HOC malignant cells were killed at and above 19 W/cm^2. Scale bar: 60 mm for all images (*adapted from reference 72*).
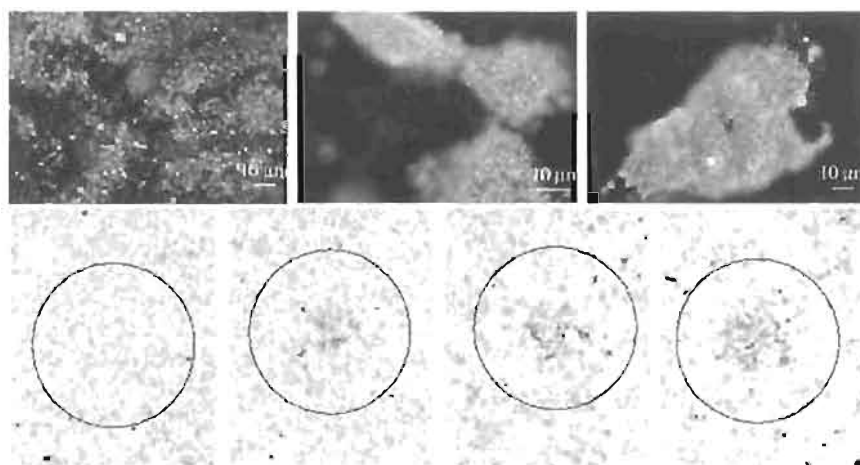
Figure 1.10. *Top:* Light scattering images of anti-EGFR/Au nanorods after incubation with cells for 30 min at room temperature. *Bottom:* Selective photothermal therapy of cancer cells with anti-EGFR/Au nanorods incubated. The circles show the laser spots on the samples (*adapted from reference 73*).

1.3. Carbon Nanotubes

Carbon nanotubes (CNTs) are allotropes of carbon that are molecular scale tubes of graphene sheets having outstanding electronic and mechanical properties. An ideal nanotube is a hexagonal network of carbon atoms rolled as a seamless cylinder, with diameter of the order of few nanometers (0.8-2.0 nm) and a tube length varying thousands of nanometer. The chemical bonding of nanotubes are similar to those of graphite, composed entirely of sp^2 hybridized carbon atoms. Carbon nanotubes are mainly classified as two types: single walled carbon nanotubes (SWNTs) and multiwalled carbon nanotubes (MWNTs). This class of quasi one-dimensional nanostructures possesses unique electrical

properties which make them an attractive candidate for the fabrication of nanodevices[77-87] and these aspects are discussed below.

1.3.1. Electronic Properties of Carbon Nanotubes

Based on the theoretical studies it was proposed that the electronic properties of "ideal" carbon nanotubes depend on their diameter and chirality.[88-91] However, the carbon nanotubes are probably not as perfect as they were envisaged theoretically. Various defects such as pentagons. heptagons, vacancies or dopant are found to drastically modify the electronic properties of CNTs.[88] The nanotubes are usually described using the chiral vector (AA' in Figure 1.11), $C_h = n \times a_1 + m \times a_2$, which connects two crystallographically equivalent sites (A and A') on a graphene sheet (where a_1 and a_2 are unit vectors of the hexagonal honeycomb lattice and n and m are integers) (Figure 1.11).[88] The chiral vector C_h also defines a chiral angle θ, which is the angle between C_h and the zigzag direction of the graphene sheet (Figure 1.11).
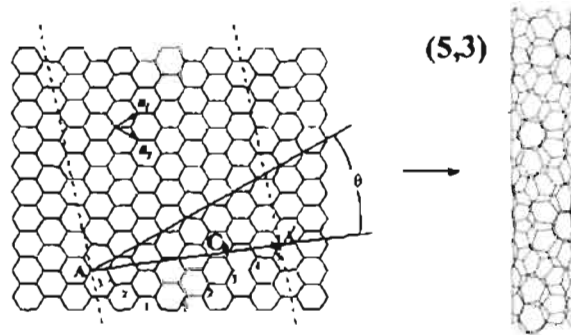
Figure 1.11. Schematic diagram showing the possible wrapping of the two-dimensional graphene sheet into tubular forms. (An example illustrating the rolling of a (5,3) nanotube is presented; *adapted from reference 88*).

Nanotube topology is usually characterized by two integer numbers (n,m) defining a particular symmetry such as *chiral* (n,m), *armchair* (n,n) and *zigzag* $(n,0)$ (Figure 1.12A).[88] The electronic properties of a nanotube vary in a periodic way between metallic and semiconductor and follows a general rule: if $(n - m)$ is a multiple of 3, then the tube exhibits a metallic behavior and possess a finite value of carriers in the density of states at the Fermi energy level (Figure 1.12B).[88] In contrast, if $(n - m)$ is *not* a multiple of 3, then the tube exhibits a semiconducting behavior and have no charge carriers in the density of states at the Fermi energy level (Figure 1.12C).[94] The sharp peaks (van Hove singularities) in the density of states (DOS) are characteristic signature of the one-dimensional (1D) conductors.[94] The DOS of various types of CNTs were experimentally investigated and compared using theoretical models.[88]
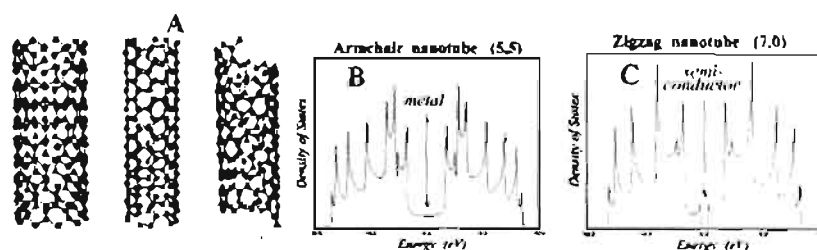
Figure 1.12. (A) Models of three atomically perfect SWNT structures, (B) electronic properties of an armchair (5,5) nanotube exhibiting a metallic behavior (finite value of charge carriers in the DOS at the Fermi energy, located at zero), (C) the zigzag (7,0) nanotube is a small gap semiconductor (no charge carriers in the DOS at the Fermi energy). Sharp spikes in the DOS denote van Hove singularities (*adapted from reference 88*).

Electronic transitions between the energy bands of SWNTs can be observed by standard spectroscopic techniques.[92] Besides the

heterogeneity of the samples, (with respect to the tube diameters and helicities) impurity doping also contribute to the breadth of the absorption features [92] Since the band gaps are inversely proportional to the tube diameters, structural information can be derived from the band transition energies. Research activities were pursued, in recent years, focusing on the separation of CNTs by their diameter, bandgap, and metallic/semiconducting character, in a scalable quantity with higher precision (Figure 1.13).[92]
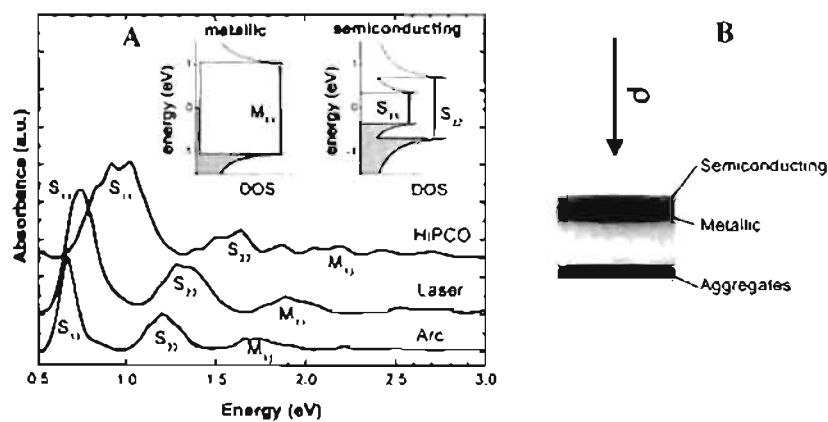
Figure 1.13. (A) Electronic transitions between the energy bands of SWNTs, observed by transmission spectroscopy of films and labeling of interband transitions and (B) separation of semiconducting and metallic SWNTs using mixtures of competing co-surfactants after ultracentrifugation *(adapted from reference 92)*.

1.3.2. Synthesis of Carbon Nanotubes

Although there have been many interesting and successful attempts to grow CNTs by various methods, we restrict our discussion to the three most widely used techniques: (i) arc discharge, (ii) laser furnace and (iii) chemical vapor deposition (CVD).

Arc Discharge Method: Carbon nanotubes were first produced by an arc discharge method. In 1990, Krätschmer[93] developed a method for the mass production of fullerenes by evaporating graphite rods, in contact, by applying an a.c voltage in an inert atmosphere. Later d.c arc voltage[94] was applied between two separated graphite rods (a modified version of the SiC powder production apparatus) and the evaporated anode generates fullerenes in the form of soot in the chamber.[95] Interestingly, a part of the evaporated anode got deposited on the cathode from which Ijima found the treasure, carbon nanotubes.[96] A brief description of CNT synthesis by the arc discharge method (Figure 1.14) is presented below.[97]
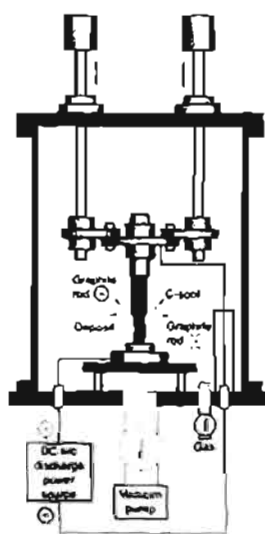
Figure 1.14. Schematic diagram of CNT formation apparatus by the arc-discharge method (*adapted from reference 97*).

An appropriate gas of the desired pressure was introduced to the chamber after the evacuation and a d.c arc voltage was applied between the graphite rods. Anode evaporates to form fullerenes which were

deposited in the form of soot in the chamber and a small portion of coaxial graphene sheets was deposited on the cathode. These graphene sheets were characterized as multi-walled carbon nanotubes (MWNTs) and their large-scale synthesis has been achieved in helium gas. It was later found that methane is best suitable for the synthesis of MWNTs with high crystallinity.[98,99] When a graphite rod containing metal catalyst (Fe, Co. etc.) was used as anode along with a pure graphite cathode, single walled carbon nanotubes (SWNTs) were generated in the form of soot.[100]

Laser Furnace method: The laser vaporization method. originally developed for the production of clusters[101] and ultrafine particles.[102] have been used by Smalley's group[103,104] for the synthesis of fullerenes and CNTs. Carbon melts at very high temperature and hence lasers are more suitable due to the high energy density compared to other vaporization techniques. Fullerenes were first discovered by this method and identified by mass spectroscopy; however. yields were too low for isolation. To produce large quantities of fullerenes and other carbon based nanomaterials, Smalley's group developed the laser furnace method together with an annealing system in 1992. Fullerenes were produced only at high furnace temperature, underlining the importance of annealing. Later in 1996, these discoveries were applied to produce SWNTs.[104] Figure 1.15 shows the setup of the apparatus consisting of (i) the laser furnace, (ii) a target carbon composite doped with catalytic metals and (iii) a water-cooled trap and flow systems for the buffer gas (to maintain constant pressures and flow rates). A laser beam (typically a YAG or CO_2 laser) is

introduced through the window and focused on to the target located in the center of the furnace. The target is vaporized at high-temperature in the presence of argon buffer gas to form SWNTs. The argon flow rate and pressure are typically 1 cm.s⁻¹ and 500 torr, respectively. The SWNTs produced are conveyed by the buffer gas to the trap, where the CNTs are collected. The vaporization surface is kept fresh by changing the focus point or moving the target. The method has many advantages such as high-quality SWNT production and diameter control.
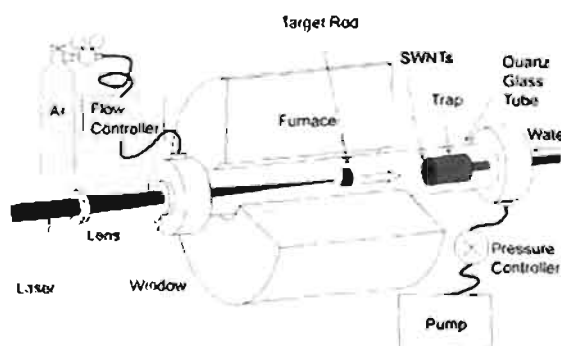
Figure 1.15. Schematic diagram of the laser-furnace apparatus (*adapted from reference 99*).

Chemical Vapor Deposition (CVD): Compared to arc-discharge and laser furnace methods, CVD is a simple and more economic technique for the synthesis of CNTs. Versatility of the technique includes (i) the use of precursor of any state (solid, liquid or gas) and (ii) the growth of CNTs in a variety of forms (powder, films of different thickness or even a desired architecture of nanotube).[99] The three main parameters that govern the CNT growth in CVD are the nature of the hydrocarbon, catalyst and growth

temperature. The process involves the thermal decomposition of hydrocarbon vapor by passing through a tube furnace (15-60 min) in which catalyst material is present at sufficiently higher temperature (600-1200°C). CNTs grow over the catalyst and are collected upon cooling the system to room temperature. In the case of liquid hydrocarbon inert gas is purged through heated liquid and the vapor is carried to the reaction furnace. Vaporization of a solid hydrocarbon (camphor, naphthalene etc.) can be conveniently achieved in another furnace kept at low temperature before the main high temperature reaction furnace (Figure 1.16a). Transition metals (Fe, Co, Ni) are the commonly used catalyst for CNT growth. The phase diagram of carbon and the above mentioned metals suggests finite solubility of carbon in these transition metals at higher temperatures. Catalytically decomposed carbon species of the hydrocarbon dissolves in metal nanoparticles and precipitates out, on supersaturation, in the form of a fullerene dome extending into a carbon cylinder (like an inverted test tube). System does not have any dangling bonds and hence the energy is minimum.[105] Two types of growth models are proposed depending on the substrate-catalyst interaction (Figure 1.16b).[99] When the interaction is strong, CNT grows up with catalyst particles rooted at its base, known as 'base growth model'. When the substrate-catalyst interaction is weak, the catalyst particles is lifted up by the growing CNT and promotes the growth of carbon nanotubes at its tip known as 'tip growth model'. The formation of SWNTs or MWNTs is governed by the size of the catalyst particles: when the particle size is of a few nanometers, SWNTs are formed whereas, particles of few tens of nanometers yielded MWNTs.[99]

(a)

(b)
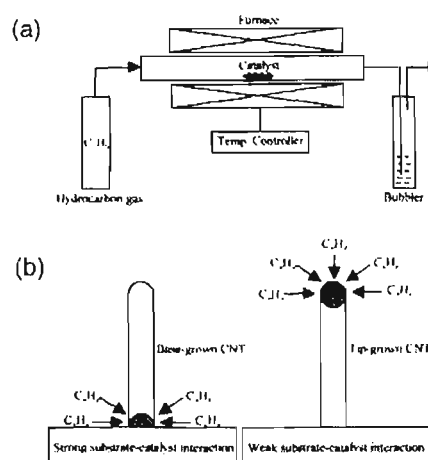
Figure 1.16. (a) Schematic diagram of a CVD setup. (b) Probable models for CNT growth (*adapted from reference 99*).

It is found that low temperature CVD (600-900°C) yielded MWNTs, whereas higher temperature reactions (900-1200°C) favor SWNT growth. Thus, SWNTs have a higher energy of formation owing to their smaller diameters which result in high curvature and high strain energy.[99] MWNTs can be easily grown from most hydrocarbons whereas SWNTs can be only grown from selected hydrocarbon such as carbon monoxide and methane, which possess reasonable stability in the temperature range of 900-1200°C. Smalley's laboratory adopts a different technique for the mass production of SWNTs by the high pressure carbon monoxide (HiPCO) technique. In this method, a Fe pentacarbonyl catalyst liberates Fe particles *insitu* at high temperatures. The high pressure of CO (~30 atm) enhances the disproportionation of CO molecules into carbon atoms and accelerates SWNT growth.[106]

1.3.3. Hybrid Carbon Nanotubes

Hybrid nanomaterials based on CNTs were synthesized through covalent functionalization[107] and supramolecular assembly.[108] These hybrid systems have been proposed as potential materials for biomedical and photovoltaic applications. Covalent functionalization of molecular appendages on CNTs can be achieved through a cycloaddition reaction, radical reaction or carboxylic acid functionalization.[107] Supramolecular organization is another important strategy used for designing hybrid CNTs which adopts various noncovalent interactions such as π-π stacking and hydrophobic interactions.[108] These aspects were extensively documented as reviews.[107,108] Recently, researchers were successful in the encapsulation of molecules inside the CNTs[109] which result in the formation of hybrid materials with unique properties and details are provided below.

Molecules within CNTs: The encapsulation of molecules inside nanotube cavity through physical adsorption results in a drastic change in nanotube properties such as conductance and electronic band gap.[109] The first molecule ever reported inside carbon nanotubes is C_{60} which occurred accidentally during the synthesis of CNTs.[110] These materials were unambiguously characterized by HRTEM. Nanotubes filled with fullerenes were named "peapods" due to their similarity in appearance (Figure 1.17). The interaction of C_{60} in CNT cavity is highly efficient (3 eV per C_{60}) due to strong van der Waals forces and perfect geometrical match in the shape of fullerene and interior of CNTs.[110] The encapsulation of C_{60} in SWNTs was
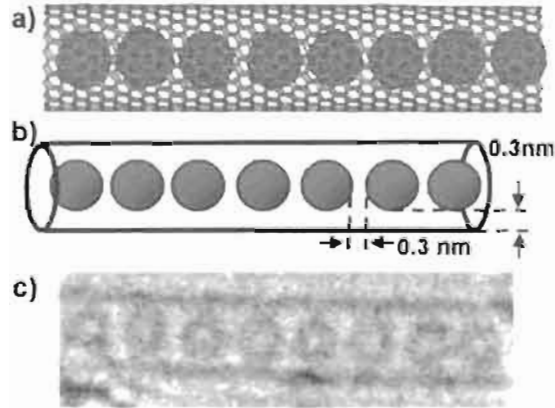
Figure 1.17. (a) Structural diagram, (b) schematic representation and (c) HRTEM micrograph of C_{60}@SWNT (*adapted from reference 110*).

found to be spontaneous and irreversible. In addition, fullerenes provide good contrast and the hybrid systems are stable under the electron beam of a TEM, which facilitates their easier imaging and analysis.

1.3.4. Applications of Carbon Nanotubes

Recent studies have shown that CNTs have potential applications as chemical sensors,[111] nanoscale logic gates[82] and field-effect transistors.[83-85] A brief overview on some of the recent developments on the use of CNTs is given below.

CNTs as Electron Source: Field emission (FE) is the emission of electrons from a solid under intense electric field and the high aspect ratio of CNTs make them ideal for such applications.[112] The simplest way to create such a field is by field enhancement at the tip of a sharp object . Si or W tips, made by anisotropic etching or deposition, were initially used for such applications. CNTs have an advantage over Si or W tips due to their

strong covalent bonding which makes them physically inert to sputtering, chemically inert to poisoning and can carry a huge current density of 10^9 A/cm^2 before electron migration. In addition, when driven to high currents, their resistivity decreases, so that they do not tend to electric field-induced sharpening. CNTs have better FE performance than other forms of carbon based materials (for e.g., diamond). A potential application of FE from CNTs is as electron guns for next generation scanning electron microscopes (SEM) and transmission electron microscopes (TEM) (Figure 1.18).[112] A single MWNT field emission source is found be 30 times brighter than existing electron sources and with a small energy width of 0.25 eV. MWNTs are preferred over SWNTs because of their greater mechanical stiffness.
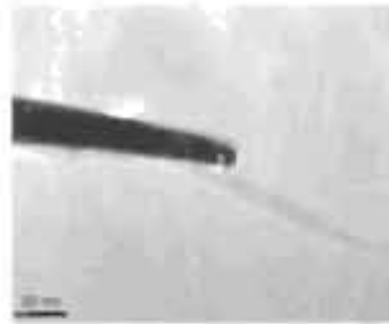
Figure 1.18. A MWNT attached to metal tip for use as an FE electron source for the electron gun on a SEM (*adapted from reference 112*).

Flexible Batteries: CNT based battery architecture was first designed by Grüner and coworkers[113] at the University of California. The prototype designed by them showed an open-circuit voltage of ~1.45 V, with a total capacity between 15-25 mA h. The proof-of-concept device consists of Zn

foil anode which acts as a charge collector, followed by a separator soaked in a solution of NH_4Cl and $ZnCl_2$ electrolytes. The cathode is then added, made from a paste of MnO_2, CNTs, and the same electrolyte mixture.

More recently, Ajayan and coworkers[114] from Rensselaer Polytechnic Institute, USA have prepared paper batteries that can be rolled or folded just like paper without any loss of efficiency (Figure 1.19). The paper version of charge storage device consists of electrodes, electrolyte and a separator. Vertically aligned multiwalled carbon nanotubes (electrode) were deposited on a Si substrate using vapor deposition method. Plant cellulose was casted on top of the layer and dried to form the separator. This paper layer is then impregnated with an ionic liquid – an organic salt that is liquid at room temperature – which acts as the electrolyte. Since the ionic liquid does not contain water, batteries will not freeze or evaporate, which enables them to withstand extreme temperatures from 195 K to 450 K.
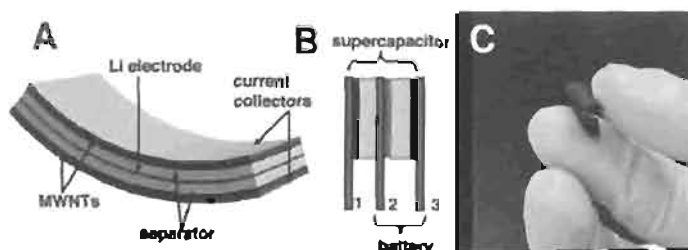
Figure 1.19. Supercapacitor-battery hybrid energy devices based on nanocomposite units. (A) Schematic representation of a three-terminal hybrid energy device that can act as both supercapacitor and battery, (B) the three terminals are defined, and the battery and supercapacitor segments of the device are shown and (C) image of flexible paper battery (*adapted from reference 114*).

CNTs Based Photovoltaics: CNTs possess unique electrical and electronic properties, wide electrochemical stability window and large

surface area which make them an ideal candidate for energy conversion devices.[77-87] Semiconducting carbon nanotubes undergo charge separation when subjected to band gap excitation and considered to be useful for the fabrication of solar cells (left panel in Figure 1.21).[115] SWNT based donor-acceptor and hybrid systems have also been proposed as potential molecular components for solar energy conversion (right panel in Figure 1.20).[107a,115,116] Fast forward electron transfer and slow charge recombination is one of the significant feature of CNT based molecular systems.[116]
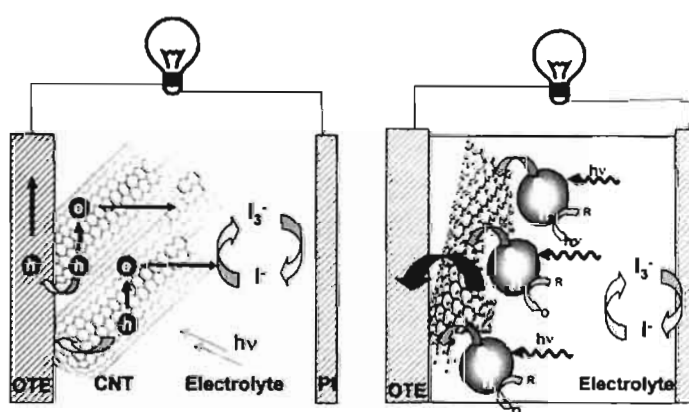
Figure 1.20. Strategies to employ carbon nanotubes in photochemical solar cells: (left) by direct excitation of carbon nanotubes; (right) by excitation of light-harvesting assemblies anchored on carbon nanotubes (*adapted from reference 115*).

Biological Applications: Tissues are highly transparent to the optical excitation in the spectral region of 700-1100 nm.[75] The strong optical absorbance of SWNT in this region combined with their biocompatibility, ability to interact with plasma membrane and cross cytoplasm make them an ideal candidate for biomedical applications.[117] An extensive review on

the use of CNTs and their functionalized derivatives as biomaterial, particularly its use in drug delivery and cancer therapy is presented in a recent review by Prato, Bianco and coworkers.[107c]

1.4. Objectives of the Present Work

As mentioned in the previous sections, significant progress has been made in the synthesis of monodisperse nanomaterials whose optoelectronic properties can be fine tuned by varying the size and shape. One of the current focuses of research in this area is on the design of hybrid nanomaterials by integrating nanoscale components. The overall objective of this thesis is to design functionalized Au nanoparticles and link them to Au nanorods and carbon nanotubes. The newly designed hybrid nanomaterials possess unusual optical properties and these aspects are discussed in Chapters 2-4.

1.5. References

(1)   Kreibig, U.; Vollmer, M. in *Optical Properties of Metal Clusters*, Springer-Verlag, New York, 1995.

(2)   Thomas, K. G. in *Nanomaterials Chemistry*, (Eds: Rao, C. N. R.; Müller, A.; Cheetham, A. K.), Wiley-VCH, Weinheim, Germany, 2007, p 185.

(3)   Katz, E.; Shipway, A. N.; Willner, I. in *Nanoscale Materials;* (Eds: Liz-Marzán, L. M.; Kamat, P. V.), Kluwer Academic Publishers, Boston, 2003, p 5.

(4)   El-Sayed, M. A. *Acc. Chem. Res.* **2001**, *34*, 257.

(5)   Daniel, M.-C.; Astruc, D. *Chem. Rev.* **2004**, *104*, 293.

(6)   Kelly, K. L.; Coronado, E.; Zhao, L. L.; Schatz, G. C. *J. Phys. Chem. B* **2003**, *107*, 668.

(7)   Burda, C.; Chen, X.; Narayanan, R.; El-Sayed, M. A. *Chem. Rev.* **2005**, *105*, 1025.

(8)   Shenhar, R.; Rotello, V. M. *Acc. Chem. Res.* **2003**, *36*, 549.

(9)   Thomas, K. G.; Kamat, P. V. *Acc. Chem. Res.* **2003**, *36*, 888.

(10)   Feynman, R. P. *Eng. Sci.* **1960**, *23*, 22.

(11)   Park, J.; Lee, E.; Hwang, N.-M.; Kang, M.; Kim, S. C.; Hwang, Y.; Park, J.-G.; Noh, H.-J.; Kim, J.-Y.; Park, J.-H.; Hyeon T. *Angew. Chem. Int. Ed.* **2005**, *44*, 2872.

(12)   (a) Wang, Z. L.; Mohamed, M. B.; Link, S.; El-Sayed, M. A. *Surf. Sci.* **1999**, *440*, L809; (b) Wang, Z. L.; Gao, R. P.; Nikoobakht, B.; El-Sayed, M. A. *J. Phys. Chem. B* **2000**, *104*, 5417; (c) Johnson, C. J.; Dujardin, E.; Davis, S. A.; Murphy, C. J.; Mann, S. *J. Mater. Chem.* **2002**, *12*, 1765.

(13)   Edwards, P. P.; Thomas, J. M. *Angew. Chem. Int. Ed.* **2007**, *46*, 5480.

(14)   (a) Rosi, N. L.; Mirkin, C. A.; *Chem. Rev.* **2005**, *105*, 1547; (b) Salata, O. V. *J. Nanobiotechnol.* **2003**, *2*, 3; (c) Whitesides, G. M. *Nat. Biotechnol.* **2003**, *21*, 1161.

(15)   Kerker, M. *J. Colloid Interface Sci.* **1985**, *105*, 297.

(16)   Rao, C. N. R.; Kulkarni, G. U.; Thomas, P. J.; Edwards, P. P. *Chem. Soc. Rev.* **2000**, *29*, 27.

(17)   Link, S.; El-Sayed, M. A. *Int. Rev. Phys. Chem.* **2000**, *19*, 409.

(18)   Mishra, L. C. *Scientific Basis for Ayurvedic Therapies*, CRC Press, 2004, p 560.

(19)   Brown, C. L.; Bushell, G.; Whitehouse, M. W.; Agrawal, D. S.; Tupe, S. G.; Paknikar, K. M.; Tiekink, E. R. T. *Gold Bull.* **2007**, *40*, 245.

(20)   Hunt, L. B. *Gold Bull.* **1976**, *4*, 134.

(21)   Barber, D. J.; Freestone, I. C. *Archaeometry* **1990**, *32*, 33.

(22)   Wagner, F. E.; Haslbeck, S.; Stievano, L.; Calogero, S.; Pankhurst, Q. A.; Martinek, K. P. *Nature* **2000**, *407*, 691.

(23)   Faraday, M. *Philos. Trans. Royal Soc. London* **1857**, *147*, 145.

(24)   Thomas, J. M. *Nova Acta Leopoldina* **2003**, *88*, 109.

(25)   Thomas, J. M. *Pure Appl. Chem.* **1988**, *60*, 1517.

(26)   Barnes, W. L.; Dereux, A.; Ebbesen, T. W. *Nature* **2003**, *424*, 824.

(27)   Eustis, S.; El-Sayed, M. A. *Chem. Soc. Rev.* **2006**, *35*, 209.

(28)   Mie, G. *Ann. Phys.* **1908**, *25*, 377.

(29)   Gans, R. *Ann. Phys.* **1912**, *37*, 881.

(30)   Hao, E.; Schatz G.; Hupp, J. *J. Fluoresc.* **2004**, *14*, 331.

(31)   Kelly, K. L.; Coronado, E.; Zhao L. L.; Schatz, G. C. *J. Phys. Chem. B* **2003**, *107*, 668.

(32)   Jain, P. K.; Lee, K. S.; El-Sayed, I. H.; El-Sayed, M. A. *J. Phys. Chem. B* **2006**, *110*, 7238.

(33)   Link, S.; El-Sayed, M. A. *J. Phys. Chem. B* **1999**, *103*, 4212.

(34)   Sosa, I.; Noguez, C.; Barrera, R. *J. Phys. Chem. B* **2003**, *107*, 6269.

(35)   Link, S.; El-Sayed, M. A.; Mohamed, M. B. *J. Phys. Chem. B* **2005**, *109*, 10531.

(36)   Liz-Marzán, L. M. *Mater. Today* **2004**, *7*, 26.

(37)   Pérez-Juste, J.; Rodriguez-Gonzalez, B.; Mulvaney, P.; Liz-Marzán, L. M. *Adv. Funct. Mater.* **2005**, *15*, 1065.

(38)   Mulvaney, P. *Langmuir* **1996**, *12*, 788.

(39)   Thomas, K. G.; Zajicek, J.; Kamat, P. V. *Langmuir* **2002**, *18*, 3722.

(40)   Yu, T.; Ober, C. K.; Kuebler, S. M.; Zhou, W.; Marder, S. R.; Perry, J. W. *Adv. Mater.* **2003**, *15*, 517.

(41)   Turkevich, J.; Stevenson, P. C.; Hiller, J. *Discuss. Faraday Soc.* **1951**, *11*, 55.

(42)   Brust, M.; Walker, M.; Bethell, D.; Schiffrin, D. J.; Whyman, R. *J. Chem. Soc., Chem. Commun.* **1994**, 801.

(43)   Teranishi, T.; Hosoe, M.; Tanaka, T.; Miyake, M. *J. Phys. Chem.* **1999**, *103*, 3818.

(44)   (a) Schmid, G.; *Clusters and Colloids*, VCH, Weinheim,1994; (b) Schmid, G. *Chem. Rev.* **1992**, *92*, 1709.

(45) Templeton, A. C.; Wuelfing, W. P.; Murray. R. W. *Acc. Chem. Res.* **2000**. *33*, 27.

(46) Pileni, M. P. *Langmuir* **1997**, *13*, 3266.

(47) Furstner, A. *Active Metals,* VCH, Weinheim, 1996.

(48) (a) Esumi, K.; Suzuki, A.; Aihara, N.; Usui, K.; Torigoe, K. *Langmuir* **1998**, *14*, 3157; (b) Troupis, A.; Hiskia, A.; Papaconstantinou. E. *Angew. Chem. Int. Ed.* **2002**, *41*, 1911; (c) Mandal, S.; Selvakannan, P. R.; Pasricha. R.; Sastry, M. *J. Am. Chem. Soc.* **2003**, *123*, 1470; (d) Sanyal. A.; Sastry. M. *Chem. Commun.* **2003**, 1236.

(49) Song, Y.; Murray, R. W. *J. Am. Chem. Soc.* **2002**, *124*, 7096.

(50) Ionita, P.; Gilbert, B. C.; Chechik. V. *Angew. Chem. Int. Ed.* **2005**. *44*. 3720.

(51) (a) Brumlik, C. J.; Martin, C. R. *J. Am. Chem. Soc.* **1991**, *113*. 3174; (b) Martin, C. R. *Chem. Mater.* **1996**, *8*, 1739.

(52) Yu, Y.; Chang, S.; Lee, C.; Wang C. R. C. *J. Phys. Chem. B* **1997**, *101*, 6661.

(53) (a) Jana, N. R.; Gearheart, L.; Murphy, C. J. *J. Phys. Chem. B* **2001**. *105*, 4065; (b) Busbee, B. D.; Obare, S.O.; Murphy, C. J. *Adv. Mater.* **2003**, *15*. 414.

(54) Link, S.; Mohamed, M. B.; El-Sayed, M. A. *J. Phys. Chem. B* **1999**, *103*. 3073.

(55) (a) Murphy, C. J.; Sau, T. K.; Gole, A. M.; Orendorff, C. J.; Gao, J.; Gou. L.; Hunyadi, S. E.; Li, T. *J. Phys. Chem. B* **2005**, *109*, 13857. b) Gole. A. M.; Murphy, C. J. *Chem. Mater.* **2004**, *16*, 3633.

(56) Kim, F.; Song, J. H.; Yang, P. *J. Am. Chem. Soc.* **2002**, *124*, 14316.

(57) (a) Nitzan, A.; Ratner, M. A. *Science* **2003**, *300*, 1384; (b) Joachim, C.; Gimzewski, J. K.; Aviram, A. *Nature* **2000**, *408*, 541.

(58) Dadosh, T.; Gordin, Y.; Krahne, R.; Khivrich, I.; Mahalu, D.; Frydman. V.; Sperling, J.; Yacoby, A.; Bar-Joseph, I. *Nature* **2005**, *436*, 677.

(59) Kamat, P. V. *J. Phys. Chem. B* **2002**, *106*, 7729.

(60)   Ipe, B. I.; Thomas, K. G.; Barazzouk, S.; Hotchandani, S.; Kamat, P. V. _J._
         Phys. Chem. B. **2002,** _106,_ 18.

(61)   Dulkeith, E.; Morteani, A. C.; Niedereichholz, T.; Klar, T. A.; Feldmann, J.;
         Levi, S. A.; van Veggel, F. C. J. M.; Reinhoudt, D. N.; Moller, M.; Gittins,
         D. I. _Phys. Rev. Let._ **2002,** _89,_ 203002.

(62)   Ipe, B. I.; Thomas, K. G. _J. Phys. Chem. B_ **2004,** _108,_ 13265.

(63)   Sudeep, P. K.; Ipe, B. I.; Thomas, K. G.; George, M. V.; Barazzouk, S.;
         Hotchandani, S.; Kamat, P. V. _Nano. Lett._ **2002,** _2,_ 29.

(64)   Ipe, B. I.; Mahima, S.; Thomas, K. G. _J. Am. Chem. Soc._ **2003,** _125,_
         7174.

(65)   Janssens, T. V. W.; Clausen, B. S.; Hvolbæk, B.; Falsig, H.; Christensen,
         C. H.; Bligaard, T.; Nørskov, J. K. _Top. Catal._ **2007,** _44,_ 15.

(66)   Lopez, N.; Janssens, T. V. W.; Clausen, B. S.; Xu, Y.; Mavrikakis, M.;
         Bligaard, T.; Nørskov, J. K. _J. Catal._ **2004,** _223,_ 232.

(67)   Joseph, S. T. S.; Ipe, B. I.; Pramod, P.; Thomas, K. G. _J. Phys. Chem. B_
         2006, _110,_ 150.

(68)   Liao, H. W.; Hafner, J. H. _Chem. Mater._ **2005,** _17,_ 4636.

(69)   Orendorff, C. J.; Murphy, C. J. _J. Phys. Chem. B_ **2006,** _110,_ 3990.

(70)   Alivisatos, P. _Nat. Biotechnol._ **2004,** _22,_ 47.

(71)   El-Sayed, I. H.; Huang, X.; El-Sayed, M. A. _Nano Lett._ **2005,** _5,_ 829.

(72)   El-Sayed, I. H.; Huang, X.; El-Sayed, M. A. _Cancer Lett._ **2006,** _239,_ 129.

(73)   Huang, X.; El-Sayed, I. H.; Qian, W.; El-Sayed, M. A. _J. Am. Chem. Soc._
         2006, _128,_ 2115.

(74)   Fahmy, T. M.; Fong, P. M.; Goyal, A.; Saltzman, W. M. _Mater. Today_
         2005, _8,_ 18.

(75)   Weissleder, R. _Nat. Biotechnol._ **2001,** _19,_ 316.

(76)   Evanoff Jr., D. D.; Chumanov, G. _ChemPhysChem_ **2005,** _6,_ 1221.

(77)   Dresselhaus, M. S.; Dresselhaus, G.; Eklund, P. C. _Science of Fullerenes_
         and Carbon Nanotubes, Academic Press, San Diego, CA, 1996.

(78)   Vivekchand, S. R. C.; Govindaraj, A.; Rao, C. N. R. in *Nanomaterials Chemistry Recent Developments and New Directions*, (Eds: Rao, C. N. R.; Müller, A.; Cheetham, A. K.), WILEY-VCH, Weinheim, 2007, p 45.

(79)   O'Connell, M. J.; Bachilo, S. M.; Huffman, C. B.; Moore, V. C.; Strano, M. S.; Haroz, E. H.; Rialon, K. L.; Boul, P. J.; Noon, W. H.; Kittrell, C.; Ma, J.; Hauge, R. H.; Weisman, R. B.; Smalley, R. E. *Science* **2002**, *297*, 593.

(80)   Avouris, P. *Acc. Chem. Res.* **2002**, *35*, 1026.

(81)   Ajayan, P. M. *Chem. Rev.* **1999**, *99*, 1787.

(82)   Wong, S. S.; Joselevich, E.; Woolley, A. T.; Cheung, C. L.; Lieber, C. M. *Nature* **1998**, *394*, 52.

(83)   Ebbesen, T. W.; Lezec, H. J.; Hiura, H.; Bennett, J. W.; Ghaemi, H. F.; Thio, T. *Nature* **1996**, *382*, 54.

(84)   Rinzler, A. G.; Hafner, J. H.; Nikolaev, P.; Nordlander, P.; Colbert, D. T.; Smalley, R. E.; Lou, L.; Kim, S. G.; Tomanek, D. *Science* **1995**, *269*, 1550.

(85)   de Heer, W. A.; Châtelain, A.; Ugarte, D. *Science* **1995**, *270*, 1179.

(86)   Javey, A.; Guo, J.; Wang, Q.; Lundstrom, M.; Dai, H. *Nature* **2003**, *424*, 654.

(87)   Postma, H. W. C.; Teepen, T.; Yao, Z.; Grifoni, M.; Dekker, C. *Science* **2001**, *293*, 76.

(88)   Charlier J.-C. *Acc. Chem. Res.* **2002**, *35*, 1063.

(89)   Hamada, N.; Sawada, S.; Oshiyama, A. *Phys. Rev. Lett.* **1992**, *68*, 1579.

(90)   Saito, R.; Fujita, M.; Dresselhaus, G.; Dresselhaus, M. S. *Appl. Phys. Lett.* **1992**, *60*, 2204.

(91)   Mintmire, J. W.; Dunlap, B. I.; White, C. T. *Phys. Rev. Lett.* **1992**, *68*, 631.

(92)   Hamon, M. A.; Itkis, M. E.; Niyogi, S.; Alvaraez, T.; Kuper, C.; Menon, M.; Haddon, R. C. *J. Am. Chem. Soc.* **2001**, *123*, 11292.

(93)   Krätschmer, W.; Lamb, L. D.; Fostiropoulos, K.; Huffman, D. R. *Nature* **1990**, *347*, 354.

(94)   Ando, Y.; Iijima, S. *Jpn. J. Appl. Phys.* **1993**, *32*, L107.

(95)   Ando, Y.; Ohkohchi, M. *J. Cryst. Growth* **1982**, *60*, 147.

(96) Iijima, S. *Nature* **1991**, *354*, 56.

(97) Zhao, X. *Bull. Res. Inst. Meijo Univ.* **1996**, *1*, 7.

(98) Zhao, X.; Ohkohchi, M.; Wang, M.; Iijima, S.; Ichihashi, T.; Ando, Y. Carbon, **1997**, *35*, 775.

(99) Ando, Y.; Zhao, X.; Sugai, T.; Kumar, M. *Mater. Today* **2004**, *7*, 22.

(100) Journet, C.; Maser, W. K.; Bernier, P.; Loiseau, A.; Chapelle, M. L.; Lefrant, S.; Deniard, P.; Lee, R.; Fischer, J. E. *Nature* **1997**, *388*, 756.

(101) Powers, D. E. et al., *J. Chem. Phys.* **1982**, *86*, 2556.

(102) Bernstein, E. R. (ed.), *Atomic and Molecular Clusters, Elsevier Science B, New York*, 1990, 69.

(103) Guo, T.; Diener, M. D.; Chai, Y.; Alford, M. J.; Haufler, R. E.; McClure, S. M.; Ohno, T.; Weaver, J. H.; Scuseria, G. E.; Smalley R. E. *Science* **1992**, *257*, 1661.

(104) Thess, A.; Lee, R.; Nikolaev, P.; Dai, H.; Petit, P.; Robert, J.; Xu, C.; Lee, Y. H.; Kim, S. G.; Rinzler, A. G.; Colbert, D. T.; Scuseria, G. E.; Tománek, D.; Fischer, J. E.; Smalley, R. E. *Science* **1996**, *273*, 483.

(105) Baker, R. T. K. in *Chemistry and Physics of Carbon*, (Eds: Walker, P. L., Thrower, P. A.), *Marcel Dekker*, New York, 1978, 14.

(106) Dai, H.; Rinzler, A. G.; Nikolaev, P.; Thess, A.; Colbert, D. T.; Smalley, R. E. *Chem. Phys. Lett.* **1996**, *260*, 471.

(107) (a) Guldi, D. M.; Rahman, G. M. A.; Zerbetto, F.; Prato, M. *Acc. Chem. Res.* **2005**, *38*, 871; (b) Tasis, D.; Tagmatarchis, N.; Bianco, A.; Prato, M. *Chem. Rev.* **2006**, *106*, 1105; (c) Prato, M.; Kostarelos, K.; Bianco, A. *Acc. Chem. Res.* **2008**, *41*, 60.

(108) Andreas, H. *Angew. Chem. Int. Ed.* **2002**, *41*, 1853.

(109) Khlobystov, A. N.; Britz, D. A.; Briggs, G. A. D. *Acc. Chem. Res.* **2005**, *38*, 901.

(110) Smith, B. W.; Monthioux, M.; Luzzi, D. E. *Nature* **1998**, *396*, 323.

(111) Kauffman, D. R.; Star, A. *Small* **2007**, *3*, 1324.

(112) Jonge, N. de.; Lamy, Y.; Schoots, K.; Oosterkamp, T. H. *Nature* **2002**, *420*, 393.

(113) Kiebele, A.; Grüner, G. *Appl. Phys. Lett.* **2007**, *91*, 144104.

(114) Pushparaj, V. L.; Shaijumon, M. M.; Kumar, A.; Murugesan, S.; Ci, L.; Vajtai, R.; Linhardt, R. J.; Nalamasu, O.; Ajayan, P. M. *Proc. Natl. Acad. Sci. U. S. A.* **2007**, *104*, 13574.

(115) Kamat, P. V. *Nanotoday* **2006**, *1*, 20.

(116) (a) Campidelli, S.; Sooambar, C.; Lozano-Diz, E.; Ehli, C.; Guldi, D. M.; Prato, M. *J. Am. Chem. Soc.* **2006**, *128*, 12544; (b) Alvaro, M.; Aprile, C.; Ferrer, B.; Garcia, H. *J. Am. Chem. Soc.* **2007**, *129*, 5647; (c) Kongkanand, A.; Kamat, P. V. *ACS Nano* **2007**, *1*, 13.

(117) (a) Pantarotto, D.; Singh, R.; McCarthy, D.; Erhardt, M.; Briand, J.-P.; Prato, M.; Kostarelos, K.; Bianco A. *Angew. Chem. Int. Ed.* **2004**, *43*, 5242; (b) Lacerda, L.; Raffa, S.; Prato, M.; Bianco, A.; Kostarelo, K. *Nanotoday* **2007**, *2*, 38.

CHAPTER 2

Synthesis and Photophysical Properties of Ruthenium Trisbipyridine Functionalized Gold Nanoparticles

2.1. Abstract

Two nanohybrid systems were synthesized by functionalizing one of the most versatile chromophoric systems, namely ruthenium trisbipyridine ($Ru(bpy)_3^{2+}$) on the surface of gold nanoparticles and their photophysical properties were investigated. By adopting a place exchange reaction, $Ru(bpy)_3^{2+}$ bearing thiols (possessing methylene chains of different lengths; **Ru-C$_3$-SH** and **Ru-C$_7$-SH**) were functionalized onto Au nanoparticles capped with triethylene glycol thiols (**Au(S-EG$_3$)$_x$**). The place exchange reaction was successful in linking a desired number of $Ru(bpy)_3^{2+}$ on Au nanoparticles; in the case of **Ru-C$_7$-SH**, a higher loading of ~145 chromophores and a lower loading of ~50 chromophores were achieved. Based on HRTEM studies, the average diameter of **Au(S-EG$_3$)$_x$** nanoparticles was estimated to be ~4.5 nm and no appreciable change in the diameter was observed after the place exchange reaction. The mixed monolayers were further characterized using UV-visible and ^{1}HNMR spectroscopy. The photophysical properties of these hybrid systems were investigated by following time resolved luminescence and transient absorption studies. At higher loadings of $Ru(bpy)_3^{2+}$, a biexponential decay

with a long lived component, corresponding to unquenched chromophores, and a short lived component due to either electron/energy transfer process was observed. However, the quenching process was not observed at lower loadings of $Ru(bpy)_3^{2+}$ chromophores. Based on transient absorption studies it was further confirmed that the quenching originates, at higher chromophoric loadings, from a light induced electron transfer from the excited state of $Ru(bpy)_3^{2+}$ to its ground state.

2.2. Introduction

The multifaceted properties of matter in nanoscale dimension offers a wide range of research and development possibilities in diverse areas of photonics, electronics, material science, catalysis and biology.[1-11] An in-depth understanding on the optical as well as electronic properties of nanoparticles is essential for designing optoelectronic and photonic devices with reduced dimensions.[7,8] For example, the unique ability of metal nanoparticles to store and transport electrons make them promising candidates for the design of optoelectronic devices.[12-15] Modification of the surface of metal nanoparticles with fluorophores is important for designing biological sensors[16] and artificial solar energy harvesting devices.[17-22] Various aspects dealing with the photophysical and electrochemical properties of chromophore functionalized metal nanoparticles have already been documented in recent reviews[3-8] and theses.[23-25] It is generally believed that the emission of chromophores is totally quenched when bound on to the surface of metals through an energy transfer process.[26] However, recent studies have revealed that the emission of chromophores

is retained when thickly packed on Au nanoparticles.[4,9,27-31] It has also been demonstrated that the energy as well as electron transfer processes from chromophores is dependant on the size of the nanoparticles.[4,9,30,31] Interestingly, smaller Au nanoparticles in the size domain of 2-5 nm has the ability to store and shuttle electrons.[4,32] Chromophore functionalized nanoparticles are useful as elements in nanophotonic devices and the efficiency of electron/energy transfer processes depend on several factors. These include the (i) redox property of chromophores, (ii) density of chromophores on nanoparticle surface, (iii) separation of chromophore from metal surface, (iv) nature of linker group and (v) size of metal nanoparticles.

For investigating the electron/energy transfer processes in functionalized Au nanoparticles, we have selected one of the most versatile chromophoric systems namely ruthenium trisbipyridine, (**Ru(bpy)$_3$$^{2+}$**), which is often called as the "king of inorganic complexes".[33] Ruthenium(II) trisbipyridyl based complexes possess remarkable chemical stability and unique photophysical properties (*vide infra*) and these aspects are well documented.[33-36] This class of molecule has been extensively utilized for solar energy harvesting[37,38] and other applications.[39,40] A brief summary of the ground and excited state properties of **Ru(bpy)$_3$$^{2+}$** chromophore is summarized below.

Ruthenium trisbipyridine chromophore possess an octahedral geometry with D_3 symmetry.[41] The absorption spectrum in the visible region is dominated by an intense metal-to-ligand charge transfer (^{1}MLCT) band at 450 nm ($\varepsilon \sim 10^4$ M^{-1}cm^{-1}), caused by the transition from a d$_\pi$ metal

orbital to a ligand based orbital ($\pi_L{}^*$). The ^{1}MLCT state rapidly decays, within 300 fs, *via* intersystem crossing (ISC) to a ^{3}MLCT excited state which has an emission quantum yield (ϕ) of 0.06 and lifetime (τ) of around 0.9 μs in acetonitrile at room temperature (Figure 2.1). The ^{3}MLCT state of $Ru(bpy)_3{}^{2+}$ is sufficiently long lived, so that it undergoes efficient energy or electron transfer with other molecules (quencher).
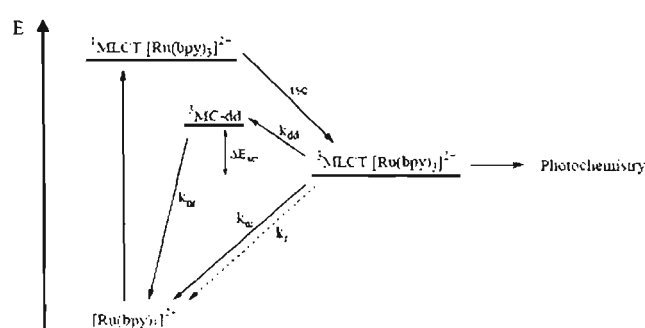
Figure 2.1. Formation and deactivation pathways for the ^{3}MLCT excited state of $Ru(bpy)_3{}^{2+}$ (*adapted from reference 41*).

The electron/energy transfer process between Au nanoparticles and fluorescent molecules have been investigated extensively and well documented.[4,9,30,31] However, there are only few investigations on the interaction of Au nanoparticles and molecular systems which possess long lived emission (for e.g., $Ru(bpy)_3{}^{2+}$ based luminescent systems).[42-54] A few approaches have been reported in the literature for assembling ruthenium polypyridines onto Au nanoparticles; however, the rich photochemistry of this class of hybrid systems has not been well exploited.[42-54] More recently, Klar and co-workers have examined the radiative and nonradiative decay channels of $Ru(bpy)_3{}^{2+}$ when bound on

Au nanoparticles.[54] **Ru(bpy)$_3$$^{2+}$** were attached to Au nanoparticles having diameters of 20 nm as well as 40 nm through biotin-streptavidin interaction at a distance of approximately 4 nm from the nanoparticle surface (Figure 2.2).[54] Time-resolved luminescence spectroscopy revealed an increase of the radiative as well as the nonradiative rate when the phosphors were bound on to the Au nanoparticles. While the increase of the radiative rate would increase the phosphorescence quantum yield, the more prominent increase of the nonradiative rate outweighs this effect, so that net quenching in luminescence occurs.

Figure 2.2. Gold nanoparticles having diameters of 20 and 40 nm functionalized with streptavidin and the remaining gaps sealed with either BSA or PEG. The biotinylated phosphorescent metal complexes **Ru(bpy)$_3$$^{2+}$** are attached to the nanoparticles *via* streptavidin-biotin recognition (*adapted from reference 54*)
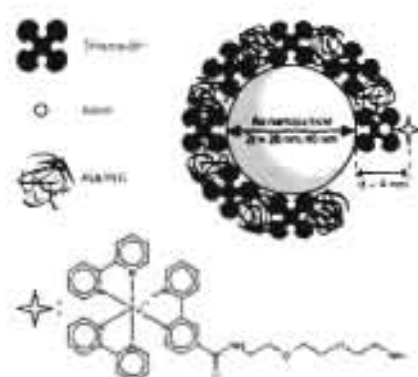
In another report, quenching of the luminescence of **Ru(bpy)$_3$$^{2+}$** and **Os(bpy)$_3$$^{2+}$** based phosphors were observed when adsorbed directly on to Au nanoparticles or bound electrostatically very close to the nanoparticles' surface.[52,53] Authors conclude that the quenching occurs through an electron transfer from **Ru(bpy)$_3$$^{2+}$/Os(bpy)$_3$$^{2+}$** when adsorbed on to

nanoparticle.[52] In contrast, the luminescence decrease was considered to be due to an energy transfer process for the electrostatically bound **Ru(bpy)₃²⁺**.[53] In the above cases, polypyridine complexes are bound on to Au nanoparticles through non-covalent interactions, which limit the control of the number of chromophores. This prevents the possibility of investigating the excited state interactions in these systems as a function of the concentration of chromophores on the nanoparticle surface. An effective approach for varying the concentrations of **Ru(bpy)₃²⁺** chromophore on to the surface of gold nanoparticles and thereby tuning their photophysical properties are presented in this Chapter. The ruthenium(II) trisbipyridyl were linked to thiol groups through methylene chains of two different lengths (**Ru-C₃-SH** and **Ru-C₇-SH** in Chart 2.1) and were functionalized on to Au nanoparticles by adopting a place exchange reaction. Various steps involved in the synthesis of ruthenium(II) trisbipyridyl complexes, (**Ru-C₃-SH** and **Ru-C₇-SH**), triethylene glycol thiol capped Au nanoparticles and their place exchange reactions are presented in Scheme 2.1-2.3. Details of the various synthetic steps and characterization of various intermediates and products are provided in the Experimental Section 2.6.
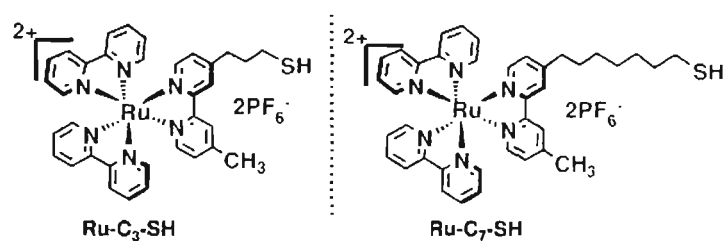
Chart 2.1

2.3. Results and Discussion

2.3.1. Synthesis and Characterization

Synthesis of ruthenium thiols, **Ru-C$_3$-SH** and **Ru-C$_7$-SH**. were carried out as per Scheme 2.1. The monobromoalkyl bipyridine derivatives (**2a** and **2b**) were prepared through a nucleophilic reaction of 4,4'-dimethyl 2,2'-bipyridine with the corresponding α,ω-dibromoalkanes, using lithium diisopropylamine as the base.[55] The corresponding bromo-derivatives
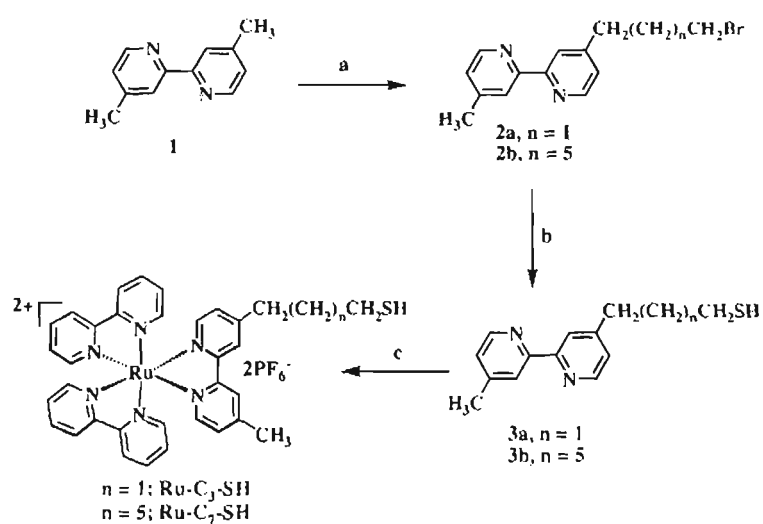
Scheme 2.1. (a) Br(CH$_2$)$_n$Br, BuLi, DISPA, THF; (b) hexamethyldisilathiane, tetrabutylammonium fluoride, THF, -10°C; (c) Ru(bpy)$_2$Cl$_2$, ethanol/water, reflux.

were converted to thiols by reacting with a mixture of tetrabutylammonium fluoride and hexamethyldisilathiane, by following a general method reported by Fox and coworkers[56] for the synthesis of thiols. The thiol-derivatives were further complexed with **Ru(bpy)$_2$Cl$_2$**, by adopting a general procedure,[57] to yield ruthenium chromophores possessing alkyl

spacers of varying chain lengths (denoted as **Ru-C$_3$-SH** and **Ru-C$_7$-SH**). Details of the synthesis and spectral characterization of various intermediates and final products are provided in the Experimental Section.

The most widely used method for the functionalization of organic molecules as monolayers on the surface of gold nanoparticles adopts a two phase synthesis reported by Brust *et al.*[58] and their modified procedures.[59] Alternately, metal nanoparticles bearing mixed monolayers can be conveniently synthesized using ligand exchange (place exchange) reactions.[60,61] In the present study, we have used octylmercaptan (**C$_8$H$_{17}$SH**) as well as monothiol derivative of triethylene glycol (**EG$_3$-SH**, Scheme 2.2) as ligands for preparing monolayer protected gold nanoparticles (denoted as **Au(SC$_8$H$_{17}$)$_x$** and **Au(S-EG$_3$)$_x$**[62] respectively,
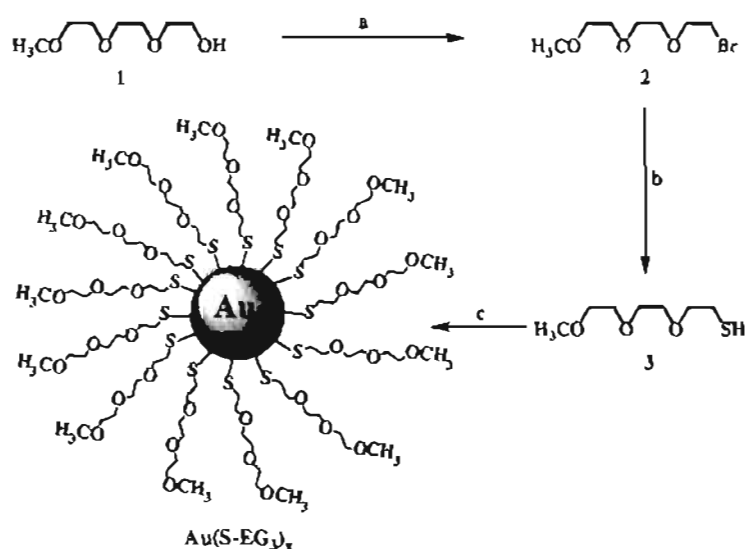
Scheme 2.2. (a) PBr$_3$, pyridine, CHCl$_3$; (b) thiourea, NaOH, ethanol/water; (c) HAuCl$_4$, methanol/acetic acid.

where 'x' indicates the average number of molecules of capping agents). Synthesis of gold nanoparticles functionalized with **EG$_3$-SH** was carried out by adopting a modified literature procedure (Section 2.6).[62]

Several attempts have been made to functionalize **Ru-C$_3$-SH/Ru-C$_7$-SH** on to Au nanoparticle surfaces. The two-phase synthetic procedure adopted by co-binding the chromophores with **C$_8$H$_{17}$SH** and the ligand exchange reaction carried out by reacting with **Au(S-C$_8$H$_{17}$)$_x$**, were not successful. Both these methods resulted in the precipitation of the nanoparticles which may be due to the noncompatibility of the two molecules on Au surface: the shell of octanethiolate protecting the gold nanoparticles is nonpolar in nature, whereas, the **Ru(bpy)$_3$$^{2+}$** chromophores are polar in nature. Interestingly, the place exchange reaction with **Au(S-EG$_3$)$_x$** (possess polar triethylene glycol as capping agent) and **Ru-C$_3$-SH/Ru-C$_7$-SH** yielded gold nanoparticles having mixed monolayers denoted as **Au(S-EG$_3$)$_{x-y}$(S-C$_3$-Ru)$_y$** and **Au(S-EG$_3$)$_{x-y}$(S-C$_7$-Ru)$_y$**. For simplicity of representation, these hybrid nanoparticles, bearing mixed monolayers. are abbreviated as **Au(S-C$_3$-Ru)** and **Au(S-C$_7$-Ru)** in the subsequent Sections. In a typical synthesis of **Au(S-C$_7$-Ru)**. to a stirring solution of **Au(S-EG$_3$)$_x$** (0.5 mL, 1.5 mmol) in dichloromethane was added 1 mL solution of **Ru-C$_7$-SH** (5 mg, 3 mmol). The reaction mixture was stirred at room temperature for 36 h and centrifuged (four times at 4000 rpm, for 5 min each) to remove the unbound **Ru-C$_7$-SH**. Both **Au(S-C$_3$-Ru)** and **Au(S-C$_7$-Ru)** are highly soluble in CH$_3$CN and partially soluble in CH$_2$Cl$_2$, whereas, the starting materials are highly soluble in CH$_2$Cl$_2$. This allowed the purification of mixed monolayer functionalized gold

nanoparticles by first dissolving the crude product in CH_2Cl_2 followed by centrifuging. Purification procedure was followed using UV-visible spectroscopic studies and found that the unbound chromophores were absent in the filtrate after four cycles of centrifugation. We have varied the surface coverage of $Ru-C_3-SH/Ru-C_7-SH$ by varying the concentration of chromophores during the place exchange reaction (Scheme 2.3). Purified nanoparticles were redispersed in acetonitrile and characterized using microscopic and spectroscopic studies.

Scheme 2.3. Synthesis of ruthenium thiol functionalized gold nanoparticles, $Au(S-C_3-Ru)$.

The average number of photoactive molecules per nanoparticle plays a decisive role in tuning the photophysical properties. Place exchange reaction with different concentrations of $Ru-C_3-SH/Ru-C_7-SH$. enabled us to fix the desired number of $Ru(bpy)_3^{2+}$ chromophores around the Au nanoparticles. The average number of chromophores per Au nanoparticle was estimated in conjunction with transmission electron microscopy (TEM), inductively coupled plasma (ICP) analysis and UV-vis absorption spectroscopy (Appendix; Section 2.5). After the place exchange

reaction, the concentration of unreacted chromophore was estimated from the absorption spectra of the filtrate. In the present case, we have synthesized mixed monolayers bearing lower and higher loadings of $Ru(bpy)_3^{2+}$. It was estimated that samples possessing higher concentration of $Ru(bpy)_3^{2+}$ possesses ~145 chromophores on each Au nanoparticle, based on the assumption that all the reacted chromophores are evenly distributed on the nanoparticles. Mixed monolayers with lower loading of chromophores (~50 molecules of $Ru(bpy)_3^{2+}$ per particle) were prepared by decreasing the concentration of Ru-C_7-SH used for place exchange reaction, and these samples are denoted as $Au(S-C_7-Ru)_L$.

2.3.2. HRTEM Studies

The HRTEM samples of $Au(S-EG_3)_x$ and $Ru(bpy)_3^{2+}$ capped gold nanoparticles were prepared by drop-casting a dilute suspension on to a carbon-coated copper grid. Images presented in Figure 2.3A indicate the presence of monodispersed $Au(S-EG_3)_x$ nanoparticles having an average diameter of 4.5 nm. Interestingly no appreciable changes in the diameter

Figure 2.3. HRTEM images of (A) $Au(S-EG_3)_x$ and (B,C) $Au(S-C_7-Ru)$. Samples were prepared by drop-casting a dilute suspension on to a carbon coated copper grid.

of nanoparticles were observed after the place exchange reaction with **Ru-C₃-SH/Ru-C₇-SH** (Figure 2.3B). We have estimated the number of gold atoms as ~2770 by adopting a tight-packed spherical model suggested by Murray and coworkers.[63] The lattice planes observed in the HRTEM image (Figure 2.3C) indicate that the nanoparticles are highly crystalline in nature.

2.3.3. ¹HNMR Characterization

For further confirming the surface functionalization of **Ru(bpy)₃²⁺** chromophores on gold nanoparticles, ¹HNMR spectra of the unbound and bound ligands were recorded. The ¹HNMR spectra of **EG₃-SH** showed two signals at 1.5 and 2.6 ppm (trace 'a' in Figure 2.4); the triplet at 1.6 ppm is attributed to the thiol proton and the doublet of triplet at 2.6 ppm due to α-CH₂ protons. Upon functionalization, significant changes were observed in the spectral range 1.4-3.0 ppm (Figure 2.4). The thiol protons were not observed for **Au(S-EG₃)ₓ** confirming the functionalization of **EG₃-SH** on to Au nanoparticles and the multiplicity of the α-CH₂ got reduced to a triplet due to the absence of any interactions with the -SH proton (trace 'b' in Figure 2.4), similar to that reported by Zheng and coworkers.[62] Peaks in other regions of ¹HNMR spectrum remain more or less unaffected upon functionalization. Place exchange reaction with **Ru-C₇-SH/Ru-C₃-SH** was confirmed by the (i) disappearance of thiol proton and (ii) lowering of multiplicity of α-CH₂ to triplet (as compared to a doublet of triplet in **Ru-C₇-SH**), along with a broadening of peaks. ¹HNMR spectrum of **Ru-C₇-SH** and **Au(S-C₇-Ru)** are presented as traces 'c' and 'd' respectively in Figure

2.4. The singlet at 2.3 ppm corresponds to methyl protons of **EG₃-SH**. Two factors contribute to the peak broadening upon functionalization: the dipolar spin relaxation and the non-uniform distribution of thiolate ligands on the surface of Au nanoparticle.[59]

Figure 2.4. ¹HNMR spectra of various ligands unbound and bound on Au nanoparticles in the spectral range 1.5-2.6 ppm *(crossed peak corresponds to residual water peak in the solvent)*. (a) **EG₃-SH**, (b) **Au-(S-EG₃)ₓ**, (c) **Ru-C₇-SH** and (d) **Au(S-C₇-Ru)** in CD₃CN.

2.3.4. Steady State Absorption and Emission Studies

Argon degassed solution of ruthenium trisbipyridine were used for various steady-state and time-resolved investigations. Absorption spectra of **Ru-C₃-SH/Ru-C₇-SH** in acetonitrile possess two bands; one centered around 288 nm attributed to the π-π^* transition of bipyridine ligands and other at 453 nm due to the metal-to-ligand charge transfer (MLCT) band (trace 'a' in Figure 2.5A). The photophysical properties of **Ru-C₃-SH/Ru-C₇-SH** in CH₃CN are summarized in Table 2.1. The absorption spectral features corresponding to the MLCT band of **Ru(bpy)₃²⁺** (trace 'a') and surface plasmon band of Au nanoparticles (trace 'b') were more or less retained in the case of **Au(S-C₇-Ru)**, ruling out the possibility of any strong ground state interaction (trace 'c'). Similar results were observed for **Au(S-C₃-Ru)**.

The emission spectra of **Ru-C₃-SH/Ru-C₇-SH** were centered at 612 nm (trace 'a' in Figure 2.5B) and the luminescence quantum yield for both

Figure 2.5. Absorption and luminescence spectra of unbound and bound **Ru(bpy)₃²⁺** on Au nanoparticles in degassed CH₃CN: (A) absorption spectra of (a) **Ru-C₇-SH**, (b) **Au(S-EG₃)ₓ**, (c) **Au(S-C₇-Ru)** and (B) luminescence spectra of (a) **Ru-C₇-SH** and (b) **Au(S-C₇-Ru)**.

Table 2.1. Absorption and luminescence properties of **Ru-C₃-SH** and **Ru-C₇-SH** in degassed CH_3CN.

Compounds	ε (x 10^4 M^{-1} cm^{-1})		λ_{max} em/nm	Φ_{em}	τ_{ns}
	π-π* bpy (288 nm)	MLCT (453 nm)			
Ru-C₃-SH	8.12	1.41	617	0.070	960
Ru-C₇-SH	8.94	1.55	617	0.071	961

the compounds were estimated as 0.07 (error limit ± 5%) using **Ru(bpy)₃**$^{2+}$ as standard (ϕ_{em} for **Ru(bpy)₃**$^{2+}$ = 0.084)[64] and the spectral properties are summarized in the Table 2.1. At lower loadings of **Ru(bpy)₃**$^{2+}$ on Au nanoparticles, the luminescence is more or less retained (*vide infra*). Interestingly, we have observed that the luminescence of **Ru(bpy)₃**$^{2+}$ is quenched at higher loadings in the case of **Au(S-C₃-Ru)/Au(S-C₇-Ru)** (trace 'b' Figure 2.5B). However, the spectral overlap between the plasmon absorption of gold nanoparticles and the MLCT band of **Ru(bpy)₃**$^{2+}$ prevented the selective excitation of the chromophore and hence quantification of the emission yields by steady-state technique is difficult. The excited state interactions were further elucidated by following luminescent lifetime and nanosecond transient absorption studies.

2.3.5. Time-Resolved Luminescence Studies

Both **Ru-C₃-SH** and **Ru-C₇-SH** follows monoexponential decay in various solvents, with a lifetime (τ) of 1.11 μs in CH_2Cl_2 and 961 ns in CH_3CN, which is attributed to the inherent lifetime of the chromophore (for e.g., trace 'a' in Figure 2.6). Interestingly, **Ru(bpy)₃**$^{2+}$ functionalized on

gold nanoparticles follows biexponential decay in CH_2Cl_2 (ε = 9.8) with a long lived (τ_1 = 1.1 μs; χ_1 = 80%) and short-lived (τ_2 = 4.3 ns; χ_2= 20%) components. The lifetime of the long-lived component (similar to that of unbound **Ru-C$_3$-SH/Ru-C$_7$-SH**) can be attributed to the unquenched **Ru(bpy)$_3^{2+}$** chromophore bound on to gold nanoparticles. The short-lived component arises from the quenched excited state of **Ru(bpy)$_3^{2+}$**, either through an energy or electron-transfer process. In a polar solvent such as CH_3CN (ε = 39.8), the relative abundance of the short-lived component substantially increased (τ_1 = 960 ns; χ_1 = 30% and τ_2 = 4.3 ns; χ_2 = 70%), further supporting an electron-transfer quenching process (trace 'b' in Figure 2.6).

Figure 2.6. Luminescence lifetime profile of (a) **Ru-C$_7$-SH** and (b) **Au(S-C$_7$-Ru)** recorded in degassed CH_3CN (Excited at 440 nm).

Table 2.2. Luminescence lifetimes[a-c] of unbound and bound $Ru(bpy)_3^{2+}$ on Au nanoparticles.

Hybrid system	Solvent (dielectric constant)	τ_1, ns [a-c] (χ_1 %) [d]	τ_2, ns [a] (χ_2 %) [d]	χ^2 [e]
Ru-C₇-SH	acetonitrile (39.8)	961 (100%)	-	1.01
Au(S-C₇-Ru)	acetonitrile (39.8)	960 (30%)	4.2 (70%)	1.05
Au(S-C₇-Ru)	dichloromethane (9.8)	1100 (80%)	4.3 (20%)	1.10
Au(S-C₇-Ru)L	acetonitrile (39.8)	960 (100%)	-	1.02

[a]τ_1 and τ_2 corresponds to the lifetime of long-lived and short-lived components; [b]error limit ± 5%; [c]excited at 440 nm; [d]χ_1 and χ_2 corresponds to the fractional contribution of τ_1 and τ_2 respectively; [e]the quality of the fit is judged by means of usual statistical parameters.

2.3.6. Nanosecond Transient Absorption Studies

Nanosecond laser flash photolysis was carried out for obtaining a better understanding on the mechanism of the quenching process. The difference absorption spectrum recorded following a 355 nm laser excitation of **Ru-C₃-SH/Ru-C₇-SH** in degassed CH_3CN solution possesses a well defined band at 370 nm, which is readily quenched in oxygenated solution. This absorption band is characteristic of the triplet-triplet absorption of $Ru(bpy)_3^{2+}$ (Figure 2.7A), and the absorption-time profile monitored at 370 nm follows a monoexponential decay with a lifetime of 909 ns (k_T = 1.10 x 10^6 s^{-1}, Figure 2.7B). The corresponding bleach around 450 nm and 620 nm is attributed to the loss of ground state absorption and emission respectively.

Figure 2.7. (A) Nanosecond transient absorption spectrum of **Ru-C$_7$-SH** in degassed CH$_3$CN and (B) the absorption-time profile at 370 nm. The spectrum was recorded immediately after 355 nm laser pulse excitation.

Interestingly, upon binding on to metal nanoparticles (**Au(S-C$_7$-Ru)**), two additional bands were observed at 308 and 520 nm, along with triplet absorption band (Figure 2.8A). The presence of oxygen has no major effect on the formation and decay of these transients, whereas, the triplet absorption band was totally quenched (Figure 2.8B). The absorption-time profile monitored at 308 nm as well as 520 nm follows monoexponential decay with a rate constant of 7.4×10^6 s^{-1} (τ = 135 ns), indicating that both the species originate from the same process (Figure 2.8C). Nanosecond transient absorption studies of **Au-(S-C$_3$-Ru)** also provided similar results.

Chemical[65,66] as well as electrochemical methods[67] have been earlier adopted for the characterization of the redox products of **Ru(bpy)$_3^{2+}$**: reduction to **Ru(bpy)$_3^{1+}$** results in absorption peaks at 350 and 500 nm and a strong absorption at 310 nm upon oxidation to **Ru(bpy)$_3^{3+}$**. Comparing these results with the transient absorption spectra presented in Figure 2.8, it is clear that the peaks originate through an excited state redox reaction resulting in the formation of **Ru(bpy)$_3^{1+}$** and **Ru(bpy)$_3^{3+}$**. Thus, the transient

Figure 2.8. Nanosecond transient absorption spectrum of **Au(S-C$_7$-Ru)** in CH$_3$CN: (A) degassed solution, (B) oxygenated solution and (C) absorption-time profile at 310 and 500 nm. All the spectra were recorded immediately after 355 nm laser pulse excitation.

decays at 308 and 500 nm were assigned as **Ru(bpy)$_3^{3+}$** and **Ru(bpy)$_3^{1+}$** arising from a light-induced electron transfer process between the excited state and ground-state molecules of **Ru(bpy)$_3^{2+}$** anchored on the surface of gold nanoparticles.

Both luminescence and nanosecond transient absorption studies of **(Au(S-C$_7$-Ru)$_L$** showed spectral behavior similar to that of **Ru-C$_7$-SH**, and no electron-transfer products were observed on decreasing the concentration of **Ru(bpy)$_3^{2+}$** (Figure 2.9). These results clearly indicate that the local concentration of the chromophores plays a decisive role in modulating the photophysics of the **Ru-(bpy)$_3^{2+}$**.

Figure 2.9. Photophysical properties of **Au(S-C$_7$-Ru)$_L$** in degassed CH$_3$CN: (A) absorption, (B) luminescence, (C) luminescence lifetime and (D) nanosecond transient absorption spectrum (The spectrum was recorded immediately after 355 nm laser pulse excitation).

Blank experiments were carried out using (i) a solution of **Ru-C$_7$-SH** in the presence of **EG$_3$-SH** and (ii) saturated solution of **Ru-C$_7$-SH.** Both these experiments did not produce any redox products, further confirming the role of gold nanoparticles in creating a micro-heterogeneous environment favorable for the electron transfer (Figure 2.10).

The nanohybrid system can be visualized as a core-shell system (Scheme 2.4) possessing several **Ru(bpy)$_3$$^{2+}$** chromophores at the periphery of gold nanoparticles in which the light-induced electron transfer generates oxidized and reduced products. Interestingly, electron transfer
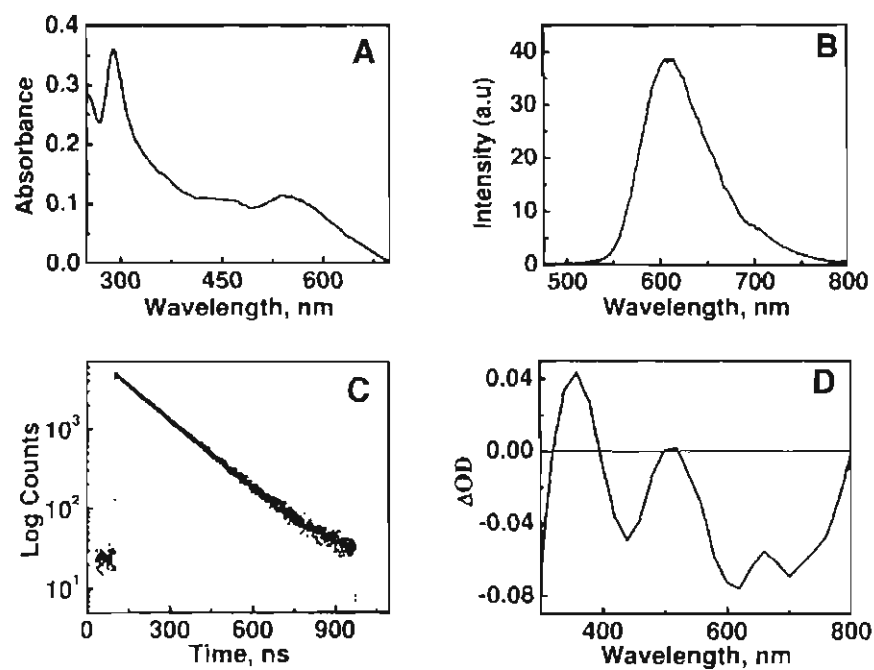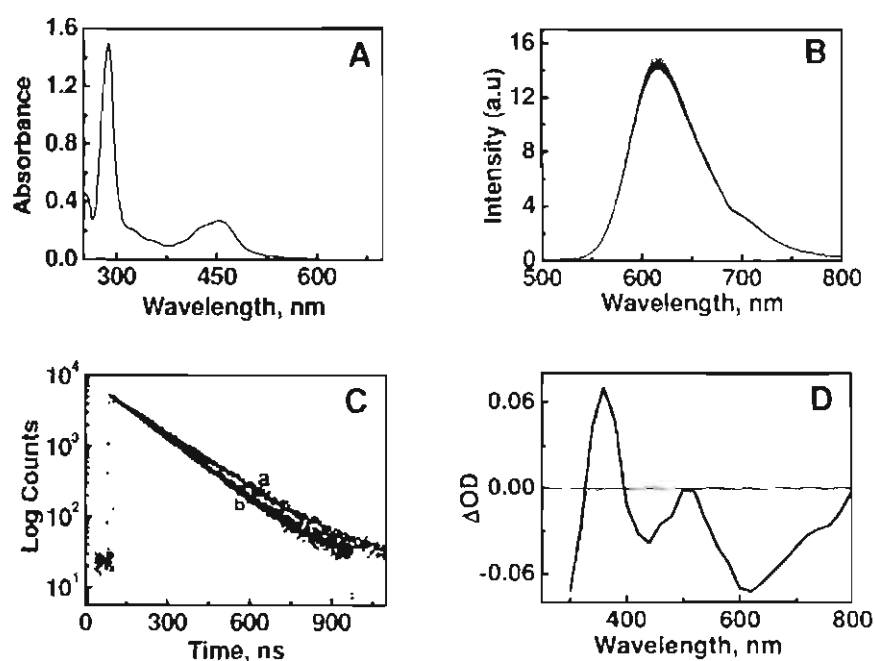
Figure 2.10. Photophysical properties of **Ru-C₇-SH** on the addition of **EG₃-SH** in degassed CH_3CN: (A) absorption, (B) luminescence, (C) luminescence lifetime (a) in presence and (b) absence of **EG₃-SH** and (D) nanosecond transient absorption spectrum (The spectrum was recorded immediately after 355 nm laser pulse excitation).

products sustained for several nanoseconds before undergoing recombination, probably due to the stabilizing effect of the polar ethylene glycol moieties embedded between the chromophoric groups. The density of **Ru(bpy)₃²⁺** chromophores in the monolayer, at lower and higher concentrations, was further estimated, and details are provided in the Section 2.5. At higher concentrations of **Ru(bpy)₃²⁺**, ~65% of the volume of the shell is occupied by the chromophore. Such dense packing of **Ru(bpy)₃²⁺** results in the formation of redox products upon photoexcitation (Figure 2.8). To the best of our knowledge, this is the first observation of a

light-induced charge shift from the excited to the ground-state of $Ru(bpy)_3^{2+}$ chromophores leading to the formation of redox products. Interestingly, the chromophore occupies ~23% of the total shell volume in the case of $Au-(S-C_7-Ru)_L$, and electron-transfer products were not observed (Figure 2.9).
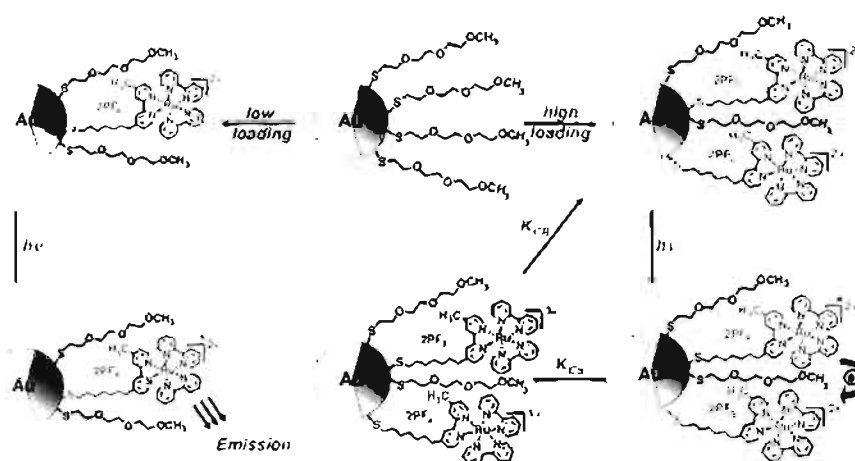
Scheme 2.4. Light induced processes in $Au(S-C_7-Ru)$ and $Au(S-C_7-Ru)_L$.

It is well established that the quantum size effects in Au nanoparticles are observed only when the diameter is <3.0 nm (transition from metal to semiconductor/insulator).[58] Photoinduced charge-transfer from the photoexcited $Ru(bpy)_3^{2+}$ chromophores to Au nanoparticles was not observed in the present case, which may be due to the large diameter of Au core (>4.5 nm). Attempts were made to synthesize $Au-(S-C_7-Ru)$ hybrid systems possessing Au core <2 nm. However, these experiments failed mainly due to the difficulties involved in the place exchange reaction between $Au(S-EG_3)_x$ having Au core <4.5 nm and $Ru-C_7-SH$, may be due to the larger volume occupied by $Ru(bpy)_3^{2+}$ chromophores.

2.4. Conclusions

An efficient approach for functionalizing a desired number of $Ru(bpy)_3^{2+}$ on Au nanoparticles through place exchange reaction was presented. Based on steady state and time resolved techniques, it was concluded that the loading of chromophores on the surface of gold nanoparticles plays a decisive role in modulating their photophysical properties. At higher loadings of $Ru(bpy)_3^{2+}$, a charge shift was observed between the chromophores leading to the formation of stable $Ru(bpy)_3^{3+}$ and $Ru(bpy)_3^{1+}$. The electron transfer products were found to be stable for several nanoseconds, probably due to the stabilizing effect of the polar ethylene glycol moieties embedded between the chromophoric groups. Interestingly, the luminescent properties of $Ru(bpy)_3^{2+}$ were retained by lowering the concentration of the chromophores on gold nanoparticles, and such hybrid systems could be further extended for the development of photocatalysts as well as chemical and biological sensors.

2.5. Appendix

Concentration of Au nanoparticles

$[Au^{3+}]$ = 0.24 mmol = 1.45 x 10^9 ions

Average size of Au nanoparticle[a] = 4.5 nm

Number of gold atoms per cluster[b] ~ 2769

Concentration of Au nanoparticles = 1.45 x 10^9/ 2769 = 5.3 x 10^{15}

Concentration of $Ru(bpy)_3^{2+}$ on $Au(S-C_7-Ru)$

$[Ru-C_7-SH]^c$ = 1.26 μmol =7.6 x 10^{17} moelcules

Number of $Ru(bpy)_3^{2+}$ chromophores per cluster[d] = 7.6 x 10^{17}/5.23 x 10^{15}

~ **145 molecules**

Concentration of $Ru(bpy)_3^{2+}$ on $Au(S-C_7-Ru)_L$

$[Ru-C_7-SH]^c$ = 0.44 μmol = 2.65 x 10^{17} moelcules

Number of Ru $(bpy)_3^{2+}$ chromophores per cluster[d] = 2.65 x 10^{17}/5.23 x 10^{15}

~ **50 molecules**

Percentage volume occupied by $Ru(bpy)_3^{2+}$ in the monolayer

(i) $Au(S-C_7-Ru)$

Volume of Au nanoparticle core (*radius = 2.25 nm*) = <u>4.77 x 10^{-20} cm^3</u>

Volume of $Au(S-C_7-Ru)$ core-shell structure (*radius = 3.65 nm*)

= <u>2 x 10^{-19} cm^3</u>

---

[a] based on TEM and tightly packed spherical model.

[b] based on tightly packed spherical model.

[c] concentration of unbound molecules in the filtrate was estimated and subtracted.

[d] on the assumption that the distribution of chromophores is uniform on the nanoparticles.

Volume occupied by monolayer = 2×10^{-19} cm^3 – 4.77×10^{-20} cm^3

$$= \underline{\mathbf{1.5 \times 10^{-19} \text{ cm}^3}}$$

Molecular volume of **Ru(bpy)$_3$$^{2+}$** in the shell

$$= \underline{7.2 \times 10^{-22} \text{ cm}^3}$$

Volume of 145 molecules of **Ru(bpy)$_3$$^{2+}$** = $145 \times 7.2 \times 10^{-22}$ cm^3

$$= \underline{1 \times 10^{-19} \text{ cm}^3}$$

Percentage volume occupied by 145 molecules of **Ru(bpy)$_3$$^{2+}$** in the monolayer
$$= 1 \times 10^{-19}/1.5 \times 10^{-19} = \underline{\mathbf{65 \%}}$$

(ii) Au(S-C$_7$-Ru)$_t$

Volume of 50 molecules of **Ru-C$_7$-SH** = $50 \times 716.93 \times 10^{-24}$ cm^3

$$= \underline{3.58 \times 10^{-20} \text{ cm}^3}$$

Space occupied by 50 molecules of **Ru-C$_7$-SH** in the shell of monolayer
$$= 3.58 \times 10^{-20}/1.5 \times 10^{-19} = \underline{\mathbf{23 \%}}$$

2.6. Experimental Section

2.6.1 Materials and Instrumental Techniques

Solvents and reagents used were purified and dried by standard methods. All starting compounds and reagents were purchased from Sigma-Aldrich and were used as such. Photophysical studies were carried out using spectroscopic grade solvents. All melting points were determined with a Mel-Temp-II melting point apparatus. ^{1}H and ^{13}C NMR spectra were measured on a Bruker DPX-300 MHz spectrometer. IR spectra were recorded on IRPrestige-21, Shimadzu infrared spectrophotometer. Mass spectra were recorded on JEOL JM AX 5505 mass spectrometer. The UV-vis spectra were recorded on a Shimadzu 2401 or 3101PC spectrophotometer. The emission spectra were recorded on a Spex-

Fluorolog, F112-X equipped with a 450W Xe lamp and a Hamamatsu R928 photomultiplier tube. The spectra were recorded by keeping a 90° geometry and a slit width of 1 nm in the excitation and emission monochromators. For the TEM analyses, samples were prepared by drop casting dilute solution from the cuvette on a carbon coated Cu grid and the solvent was allowed to evaporate and specimens were examined on a 300 kV (JEOL 3010) transmission electron microscope.

Luminescence lifetimes were measured using IBH (Florocube) Time-Correlated Picosecond Single Photon Counting (TCSPC) system. Solutions were excited with a pulsed diode laser (<100 ps pulse duration) at a wavelength of 440 nm (NanoLED) with a repletion of 100 kHz. The detection system consisted of a micro channel plate photomultiplier (5000U-09B, Hamamastu) with a 38.6 ps response time coupled to a monochromator (500M) and TCSPC electronics (Data Station Hub including Hub-NL, NanoLED controller and preinstalled luminescence measurement and analysis studio (FMAS) software). The luminescence lifetime values were obtained using DAS6 decay analysis software. The quality of the fit has been judged by the fitting parameters such χ^2 (1 ± 0.1) as well as the visual inspection of the residuals. Nanosecond laser flash photolysis experiments were carried out using an Applied Photophysics Model LKS-20 Laser Spectrometer using the third harmonic (355 nm) of a Qunta Ray GCR-12 series pulsed Nd:YAG laser with a pulse duration of ~8 ns.

2.6.2. Synthesis of 4-(3-bromopropyl)-4'-methyl-2,2'-bipyridine, 2a

To a degassed solution of lithium diisopropyl amine (1 equiv., prepared by mixing 2 mL of butyl lithium and 1mL of diisopropyl amine in dry THF) was added 4,4' dimethyl 2,2' bipyridine (500 mg, 2.71 mmol) at -15°C. The resulting solution was stirred at this temperature for 1 h to stabilize the monoanion produced. To the above stirring solution 1,2 dibromoethane (2.4 mL, 27.1 mmol) was added at -15°C and stirred at room temperature for 12 h. The reaction mixture was quenched with ice to remove excess LDA and then concentrated to remove the THF. Crude product was dissolved in dichloromethane and extracted with water to remove the inorganic salts. The organic washings were concentrated and column chromatographed over silica gel (100-200 mesh) using 20% ethyl acetate/hexane mixture to give 400 mg of **2a** (53%) having a melting point 68-70°C. ^{1}H NMR (CDCl$_3$, 300 MHz, TMS) δ 2.12-2.55 (m, 7H, aliphatic), 3.30-3.33 (t, 2H, CH$_2$Br), 7.02-7.08 (d, 2H, aromatic), 8.40 (s, 2H, aromatic), 8.61-8.65 (d, 2H, aromatic) ppm; ^{13}C NMR (CDCl$_3$, 75 MHz) δ 24.62, 28.85, 33.33, 34.71, 124.56, 125.31, 148.52, 149.76, 155.85 ppm; Mass-FAB: [M[+]] 290.11 (calculated 290.04), [M+2] 292.12 (calculated 292.04).

2.6.3. Synthesis of 3-(4'-methyl-2,2'-bipyridin-4-yl)propane-1-thiol, 3a

A mixture of tetrabutylammonium fluoride (98 mg, 0.38 mmol) and hexamethyldisilathiane (73 mg, 0.4 mmol) in THF (10 mL) was added to compound **2a** (100 mg, 0.35 mmol) in THF (10 mL) kept at -10°C. The mixture was allowed to warm to room temperature, while being stirred and

was further stirred at room temperature for 12 h. The reaction mixture was concentrated to remove THF and diluted with dichloromethane and then washed with saturated ammonium chloride solution. The organic layer was concentrated and column chromatographed over alumina using 10% ethyl acetate/hexane as eluent to give 50 mg of **3a** (62%) having melting point 65-67°C. ^{1}H NMR (CDCl$_3$, 300 MHz, TMS) δ 1.51-1.56 (t, 1H, thiol), 1.92-2.56 (m, 9H, aliphatic), 7.02- 7.09 (d, 2H, aromatic), 8.43 (s, 2H, aromatic), 8.65-8.69 (d, 2H, aromatic) ppm; ^{13}C NMR (CDCl$_3$, 75MHz) δ 24.62, 28.85, 33.33, 34.71, 124.56, 125.31, 148.52, 149.76, and 155.85 ppm; Mass-FAB: [M$^+$] 244.11 (calculated 244.10).

2.6.4. Synthesis of Ru-C$_3$-SH

To a stirring solution of the **3a** (50 mg, 0.2 mmol) in 1:1 mixture of ethanol:water (4 mL), same equivalents of **Ru(bpy)$_2$Cl$_2$** (100 mg, 0.2 mmol) in 1:1 mixture of ethanol:water (4 mL) was added and the reaction mixture was allowed to stir at reflux at 80°C for 8 h. The reaction mixture is concentrated to remove the solvent and an aqueous solution of ammonium hexafluorophosphate is added which results in the precipitation of the product in dark red color. Crude product was filtered, dissolved in acetonitrile and column chromatographed over silica gel (100-200 mesh) using 50% acetonitrile/dichloromethane as eluent to give 150 mg (90%) of the product. ^{1}H NMR (CDCl$_3$, 300 MHz, TMS) δ 1.51-1.56 (t, 1H, thiol), 1.92-2.56 (m, 9H, aliphatic), 7.02- 7.09 (m, 12H, aromatic), 8.43-8.52 (t, 6H, aromatic), 8.65-8.69 (m, 4H, aromatic) ppm; Exact mass calculated for

$C_{34}H_{32}N_6RuSPF_6$ [M-PF$_6$]$^+$ 803.1094, found 803.1090 (FAB, high-resolution mass spectroscopy).

2.6.5. Synthesis of 4-(7-bromoheptyl)-4'-methyl-2,2'-bipyridine, 2b

To a degassed solution of lithium diisopropyl amine (1 equiv; prepared by mixing 2 mL of butyl lithium and diisopropyl amine in dry THF) was added 4,4' dimethyl 2,2' bipyridine (500 mg, 2.71 mmol) at -15°C. The resulting solution was stirred at this temperature for 1 h to stabilize the monoanion produced. To the above stirring solution 1,6 dibromohexane was added at -15°C and stirred at room temperature for 12 h. The reaction mixture was quenched with ice to remove excess LDA and concentrated to remove the solvent. Crude product was dissolved in dichloromethane and extracted with water to remove the inorganic salts. The organic washings were concentrated and column chromatographed over silica gel (100-200 mesh) using 20% ethyl acetate/hexane mixture to give 700 mg of **2b** (75%) having a melting point 84-86°C. ^{1}H NMR (CDCl$_3$, 300 MHz, TMS) δ 1.29-2.56 (m, 13H, aliphatic), 3.30-3.34 (t, 2H, CH$_2$Br), 7.02- 7.09 (d, 2H, aromatic), 8.44 (s, 2H, aromatic), 8.61-8.69 (d, 2H, aromatic)ppm; ^{13}C NMR (CDCl$_3$, 75MHz) δ 24.62, 27.85, 29.21, 30.33, 31.52, 32.71, 33.71, 36.31, 124.56, 125.31, 148.52, 149.76, 155.85 ppm; Mass-FAB: [M$^+$] 346.07 (calculated 346.10), [M+2] 348.05 (calculated 348.10).

2.6.6. Synthesis of 7-(4'-methyl-2,2'-bipyridin-4-yl)heptane-1-thiol, 3b

A mixture of tetrabutylammonium fluoride (415 mg, 1.58 mmol) and hexamethyldisilathiane (308 mg, 1.7 mmol) in THF (10 mL) was added to

compound **2b** (500 mg, 1.4 mmol) in THF (10 ml) kept at -10°C. The mixture was allowed to warm to room temperature, while being stirred and was further stirred at room temperature for 12 h. The reaction mixture was concentrated to remove THF, diluted with dichloromethane and then washed with saturated ammonium chloride solution. The organic layer was concentrated and column chromatographed over alumina using 10% ethyl acetate/hexane as eluent to give 220 mg of **3b** (60%) having melting point 75-78°C. ^{1}H NMR (CDCl$_3$, 300 MHz, TMS) δ 1.51-1.55 (t, 1H, thiol), 1.92-2.56 (m, 17H, aliphatic), 7.02- 7.08 (d, 2H, aromatic), 8.42 (s, 2H, aromatic), 8.63-8.69 (d, 2H, aromatic); ^{13}CNMR (CDCl$_3$, 75MHz) δ 24.62, 28.85, 33.33, 34.71, 30.52, 124.56, 125.31, 148.52, 149.76, 155.12, 155.85 ppm; Mass-FAB: [M$^+$] 300.12 (calculated 300.17).

2.6.7. Synthesis of Ru-C$_7$-SH

To a stirring solution of the **3b** (150 mg, 0.5 mmol) in 1:1 mixture of ethanol:water (4 mL), same equivalents of **Ru(bpy)$_2$Cl$_2$** (240 mg, 0.5 mmol) in 1:1 mixture of ethanol:water (4 mL) was added and the reaction mixture was allowed to stir at reflux at 80°C for 8 h. The reaction mixture was concentrated to remove the solvent and an aqueous solution of ammonium hexafluorophosphate was added to the concentrated reaction mixture which resulted in the precipitation of the crude product in dark red color. The crude product was filtered, dissolved in acetonitrile and column chromatographed over silica gel (100-200 mesh) using 50% acetonitrile/dichloromethane as eluent to give 350 mg (85 %) of the product. ^{1}H NMR (CDCl$_3$, 300 MHz, TMS) δ 1.92-2.56 (m, 17H, aliphatic),

7.02- 7.09 (m, 12H, aromatic), 8.43-8.52 (t, 6H, aromatic), 8.65-8.69 (m, 4H, aromatic)ppm; Mass-FAB: [M-PF$_6$] 858.13 (calculated 858.21), [M-2PF$_6$] 714.21 (calculated 714.23).

2.6.8. Synthesis of Au(S-EG$_3$)$_x$

In a typical preparation of **Au(S-EG$_3$)$_x$** protected gold nanoparticles, 30 mL of MeOH (HPLC grade) and 5.0 mL of acetic acid were mixed in a 250 mL Erlenmeyer flask by stirring for 2-5 min. Then, 78.0 mg (0.2 mmol) of tetrachloroauric acid (HAuCl$_4$ XH$_2$O) (99.99%) and 13.6 mg (0.1 mmol) of monothiol of triethylene glycol (**EG$_3$-SH**) were added to the above mixed solvents and dissolved by stirring for 5 min, which gave a clear, yellow solution. Subsequently, a solution of sodium borohydride (75.0 mg, 2.0 mmol) dissolved in 5.0 mL of distilled water was added drop wise into the above solution with rapid stirring. On addition of the first drop of NaBH$_4$, the HAuCl$_4$ solution immediately turned to dark brown from yellow and rapid stirring was continued for 2 h. The reaction mixture was transferred into a 10 mL plastic centrifuging tube and centrifuged at 2500 rpm for 30 s to remove large particles, if there were any. The supernatant liquid was then filtered through a filter paper, concentrated under vacuum to remove methanol and acetic acid, washed several times with ether to remove the excess thiol. The product was dissolved in dichloromethane and extracted with water to remove excess sodium borohydride. The organic washings are dried over anhydrous Na$_2$SO$_4$, concentrated and redissolved in 10 mL of dichloromethane.

2.7. References

(1)   Katz, E.; Shipway, A. N.; Willner, I. in *Nanoscale Materials*, (Eds: Liz-Marzán, L. M.; Kamat, P. V.), Kluwer Academic Publishers, Boston, 2003, p 5.

(2)   Thomas, K. G. in *Nanomaterials Chemistry*, (Eds: Rao, C. N. R.; Müller, A.; Cheetham, A. K.), Wiley-VCH, Weinheim, Germany, 2007, p 185.

(3)   Shenhar, R.; Rotello, V. M. *Acc. Chem. Res.* **2003**, *36*, 549.

(4)   Thomas, K. G.; Kamat, P. V. *Acc. Chem. Res.* **2003**, *36*, 888.

(5)   Lewis, D. N. *Chem. Rev.* **1993**, *93*, 2693.

(6)   Rao, C. N. R.; Kulkarni, G . U.; Thomas, P. J.; Edwards, D. P. *Chem. Soc. Rev.* **2000**, *29*, 27.

(7)   Daniel, M.-C.; Astruc, D. *Chem. Rev.* **2004**, *104*, 293.

(8)   Burda, C.; Chen, X.; Narayanan, R.; El-Sayed, M. A. *Chem. Rev.* **2005**, *105*, 1025.

(9)   (a) Ipe, B. I.; Thomas, K. G.; Barazzouk, S.; Hotchandani, S.; Kamat, P. V. *J. Phys. Chem. B* **2002**, *106*, 18; (b) Ipe, B. I.; Thomas, K. G. *J. Phys. Chem. B* **2004**, *108*, 13265.

(10)   Sudeep, P. K.; Ipe, B. I.; Thomas, K. G.; George, M. V.; Barazzouk, S.; Hotchandani, S.; Kamat, P. V. *Nano Lett.* **2002**, *2*, 29.

(11)   (a) Ipe, B. I.; Mahima, S.; Thomas, K. G. *J. Am. Chem. Soc.* **2003**, *125*, 7174; (b) Ipe, B. I.; Yoosaf, K.; Thomas, K. G. *J. Am. Chem. Soc.* **2006**, *128*, 1907; (c) Yoosaf, K.; Ipe, B. I.; Suresh, C. H.; Thomas, K. G. *J. Phys. Chem. C* **2007**, *111*, 12839.

(12)   Baum, T.; Brust, M.; Bethell, D.; Schiffrin, D. J. *Langmuir* **1999**, *15*, 866.

(13)   Chen, S.; Ingram, R. S.; Hostetler, M. J.; Pietron, J. J.; Murray, R. W.; Schaaff, T. G.; Khoury, J. T.; Alvarez, M. M.; Whetten, R. L. *Science* **1998**, *280*, 2098.

(14)   Chen, S.; Murray, R. W. *J. Phys. Chem. B* **1999**, *103*, 9996.

(15)   Fishelson, N.; Shkrob, I.; Lev, O.; Gun, J.; Modestov, A. D. *Langmuir* **2001**, *17*, 403.

(16) (a) Rosi, N. L.; Mirkin, C. A. *Chem. Rev.* **2005**, *105*, 1547; (b) Elghanian, R.; Storhoff, J. J.; Mucic, R. C.; Letsinger, R. L.; Mirkin, C. A. *Science* **1997**, *277*, 1078; (c) Storhoff, J. J.; Elghanian, R.; Mucic, R. C.; Mirkin, C. A.; Letsinger, R. L. *J. Am. Chem. Soc.* **1998**, *120*, 1959; (d) Thaxton, C. S.; Georganopoulou, D. G.; Mirkin, C. A. *Clin. Chim. Acta* **2006**, *363*, 120; (e) Cheng, M. M. C.; Cuda, G.; Bunimovich, Y. L.; Gaspari, M.; Heath, J. R.; Hill, H. D.; Mirkin, C. A.; Nijdam, A. J.; Terracciano, R.; Thundat, T.; Ferrari, M. *Curr. Opin. Chem. Biol.* **2006**, *10*, 11; (f) Lee, J.-S.; Han, M. S.; Mirkin, C. A. *Angew. Chem. Int. Ed.* **2007**, *46*, 4093; (g) Xu, X.; Georganopoulou, D. G.; Hill, H. D.; Mirkin, C. A. *Anal. Chem.* **2007**, *79*, 6650. (h) Stoeva, S. I.; Lee, J.-S.; Thaxton, C. S.; Mirkin, C. A. *Angew. Chem. Int. Ed.* **2006**, *45*, 3303.

(17) Lahav, M.; Gabriel, T.; Shipway, A. N.; Willner, I. *J. Am. Chem. Soc.* **1999**, *121*, 258.

(18) Chen, S.; Ingram, R. S.; Hostetler, M. J.; Pietron, J. J.; Murray, R. W.; Schaaff, T. G.; Khoury, J. T.; Alvarez, M. M.; Whetten, R. L. *Science* **1998**, *280*, 2098.

(19) Hostetler, M. J.; Green, S. J.; Stokes, J. J.; Murray, R. W. *J. Am. Chem. Soc.* **1996**, *118*, 4212.

(20) Kamat, P. V.; Barazzouk, S.; Hotchandani, S. *Angew. Chem. Int. Ed.* **2002**, *41*, 2764.

(21) (a) Wang, G. L.; Zhang, J.; Murray, R. W. *Anal. Chem.* **2002**, *74*, 4320; (b) Clark, H. A.; Campagnola, P. J.; Wuksell, J. P.; Lewis, A.; Loew, L. M. *J. Am. Chem. Soc.* **2000**, *122*, 10234.

(22) Schmid, G.; Baunile, M.; Geerkens, M.; Heim, I.; Osemann, C.; Sawitonski, T. *Chem. Soc. Rev.* **1999**, 28.

(23) Ipe, B. I. *Ph.D Thesis, University of Kerala,* **2004**.

(24) Sudeep, P. K. *Ph.D Thesis, University of Kerala,* **2004**.

(25) Yoosaf, K. *Ph.D Thesis, CUSAT,* **2008**.

(26) Drexhage, K. H.; Kuhn, H.; Shafer, F. P. *Ber. Bunsenges. Phys. Chem.* **1968**, *72*, 329.

(27)   Stellacci, F.; Bauer, C. A.; Meyer-Friedrichsen, T.; Wenseleers, W.; Marder, S. R.; Perry, J. W. *J. Am. Chem. Soc.* **2003**, *125*, 328.

(28)   Fan, C. H.; Wang, S.; Hong, J. W.; Bazan, G. C.; Plaxco, K. W.; Heeger, A. J. *Proc. Natl. Acad. Sci. U.S.A.* **2003**, *100*, 6297.

(29)   Imahori, H.; Arimura, M.; Hanada, T.; Nishimura, Y.; Yamazaki, I.; Sakata, Y.; Fukuzumi, S. *J. Am. Chem. Soc.* **2001**, *123*, 335.

(30)   Chen, M. M. Y.; Katz, A. *Langmuir* **2002**, *18*, 2413.

(31)   Dulkeith, E.; Morteani, A. C.; Niedereichholz, T.; Klar, T. A.; Feldmann, J.; Levi, S. A.; van Veggel, F. C. J. M.; Reinhoudt, D. N.; Moller, M.; Gittins, D. I. *Phys. Rev. Lett.* **2002**, *89*, 203002.

(32)   Hirakawa, T.; Kamat, P. V. *J. Am. Chem. Soc.* **2005**, *127*, 3928.

(33)   Juris, A.; Balzani, V.; Barigelletti, F.; Campagna, S.; Belser, P.; von Zelewsky, A. *Coord. Chem. Rev.* **1988**, *84*, 85.

(34)   McCusker, J. K. *Acc. Chem. Res.* **2003**, *36*, 876.

(35)   Yonemoto, E. H.; Saupe, G. B.; Schmehl, R. H.; Hubig, S. M.; Riley, R. L.; Iverson, B. L.; Mallouk, T. E. *J. Am. Chem. Soc.* **1994**, *116*, 4786.

(36)   Borja, M.; Dutta, P. K. *Nature* **1993**, *362*, 43.

(37)   Hagfeldt, A.; Gratzel, M. *Acc. Chem. Res.* **2000**, *33*, 269.

(38)   Wang, Q.; Zakeeruddin, S. M.; Nakeeruddin, M. K.; Humphry-Baker, R.; Gratzel, M. *J. Am. Chem. Soc.* **2006**, *128*, 4446.

(39)   Miao, W.; Choi, J. P.; Bard, A. J. *J. Am. Chem. Soc.* **2002**, *124*, 14478.

(40)   Clarke, Y.; Xu, W.; Demas, J. N.; DeGraff, B. A. *Anal. Chem.* **2000**, *72*, 3468.

(41)   Johansson, O. *Ph.D Thesis, Stockholm University*, **2004**.

(42)   Imahori, H.; Norieda, H.; Yamada, H.; Nishimura, Y.; Yamazaki, I.; Sakata, Y.; Fukuzumi, S. *J. Am. Chem. Soc.* **2001**, *123*, 100.

(43)   Yamada, M.; Tadera, T.; Kubo, K.; Nishihara, H. *Langmuir* **2001**, *17*, 2363.

(44)   Makarova, O. V.; Ostafin, A. E.; Miyoshi, H.; Norris, J. R.; Meisel, D. *J. Phys. Chem. B* **1999**, *103*, 9080.

(45) Hu, J.; Zhang, J.; Liu, F.; Kittredge, K.; Whitesell, J. K.; Fox, M. A. *J. Am. Chem. Soc.* **2001**, *123*, 1470.

(46) Aguila, A.; Murray, R. W. *Langmuir* **2000**, *16*, 5949.

(47) Akiyama, T.; Inoue, K.; Kuwahara, Y.; Niidome, Y.; Terasaki, N.; Nitahara, S.; Yamada, S. *Langmuir* **2005**, *21*, 793.

(48) Terasaki, N.; Otsuka, K.; Akiyama, T.; Yamada, S. *Jap. J. Appl. Phys. Part-1* **2004**, *43*, 2372.

(49) Ito, M.; Tsukatani, T.; Fujihara, H. *J. Mater. Chem.* **2005**, *15*, 960.

(50) Dong, T. Y.; Shih, H. W.; Chang, L. S. *Langmuir* **2004**, *20*, 9340.

(51) Xu, X. H. N.; Huang, S.; Brownlow, W.; Salaita, K.; Jeffers, R. B. *J. Phys. Chem. B* **2004**, *108*, 15543.

(52) Glomm, W. R.; Moses, S. J.; Brennaman, M. K.; Papanikolas, J. M.; Franzen, S. *J. Phys. Chem. B* **2005**, *109*, 804.

(53) Huang, T.; Murray, R. W. *Langmuir* **2002**, *18*, 7077.

(54) Soller, T.; Ringler, M.; Wunderlich, M.; Klar, T. A.; Feldmann, J.; Josel, H.-P.; Markert, Y.; Nichtl, A.; Kurzinger, K. *Nano Lett.* **2007**, *7*, 1941.

(55) Salmon, L.; Verlhac, J.-B.; Bied-Charreton, C.; Verchè-Béaur, C.; Gaudemer, A.; Pasternack, R. F. *Tetrehedron Lett.* **1990**, *31*, 519.

(56) Hu, J.; Fox, M. A. *J. Org. Chem.* **1999**, *64*, 4959.

(57) Sullivan, B. P.; Salmon, D. J.; Meyer, T. J. *Inorg. Chem.* **1978**, *17*, 3334.

(58) Brust, M.; Walker, M.; Bethell, D.; Schffrin, D. J.; Whyman, R. *J. Chem. Soc., Chem. Commun.* **1994**, 801.

(59) Templeton, A. C.; Wuelfing, W. P.; Murray, R. W. *Acc. Chem. Res.* **2000**, *33*, 27.

(60) Song, Y.; Murray, R. W. *J. Am. Chem. Soc.* **2002**, *124*, 7096.

(61) Ionita, P.; Gilbert, B. C.; Chechik, V. *Angew. Chem. Intl. Ed.* **2005**, *44*, 3720.

(62) Zheng, M.; Li, Z. G.; Huang, X. Y. *Langmuir* **2004**, *20*, 4226.

(63) (a) Terill, R. H.; Postlethwaite, T. A.; Chen, C.-H.; Poon, C. D.; Terzis, A.; Chen, A.; Hutchison, J. E.; Clark, M. R.; Wignall, G.; Londono, J. D.;

Superfine, R.; Falvo, M.; Johnson, C. S. Jr.; Samulski, E. T.; Murray, R. W. *J. Am. Chem. Soc.* **1995**, *117*, 12537; (b) which assigns the gold core as a sphere with density of 58.01 atoms/nm^3 covered with a skin of hexagonally close packed gold atoms with number density of surface gold atoms as 13.89 atoms/nm.

(64)   Goze, C.; Chambron, J.-C.; Heitz, V.; Pomeranc, D.; Salom-Roig, X. J.; Sauvage, J.-P.; Morales, A. F.; Barigelletti, F. *Eur. J. Inorg. Chem.* **2003**, 3752.

(65)   Navon, G.; Sutin, N. *Inorg. Chem.* **1974**, *13*, 2159.

(66)   Mulazzani, Q. G.; Emmi, S.; Fuochi, P. G.; Hoffman, M. Z.; Venturi, M. *J. Am. Chem. Soc.* **1978**, *100*, 981.

(67)   Lomoth, R.; Häupl, T.; Johansson, O.; Hammarström, L. *Chem.-- Eur. J.* **2002**, *8*, 102.

(68)   Templeton, A. C.; Pietron, J. J.; Murray, R. W.; Mulvaney, P. *J. Phys. Chem. B* **2000**, *104*, 564.

CHAPTER 3

Gold Nanoparticle Decorated Carbon Nanotubes for Light Induced Electron Transfer

3.1. Abstract

Photoactive hybrid nanomaterials were synthesized by functionalizing ruthenium trisbipyridine ($Ru(bpy)_3^{2+}$) chromophores on to single walled carbon nanotubes (**SWNT**), both in the presence and absence of gold nanoparticles. Various light induced processes in these hybrid systems were investigated using steady state and time resolved techniques. A unidirectional electron flow was observed from the excited state of $Ru(bpy)_3^{2+}$ to carbon nanotubes when the chromophores were linked through Au nanoparticles (**SWNT-Au-Ru^{2+}**). In contrast, photoinduced electron transfer was not observed from *$Ru(bpy)_3^{2+}$ to **SWNT** when these components were linked directly. Based on luminescence lifetime studies, the forward electron transfer rate constant (k_{ET}) in **SWNT-Au-Ru^{2+}** nanohybrids was estimated as 2.55×10^8 s^{-1} and the electron transfer products ($Ru(bpy)_3^{3+}$ and the monoanion of **SWNT**) were further characterized by transient absorption studies. The charge equilibration occurring at the **SWNT-Au** heterojunctions, due to the differences in electrochemical potentials, result in the formation of a localized depletion layer at the **SWNT** walls which may act as acceptor sites of electrons from

*Ru(bpy)$_3^{2+}$. The charge separation in **SWNT-Au-Ru^{2+}** nanohybrids sustained for several nanoseconds before undergoing recombination (k_{BET} = 2.5 x 10^6 s^{-1}) making these systems promising for optoelectronic and artificial photosynthetic device applications.

3.2. Introduction

Photosynthetic light harvesting assembly is one of the finest pieces of molecular machinery that nature has ever created and life on earth derives all its energy from natural photosynthesis. It utilizes photoinduced energy transfer for harvesting sunlight which is followed by well-organized sequence of electron transfer reactions in the photosynthetic reaction center (RC).[1-3] The unique arrangement of molecules in RC is responsible for the unidirectional electron transfer, which prevents the back electron transfer by increasing the distance of separation of the radical ion pairs (Scheme 3.1).[1-3]
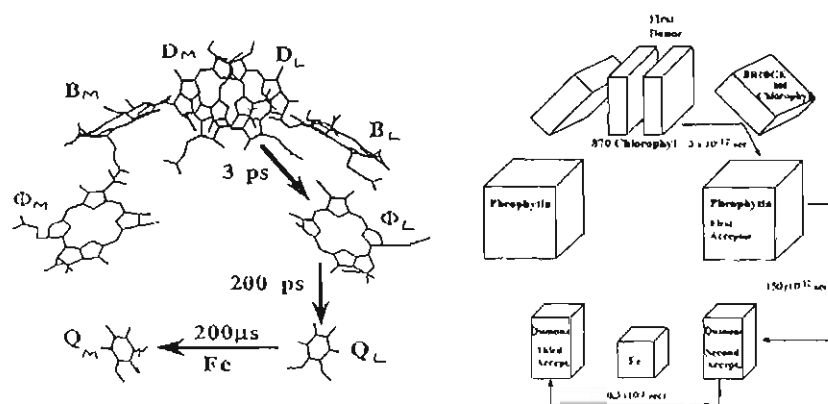
Scheme 3.1. Structure of the cofactors of the reaction centre from *Rhodobacter sphaeroides (adapted from reference 3).*

Photosynthetic system is complex in nature and attempts have been actively pursued, in recent years, in the design of molecular as well as nanohybrid systems[4] which can serve as components of photovoltaic devices that mimic parts of the photosynthetic machinery. A long-term goal in this area is to construct biomimetic supramolecular systems with electron donors (D) and acceptors (A) for carrying out the functions of natural photosynthesis. Among the various steps, generation of long-lived charge-separated ion pairs (D^+/A^-) is the most crucial one. A practical approach is to use these stable ion pairs for (i) designing photovoltaic systems which can generate photocurrent or (ii) producing high energy substances (e.g., hydrogen from water as in Scheme 3.2).
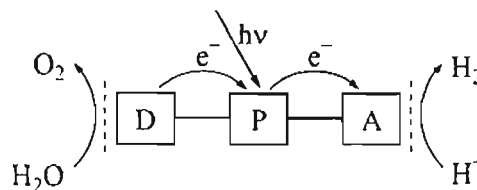
Scheme 3.2. Electron transfer processes in an artificial system that consists of a photosensitizer (P), electron acceptors (A) and donors (D).

Of late, it was demonstrated that carbon based systems such as fullerenes and carbon nanotubes are excellent acceptors of electrons.[5,6] Understanding the basic properties of carbon nanotube[7,8] based one dimensional systems has opened up newer possibilities for the design of nanoscale electronic devices,[9-27] energy conversion systems[28-44] and biological sensors.[45-49] For example, the intriguing electron accepting and transporting properties of single walled carbon nanotubes have been

exploited for the design of nanohybrid systems for light energy conversion.[28 44] The use of **SWNT** based nanohybrids for charge separation has been demonstrated by functionalizing them with appropriate donor groups,[29-36] as well as attaching semiconductor nanoparticles to their surface.[37-44,50,51] An alternative approach is to use metal-semiconductor hybrid materials such as noble metal nanoparticle decorated **SWNT**[24] for photovoltaic applications. The rationale behind this design strategy is based on the fact that the band structure at the metal nanoparticle-**SWNT** interface is distinctly different from that of individual components.[24]

Metal and semiconductor possess different electrochemical potentials, hence charge redistribution occurs at the contact junction so that the potentials are equilibrated (generally represented as band bending).[52] When metals are doped on n-type semiconductor, charge transfer occurs to the metal resulting in the depletion of electrons at the semiconductor interface (Schottky type potential barrier[52]; Scheme 3.3).

Before contact   After Contact
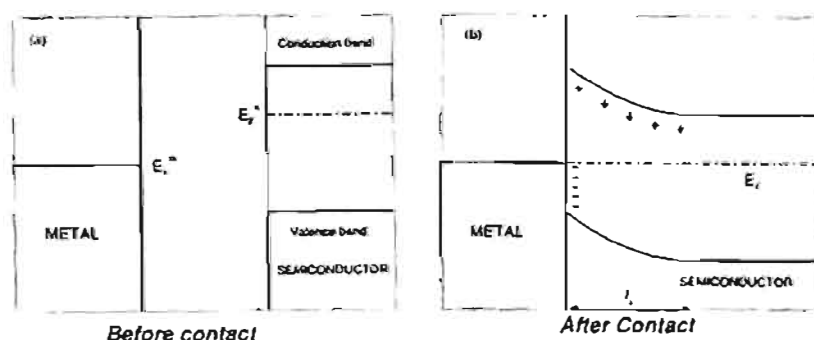
Scheme 3.3. Scheme of the metal–semiconductor band structure (a) before contact and (b) after equilibrium. E^m_F and E^s_F are the Fermi levels for the metal and semiconductor. l_s is the depletion length (*adapted from reference 52*).

In the case of bulk metal-semiconductor junction, the well-known Schottky model yields,[52]

$$\rho = (\varepsilon_s N_d \Delta E/2\pi)^{1/2} \qquad (3.1)$$

$$l_s = (\varepsilon_s \Delta E/2\pi e^2 N_d)^{1/2} \qquad (3.2)$$

where 'ρ' is the surface density of charge passed on the metal, 'l_s' the depletion length in the semiconductor, 'N_d' the concentration of charge donors in the semiconductor, 'ε_s' the semiconductor dielectric constant, 'ΔE' the difference of the Fermi energies in the semiconductor and metal before the charge redistribution, and 'e' the electron charge. The derivation of Equations 3.1 and 3.2 is based on the assumption that the potential in the semiconductor is dependent only on the coordinate along the normal to the interface. Mathematically, it is clear that this assumption holds if the depletion length defined by Equation 3.2 is smaller than the size of a supported particle. Thus, for nanoparticles it is difficult to apply traditional Schottky junction behavior and a fully accepted theoretical model for metal nanoparticle-semiconductor junction is not yet developed. One of the theoretical models propose that the metal nanoparticles may create an interfacial "Schottky-type" potential barriers on semiconducting substrates.[53] Experimental studies have later shown that the Au nanoparticles form size-dependent "nano-Schottky" potential barriers on semiconducting substrates that asymptotically approach the macroscopic Schottky barrier.[24] Hence the semiconductor supported metal nanoparticle will experience this effect and create localized depletion regions on the semiconductor wall which acts as the deep acceptor states (Scheme 3.4).[52]
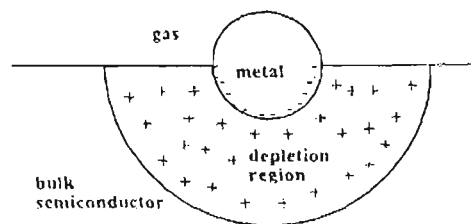
Scheme 3.4. Physical model illustrating the contact of metal crystallite and semiconducting support. Plus signs and dashed lines indicate positive and negative charges, respectively (*adapted from reference 52*).

Other theoretical and experimental investigations dealing with the modified electronic properties of metal nanoparticle-semiconductor interface include metal nanoparticle-TiO_2,[52] Ag nanoparticle-SbO_2,[53] Mn nanoparticle-GaN nanowires[54] and noble metal nanoparticle-**SWNT**[24] systems. Methodologies for incorporating Ag, Au and Pt nanoparticles on to the surface of **SWNT**[50-59] and their potential applications as sensors and field emission transistors[23-27] have also been demonstrated. For example, fabrication of sensor arrays for the identification and detection of toxic/combustable gases (H_2, CH_4, CO and H_2S) has been demonstrated by Star and coworkers using a carbon nanotube field emission transistor (NTFET) consisting of metal decorated carbon nanotubes (Figure 3.1).[26]

It has been recently reported that the electron donation to the nanoparticle decorated **SWNT** network of NTFET, upon exposure to NO gas, is dependant on the work function of the metal.[24] Based on these studies, it is concluded that the Schottky type potential barrier existing at the nanoparticle-**SWNT** interface is intimately related to the work function of the metal (Figure 3.2).
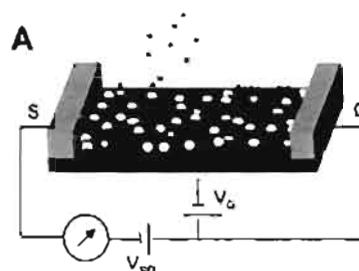
Figure 3.1. (A) Conceptual illustration of a carbon nanotube network connecting source (S) and drain (D) electrodes of a FET. **SWNTs** are decorated with metal nanoparticles (silver bullets) for selective detection of analyte gases (red dots) (*adapted from reference 26*).
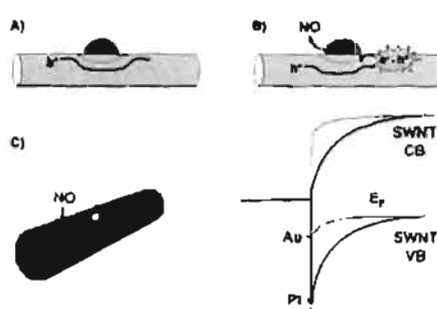
Figure 3.2. Chemically induced potential barriers at the carbon nanotube-metal nanoparticle interface (*adapted from reference 24*).

While **SWNT**-metal nanoparticle systems are proposed for sensing applications, the possibility of utilizing these materials as components of light energy conversion systems has not been actively pursued. Herein, we investigate various light induced processes between ruthenium trisbipyridine[60-75] and **SWNT**, both in the presence and absence of gold nanoparticles. The structures of the hybrid systems under investigation are illustrated in Chart 3.1.
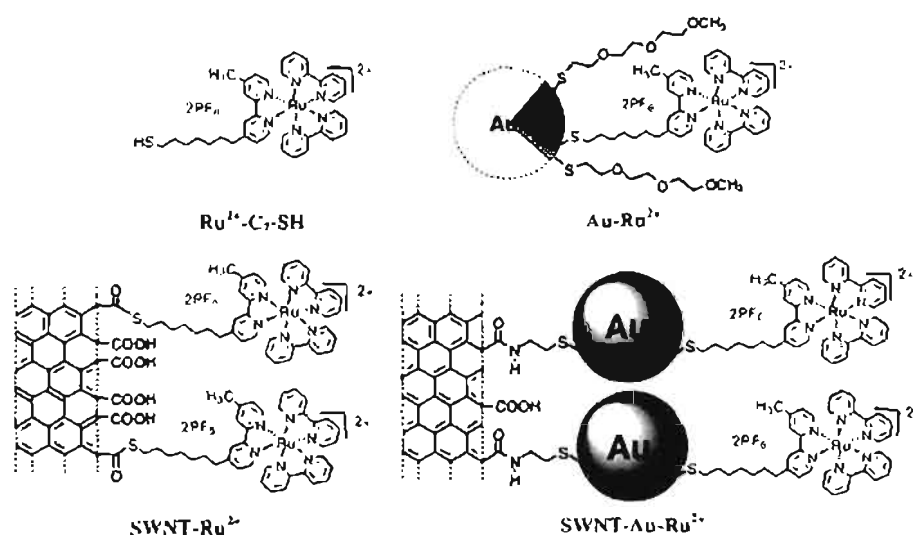
Chart 3.1. Structures of hybrid systems under study.

3.3. Results and Discussion

3.3.1. Synthesis and Characterization

Ruthenium trisbipyridine bearing a thiol group (**Ru^{2+}-C$_7$-SH**) was synthesized as described in Chapter 2 and were functionalized on to the surface of Au nanoparticles by adopting a place exchange reaction (**Au-Ru^{2+}**; average diameter of 4.5 nm).[74] **SWNTs** (HiPCO) were purified first by heating in air at 350°C to remove the carbonaceous material and subsequently heated with conc. HNO$_3$ for 4 h to remove the transition metal impurities.[76-80] The purified **SWNTs** were converted to thiolated **SWNTs** (**SWNT-SH**) by using the modified literature procedures (Scheme 3.5).[76-80] Accordingly, the purified **SWNTs** were converted to carboxylated **SWNTs** (**SWNT-CO$_2$H**) and further to corresponding acid chloride

(SWNT–COCl) and subsequently to **SWNT-SH** by reacting with 2-mercaptoethylamine hydrochloride. **Ru(bpy)$_3^{2+}$** were functionalized on **SWNT** in the absence and presence of Au nanoparticles (**SWNT-Ru^{2+}** and **SWNT-Au-Ru^{2+}**, respectively) by the pathways shown in Scheme 3.5 and the details of the synthetic procedure adopted are provided in the Experimental Section. In both cases, we have varied the concentration of **Ru(bpy)$_3^{2+}$** on the surface of **SWNT** (*vide infra*). The different stages of the functionalization of **SWNTs** were monitored by analytical (Thermogravimetric Analysis, TGA), microscopic (Transmission Electron Microscope, TEM) and spectroscopic (Raman, FTIR, UV-visible) techniques.
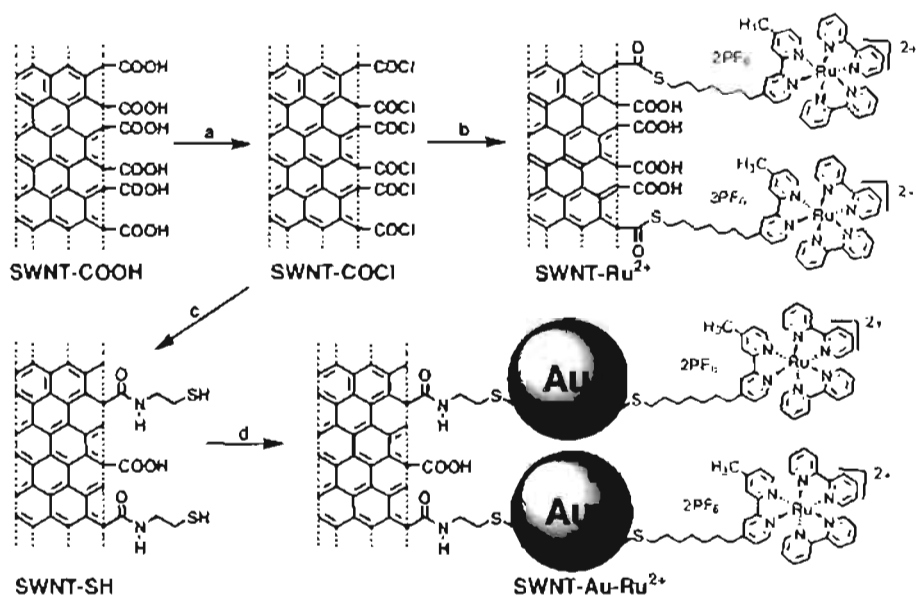
Scheme 3.5. (a) SOCl$_2$, DMF; (b) **Ru-C$_7$-SH**, THF, 70°C, 36 h; (c) 2-mercapto-ethylamine hydrochloride, pyridine, DMF. 70°C. 24 h; (d) **Au-Ru^{2+}**, THF, rt. 36 h.

3.3.2. HRTEM Studies

The HRTEM samples were prepared by drop-casting a dilute suspension on to a carbon coated copper grid. The presence of **SWNTs** was confirmed by TEM analysis and representative images of **SWNT-Ru^{2+}** and **SWNT-Au-Ru^{2+}** are presented in Figure 3.3. The presence of Au nanoparticles bound on **SWNTs** is clearly visible in TEM images as dark spheres, with an average diameter of 4.5 nm (Figure 3.3B,C). Functionalized **SWNTs** are observed as relatively thin bundles and hence the Au nanoparticles may be intimately attached on to nanotube surface.
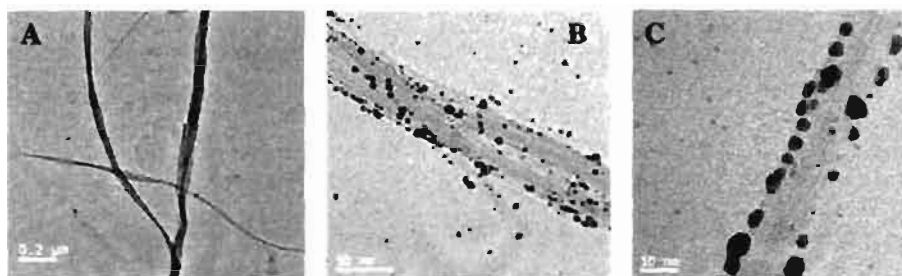
Figure 3.3. HRTEM images of functionalized **SWNTs** in relatively thin bundles: (A) **SWNT- Ru^{2+}** and (B&C) **SWNT-Au-Ru^{2+}**. Samples were prepared by drop casting a dilute suspension on to a carbon coated copper grid.

3.3.3. Raman Studies

Raman spectroscopy is a valuable tool used for characterizing nanotubes since it provides detailed information on the structure and properties.[9,10] Figure 3.4 shows the normalized Raman spectra (excitation wavelength of 514 nm) of the pristine **SWNTs** and functionalized nanotubes (**SWNT-COOH, SWNT-Ru^{2+}** and **SWNT-Au-Ru^{2+}**) measured at room temperature under air. The main characteristic bands for single walled carbon nanotubes, namely RBM, D, G and G' bands were observed in the

Raman spectra, in all cases. The radial breathing mode (RBM), characteristic of tubular structure, was preserved during various stages of functionalization. Moreover, it is interesting to note that the D-band does not undergo any intensity variation upon functionalizing the chromophores and metal nanoparticles on the surface of carbon nanotubes. This clearly rules out the possibility of any disintegration of carbon nanotubes. All these results confirm that the integrity and tubular nature of single walled carbon nanotubes were well preserved at different stages of functionalization.
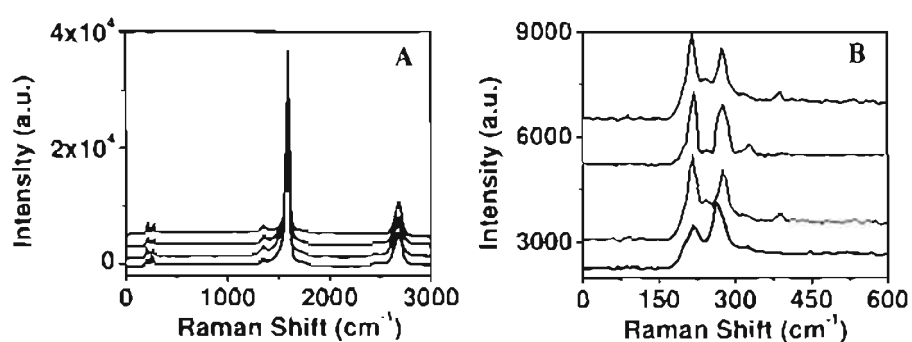
Figure 3.4. (A) Normalized Raman spectra of pristine (black), SWNT-COOH (red), SWNT-Ru^{2+} (blue) and SWNT-Au-Ru^{2+} (green) at room temperature under air (excitation wavelength of 514 nm). (B) RBM region at different stages of functionalization (G band of all the spectra were normalized).

3.3.4. FTIR Studies

The covalent functionalization of Ru(bpy)$_3^{2+}$ on the surface of SWNTs was confirmed using FTIR by the presence of amide bands and carbonyl stretching of thioester. FTIR spectra of SWNT-CO$_2$H, SWNT-Ru^{2+} and SWNT-Au-Ru^{2+} are provided in Figure 3.5. The FTIR spectrum showed characteristic peaks for SWNT-CO$_2$H (1733 cm^{-1}, CO stretching), SWNT-Ru^{2+} (1682 cm^{-1}, thioester) and SWNT-CONH(CH$_2$)$_2$SH (amide I

band at 1686 cm^{-1} and amide II band at 1535 cm^{-1}), confirming the covalent functionalization.
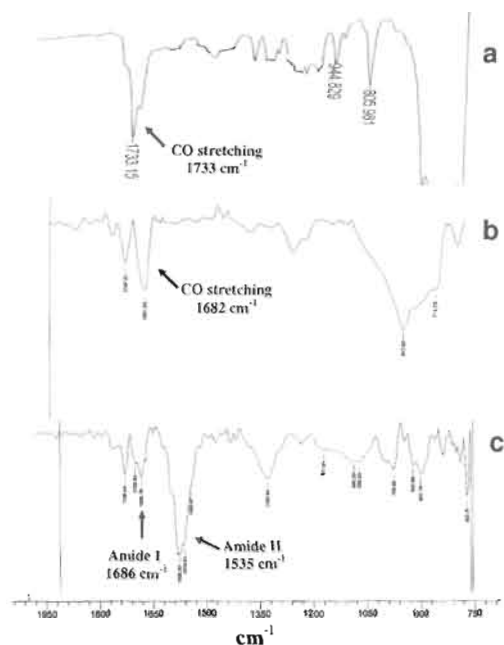
Figure 3.5. FTIR spectra of (a) **SWNT-COOH**, (b) **SWNT-Ru^{2+}** and (c) **SWNT-Au-Ru^{2+}**.

3.3.5. Thermogravimetric Analysis

Thermograms at both low and high loading of chromophores on functionalized SWNTs showed similarities with that of **Ru^{2+}-C$_7$-SH** (Figure 3.6). Thermogravimetric analysis (TGA) of compounds at low and high loadings of chromophores presents a loss of weight of ~20% and ~40% for **SWNT-Ru^{2+}** and ~25% and ~50% for **SWNT-Au-Ru^{2+}** at 600°C. In the former case, the samples which provided lower and higher loss of weight

were designated as **SWNT-Ru$_L$$^{2+}$** and **SWNT-Ru^{2+}** and latter case as **SWNT-Au-Ru$_L$$^{2+}$** and **SWNT-Au-Ru^{2+}**.
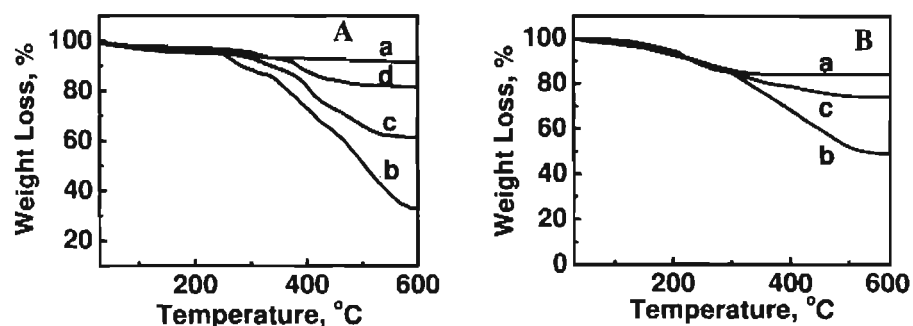
Figure 3.6. TGA of functionalized **SWNTs**. (A) (a) purified **SWNT**, (b) **Ru^{2+}-C$_T$-SH**, (c) **SWNT-Ru^{2+}** and (d) **SWNT-Ru$_L$$^{2+}$** and (B) (a) Au nanoparticles, (b) **SWNT-Au-Ru^{2+}** and (c) **SWNT-Au-Ru$_L$$^{2+}$** (loss of weight at 180-250°C for B corresponds to decomposition of ethylene glycol residue).

3.3.6. Photophysical Investigations on SWNT-Ru^{2+}

Steady State Absorption and Emission Studies: The UV-vis-NIR absorption spectra of **SWNT-Ru^{2+}** is presented in Figure 3.7A. The bands corresponding to **Ru(bpy)$_3$$^{2+}$** are distinct and remained more or less unperturbed when bound on **SWNT**, indicating the absence of any ground state interaction. For example, the absorption spectra of **Ru^{2+}-C$_T$-SH** in acetonitrile possess two bands; a band centered around 288 nm corresponding to π–π^* transition of bipyridine ligand and other at 453 nm originating from the metal-to-ligand charge transfer (MLCT). Both these bands remain unperturbed when **Ru(bpy)$_3$$^{2+}$** is functionalized on the surface of **SWNT**. The luminescence of **Ru^{2+}-C$_T$-SH** is centered at 612 nm with a quantum yield of 0.07.[74] On covalent functionalization of **Ru-C$_T$-SH** to **SWNT**, the emission of the **Ru(bpy)$_3$$^{2+}$** chromophore is drastically

quenched suggesting a strong excited state interaction (Figure 3.7B). However, the spectral overlap between the absorption of **SWNT** and the MLCT band of **Ru(bpy)$_3$$^{2+}$** prevented the selective excitation of the chromophore and hence quantification of the emission yields by steady-state technique is difficult. The excited state interactions were further elucidated by following luminescent lifetime studies.
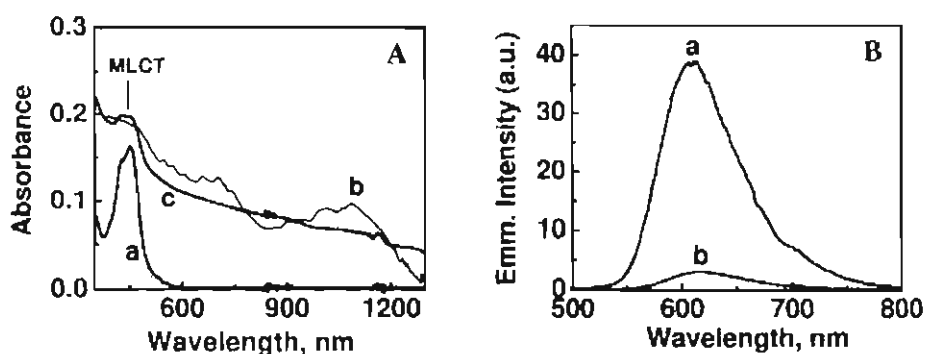
Figure 3.7. Absorption and luminescence properties of unbound and bound Ru(bpy)$_3$$^{2+}$ on **SWNT** in degassed CH$_3$CN: (A) absorption spectra of (a) **Ru^{2+}-C$_7$-SH**, (b) purified **SWNT** and (c) **SWNT-Ru^{2+}** and (B) the corresponding luminescence spectra of (a) **Ru^{2+}-C$_7$-SH** and (b) **SWNT-Ru^{2+}** (excitation wavelength 453 nm).

Time-Resolved Luminescence Studies: Unbound **Ru^{2+}-C$_7$-SH** in various solvents follows monoexponential decay, with a lifetime (τ) of 1.11 µs in CH$_2$Cl$_2$ and 961 ns in CH$_3$CN, which is attributed to the inherent lifetime of the chromophore (trace 'a' in Figure 3.8). Interestingly, **Ru(bpy)$_3$$^{2+}$** functionalized on **SWNT** follows a biexponential decay in CH$_3$CN (ε = 39.8), with a long lived (τ_1 = 960 ns; χ_1 = 20%) and a short lived (τ_2 = 4.5 ns; χ_2 = 80%) components (trace 'b' in Figure 3.8). The lifetime of the long-lived component is similar to that of unbound **Ru^{2+}-C$_7$-SH** and can be

attributed to the unquenched $Ru(bpy)_3^{2+}$ chromophore bound on **SWNT**. The short-lived component is attributed to the quenched excited state of $Ru(bpy)_3^{2+}$. By analyzing the relative abundance of both these species, it is clear that the emission of $Ru(bpy)_3^{2+}$ is quenched by 80% when functionalized on to the surface of **SWNT**.
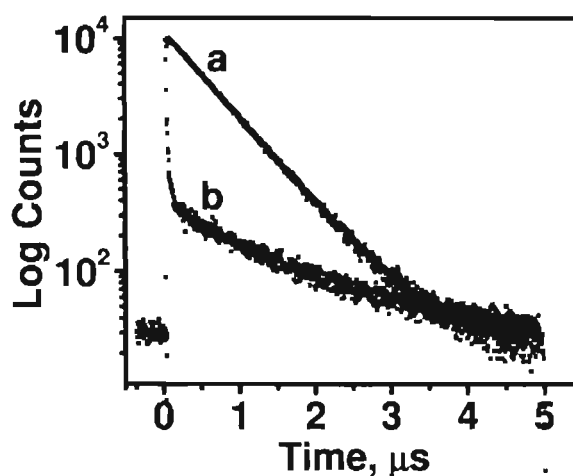
Figure 3.8. Luminescence lifetime profile of (a) $Ru^{2+}-C_T-SH$ and (b) $SWNT-Ru^{2+}$ at higher loadings of $Ru(bpy)_3^{2+}$ in degassed CH_3CN (excitation wavelength 440 nm).

Nanosecond Transient Absorption Studies: The triplet-triplet (T-T) absorption of $Ru^{2+}-C_T-SH$ has a characteristic band at 370 nm which decays with a rate constant of $k_T = 1.10 \times 10^6 \ s^{-1}$ ($\tau = 909$ ns) in acetonitrile (trace 'a' in Figure 3.9A and Figure 3.9B).[74] The corresponding bleach observed at 450 and 620 nm in the difference absorption spectra (laser excitation at 355 nm) is attributed to the loss of ground state absorption and emission, respectively. Transient absorption studies of $SWNT-Ru^{2+}$ was carried out both in argon degassed and oxygen saturated acetonitrile

solutions under two different conditions having lower and higher loadings of chromophores. The spectral features of **SWNT-Ru²⁺** at lower loading of chromophores are similar to those of **Ru²⁺-C₇-SH** which were totally quenched upon oxygen saturation indicating the absence of any excited state interactions. The band at 370 nm is assigned as the triplet excited state of the chromophore. In contrast, two additional peaks at 310 nm and 500 nm were observed at high loadings of chromophores on **SWNT** along with the 370 nm band (trace 'b' in Figure 3.9A). Upon bubbling with oxygen, the 370 nm band was quenched leaving a residual absorption at 350 nm (trace 'c' in Figure 3.9A). Complementary chemical and electrochemical methods[82-84] have been earlier adopted for the characterization of the redox products of **Ru(bpy)₃²⁺**: reduction to **Ru(bpy)₃¹⁺** results in absorption peaks at 350 and 500 nm[82,83] and a strong absorption at 310 nm[82,84] upon oxidation to **Ru(bpy)₃³⁺**. Comparing these results with the transient absorption spectra presented in Figure 3.9A, it is clear that the peaks originate through an excited state redox reaction resulting in the formation of **Ru(bpy)₃¹⁺** and **Ru(bpy)₃³⁺**. We have further probed on the fate of these transient species by monitoring the absorption-time profile at 500 and 310 nm (Figure 3.9C). Both the transients follow monoexponential decay with a rate constant of 6.9×10^6 s⁻¹ ($\tau = 145$ ns) in argon degassed solution, suggesting that these species originate from the same redox process. Blank experiments carried out using a saturated solution of **Ru²⁺-C₇-SH** do not produce any redox products on photoexcitation.
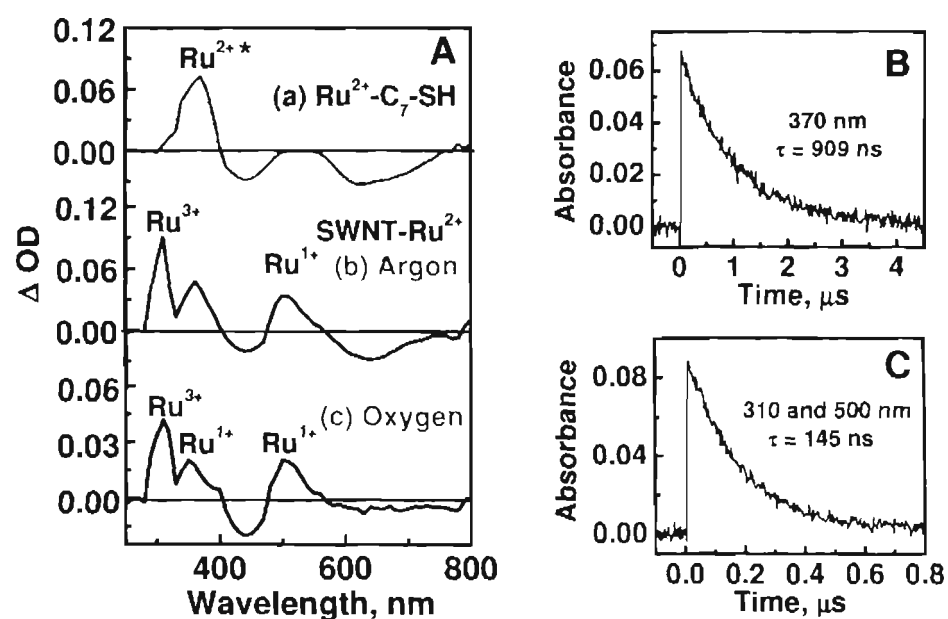
Figure 3.9. (A) Nanosecond transient absorption spectrum (355 nm laser pulse) of unbound and bound $Ru(bpy)_3^{2+}$ on **SWNT** in degassed CH_3CN recorded immediately after the pulse: (a) Ar saturated solution of Ru^{2+}-C_7-SH; (b) **SWNT-**Ru^{2+} having high loading of $Ru(bpy)_3^{2+}$ in Ar saturated and (c) oxygen saturated solutions; (B) Transient decay at 370 nm and (C) 310/500 nm in Ar degassed solution.

3.3.7. Photophysical Investigations on SWNT-Ru$_L^{2+}$

Experiments were further carried out on **SWNT-Ru^{2+}$_L$** where the concentration of **Ru-C$_7$-SH** is low on the surface of **SWNT**. Figure 3.10A represents the UV-vis-NIR spectrum of **SWNT-Ru^{2+}** at lower and higher loadings of $Ru(bpy)_3^{2+}$ on **SWNT**. The luminescence of $Ru(bpy)_3^{2+}$ when bound on **SWNT** at lower loadings (**SWNT-Ru^{2+}$_L$**) were slightly quenched (compared to **Ru^{2+}-C$_7$-SH**) which may be attributed to the loss of photons due to the absorption by **SWNT** (Figure 3.10B). Both luminescence and nanosecond transient absorption studies of **SWNT-Ru$_L^{2+}$** showed similar

spectral behavior as that of **Ru²⁺-C₇-SH**. From these results it is concluded that no electron transfer products were observed on decreasing the concentration of **Ru(bpy)₃²⁺** on **SWNT** (Figure 3.10C and 3.10D).
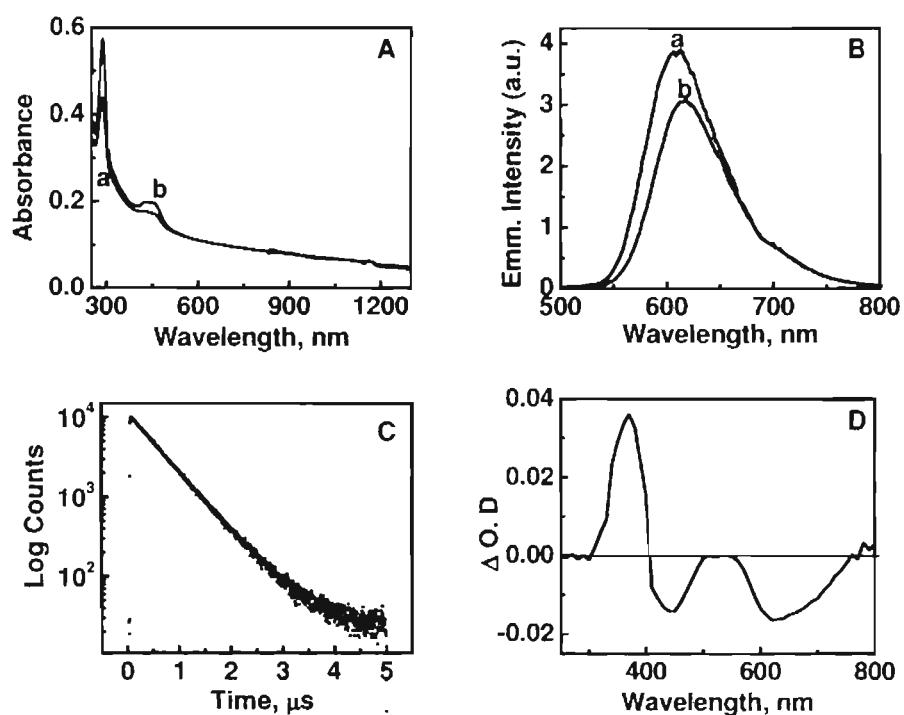
Figure 3.10. (A) absorption spectra of (a) **SWNT-Ru²⁺**ₗ and (b) **SWNT-Ru²⁺**, (B) luminescence spectra of (a) **Ru²⁺-C₇-SH** and (b) **SWNT-Ru²⁺**ₗ, (C) luminescence lifetime and (D) nanosecond transient absorption spectrum spectra of **SWNT-Ru²⁺**ₗ in degassed CH₃CN.

3.3.8. Photophysical Investigations on SWNT-Au-Ru²⁺

Steady State Absorption and Emission Studies: The UV-vis-NIR absorption spectra of **Ru²⁺-C₇-SH**, **Au-Ru²⁺**, purified **SWNT** and **SWNT-Au-Ru²⁺** are presented in Figure 3.11A. The bands corresponding to **Ru(bpy)₃²⁺** are distinct and remained more or less unperturbed when

bound on **SWNT**, indicating the absence of any ground state interaction. The additional band observed around 530 nm in the case of **SWNT-Au-Ru^{2+}** corresponds to the plasmon absorption of Au nanoparticles. Compared to **Au-Ru^{2+}**, the corresponding plasmon absorption band of **SWNT-Au-Ru^{2+}** was shifted by ~10 nm to red region due to the strong interaction with **SWNT** surface (Figure 3.11A). On covalent functionalization of **Au-Ru^{2+}** to **SWNT**, the emission of the **Ru(bpy)$_3$$^{2+}$** chromophore is drastically quenched suggesting a strong excited state interaction (Figure 3.11B). However, the spectral overlap between the MLCT band of **Ru(bpy)$_3$$^{2+}$** with the absorption of **SWNT** and Au nanoparticles prevented the selective excitation of the chromophore and hence quantification of the emission yields by steady-state technique is difficult. The excited state interactions were further elucidated by following luminescent lifetime studies.
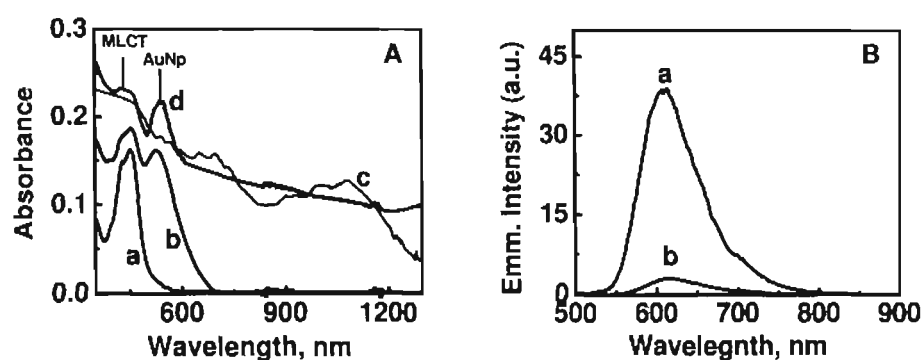
Figure 3.11. Absorption and luminescence properties of unbound and bound **Au-Ru^{2+}** on **SWNT** in degassed CH$_3$CN: (A) absorption spectra of (a) **Ru^{2+}-C$_7$-SH**, (b) **Au-Ru^{2+}** (c) purified **SWNT** and (d) **SWNT-Au-Ru^{2+}** and (B) the corresponding luminescence spectra of (a) **Ru^{2+}-C$_7$-SH** and (b) **SWNT-Au-Ru^{2+}** (excitation wavelength 453 nm).

Time-Resolved Luminescence Studies: Luminescence lifetime studies of both Ru^{2+}-C_7-SH and SWNT-Ru^{2+} with lower loading of chromophores follow a monoexponential decay with an average lifetime (τ) of 960 ± 2 ns in acetonitrile (trace 'a' in Figure 3.12). In contrast, a biexponential decay was observed in the case of SWNT-Au-Ru^{2+}, both at lower and higher loadings of chromophores (τ_1 = 960 ns; χ_1 = 20% and τ_2 = 3.9 ns; χ_2 = 80%) (trace 'b' in Figure 3.12). The lifetime of the long-lived component is similar to that of Ru^{2+}-C_7-SH which can be attributed to the unquenched $Ru(bpy)_3^{2+}$ bound on SWNT. The short lived species arises as a result of excited state quenching of $Ru(bpy)_3^{2+}$ and nanosecond transient absorption studies of SWNT-Au-Ru^{2+} were further carried out to elucidate the mechanistic pathways involved.
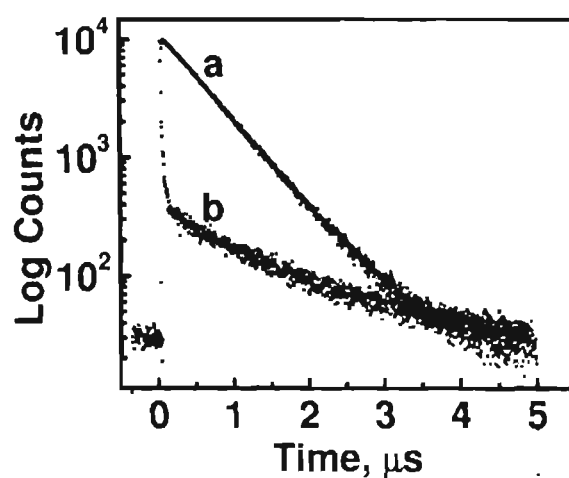
Figure 3.12. Luminescence lifetime profile of (a) Ru^{2+}-C_7-SH and (b) SWNT-Au-Ru^{2+} at higher loadings of $Ru(bpy)_3^{2+}$ in degassed CH_3CN (excitation wavelength 440 nm).

Nanosecond Transient Absorption Studies: Time-resolved transient absorption studies of **SWNT-Au-Ru^{2+}** was carried out, both in argon and oxygen saturated solutions, at lower and higher loadings of chromophores (Figure 3.13). Interestingly, the transient absorption spectral profile of **SWNT-Au-Ru^{2+}** were quite different when compared to those of **SWNT-Ru^{2+}** and remained unaffected by varying the concentration of chromophores. In argon saturated solutions, both at lower and higher loadings of **Ru(bpy)$_3$$^{2+}$** yielded two transients: a sharp one at 310 nm and a broad band at 530 nm, apart from the triplet-triplet absorption at 370 nm (trace 'a' in Figure 3.13A).

Figure 3.13. (A) Nanosecond transient absorption spectrum (355 nm laser pulse) **SWNT-Au-Ru^{2+}** in degassed CH$_3$CN recorded immediately after pulse: (a) **SWNT-Au-Ru^{2+}** having high loading of **Ru(bpy)$_3$$^{2+}$** in Ar saturated; (b) oxygen saturated solution and (c) low loading of **Ru(bpy)$_3$$^{2+}$** in Ar saturated solution; (B)Transient decay at 310 nm and (C) 530 nm in Ar saturated solution.

Compared to the transient absorption of the oxidized product ($Ru(bpy)_3^{3+}$) at 310 nm,[74,82,84] the bands at 370 and 530 nm got totally quenched upon bubbling with oxygen (trace 'b' in Figure 3.13A). The absorption-time profile were monitored at 310 nm and 530 nm in argon saturated solution and found to exhibit monoexponential decay with a rate constant of 2.5×10^6 s^{-1}, suggesting that these species originate through the same process (Figure 3.13B and 3.13C). In a recen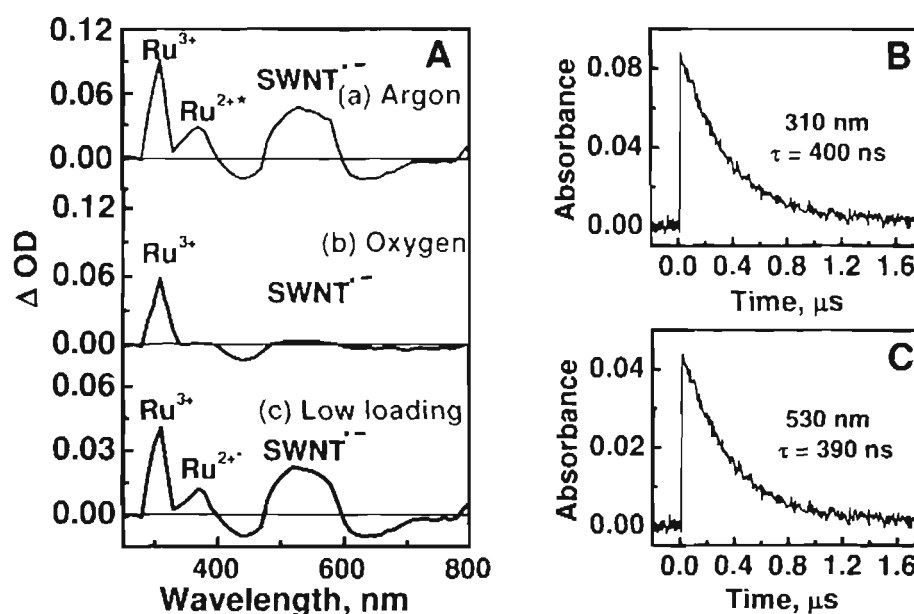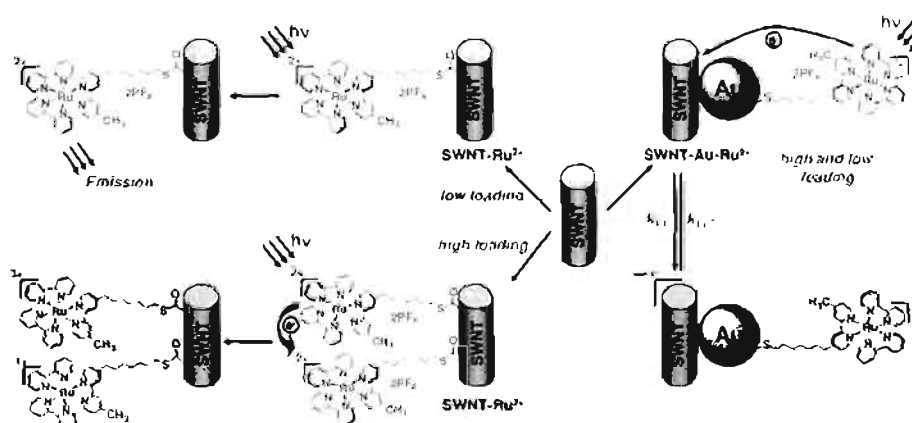t study, Guldi, Prato and coworkers have characterized the reduced form of **SWNT** (HiPCO) by spectroelectrochemical and pulse radiolytic studies[33] and found that the monoanion (**SWNT**$^-$) possesses a broad absorption band at 530 nm. The transient corresponding to **SWNT**$^-$ was also observed on photoexcitation of **SWNT** based dyads having ferrocene[33] and pyrene[36] as donors. Based on these results, it is clear that an efficient light induced electron transfer process occurs from the *$Ru(bpy)_3^{2+}$ to gold nanoparticle decorated **SWNT** resulting in the formation of **SWNT** monoanion and $Ru(bpy)_3^{3+}$.

3.3.9. Light Induced Processes in SWNT-Ru^{2+} and SWNT-Au-Ru^{2+}

Based on luminescence lifetime and transient absorption studies it is clear that when the concentration of the chromophore is high on the surface of **SWNT**, an interchromophoric quenching was observed through an electron transfer from *$Ru(bpy)_3^{2+}$ to a ground state molecule due to its close proximity (Scheme 3.6). Similar light induced redox reaction between $Ru(bpy)_3^{2+}$ chromophores were reported when they were closely packed on Au nanoparticle surface (**Au-Ru^{2+}**) in Chapter 2.[74] In contrast, such an

interaction is not observed on lowering the concentration of chromophores on SWNT. Interestingly, light induced processes was observed from $Ru(bpy)_3^{2+}$ to **SWNT** in **SWNT-Au-Ru^{2+}** nanohybrids, at both lower and higher loadings of chromophores, and results are summarized in Scheme 3.6. From the luminescence lifetime studies, the rate constant for forward electron transfer (k_{ET}) in **SWNT-Au-Ru^{2+}** was estimated as 2.55 x 10^8 s^{-1}. One of the promising features of **SWNT-Au-Ru^{2+}** is their relatively slower back electron transfer rate constant (k_{BET} = 2.5 x 10^6 s^{-1}) which was estimated based on transient absorption studies. Interestingly, the rate constant for the back electron transfer in **SWNT-Au-Ru^{2+}** is two orders of magnitude slower than the forward electron transfer (k_{ET}/k_{BET} = 10^2) which provides newer possibilities for designing energy conversion systems based on nanoparticle decorated carbon nanotubes.

Scheme 3.6. Light induced processes in SWNT-Ru$_L^{2+}$ and SWNT-Au-Ru^{2+}.

Electron Transfer Driven by Au-SWNT Heterojunctions: Excited state of $Ru(bpy)_3^{2+}$ can undergo reductive as well as oxidative quenching with donor/acceptor systems depending on the driving force of the reaction.[82] Photoconductivity studies have shown that the oxidative quenching of $*Ru(bpy)_3^{2+}$ is not observed when bound to **SWNT** surface.[85] Similar results were observed in the present case wherein the luminescence of $Ru(bpy)_3^{2+}$ on **SWNT** is retained at lower loadings, indicating the absence of electron transfer. Thus, based on the luminescence lifetime and transient absorption studies it is concluded that photoinduced electron transfer is not observed from $Ru(bpy)_3^{2+}$ neither to Au nanoparticles (Chapter 2) nor to **SWNT** when these components are linked directly. However, a unidirectional electron flow was observed from $*Ru(bpy)_3^{2+}$ to **SWNT** when linked through Au nanoparticles. It is well established that the heterojunctions of **SWNT**-metal[24] as well as **SWNT**-semiconductor[37] play a significant role in modulating the electronic properties of hybrid materials. In a recent report, Kauffman and Star have demonstrated that the potential barrier existing at the **SWNT**-metal nanoparticle interface is related to the work function of the respective metal.[24] In the present case, the charge redistribution at the **SWNT-Au** nanoparticle interface, due to Fermi level alignment, results in the formation of a localized depletion layer on **SWNT** walls which acts as deep acceptor states[23,54] (Scheme 3.7). Thus, the **SWNT-Au** heterojunctions drive the electron transfer from the $*Ru(bpy)_3^{2+}$ to carbon nanotubes. These studies can be further extended by decorating **SWNT** with a variety of metal nanoparticles which in combination with appropriate molecular systems may have the potential application for the design of efficient photovoltaic devices.

Scheme 3.7. Schematic representation of heterojunction driven electron transfer.

3.4. Conclusions

The modified electronic properties at the heterojunctions of Au nanoparticle decorated single walled carbon nanotubes (**SWNT**) have been utilized for photoinduced electron transfer by anchoring a photoactive molecule, namely ruthenium trisbipyridine ($Ru(bpy)_3{}^{2+}$). On the basis of the steady state and time resolved studies, it is concluded that the electron transfer take place from $^*Ru(bpy)_3{}^{2+}$ to Au decorated **SWNT**. However, no electron transfer process was observed from the photoexcited chromophores to **SWNT** or Au nanoparticles when these components are linked directly (Scheme 3.8). From these results, it is further concluded that the electronic properties at the heterojunctions of **SWNT-Au** nanoparticles are distinctly different from that of the isolated components due to the charge redistribution at the interface. The localized depletion layer at the **SWNT** walls may act as acceptor sites for electrons from the excited chromophores, leading to forward electron transfer. The charge separated intermediates in these multicomponent systems are stable for several

nanoseconds and the high ratio of forward to back electron transfer ($k_{ET}/k_{BET} = 10^2$) makes these hybrid nanosystems promising for energy conversion and optoelectronic applications. The intriguing electronic properties of these heterojunctions can be further modified by decorating **SWNT** with suitable metal nanoparticles and photoresponsive units which can lead to the development of a new generation of photoactive hybrid nanomaterials.

Scheme 3.8. Light induced processes in **SWNT-Ru$_L$$^{2+}$** and **SWNT-Au-Ru^{2+}**
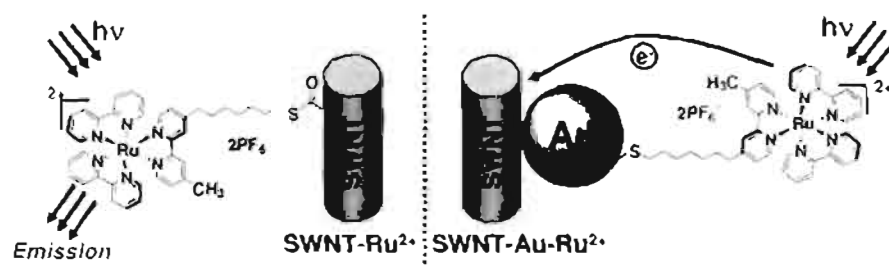
3.5. Experimental Section
3.5.1. Materials and Instrumental Techniques

Solvents and reagents used were purified and dried by standard methods. Photophysical studies were carried out using spectroscopic grade solvents. The thermogravimetric analyses were performed with a TGA-50 Shimadzu thermogravimetric analyzer at a heating rate of 10°C/min in nitrogen. FTIR spectra were recorded on a IRPrestige-21 Shimadzu infrared spectrophotometer. For the TEM analyses, samples were prepared by drop casting dilute solution from the cuvette on a carbon coated Cu grid and the solvent was allowed to evaporate and specimens

were investigated with a FEI-Tecnai 30G^{2}S-Twin operated at an accelerating voltage of 300 kV. The UV-vis spectra were recorded on a Shimadzu 3101PC spectrophotometer. The emission spectra were recorded on a Spex-Fluorolog, F112-X equipped with a 450W Xe lamp and a Hamamatsu R928 photomultiplier tube. The spectra were recorded by keeping a 90° geometry and a slit width of 1 nm in the excitation and emission monochromators at an excitation wavelength of 453 nm. Luminescence lifetimes were measured using IBH (Florocube) Time-Correlated Picosecond Single Photon Counting (TCSPC) system. Solutions were excited with a pulsed diode laser (<100 ps pulse duration) at a wavelength of 440 nm (NanoLED) with a repletion of 100 KHz. The detection system consisted of a Micro Channel Plate (MCP) photomultiplier (5000U-09B, Hamamastu) with a 38.6 ps response time coupled to a monochromator (500M) and TCSPC electronics (Data Station Hub including Hub-NL, NanoLED controller and preinstalled luminescence measurement and analysis studio (FMAS) software). The luminescence lifetime values were obtained using DAS6 decay analysis software. The quality of the fit has been judged by the fitting parameters such χ^2 (1 $\pm$ 0.1) Nanosecond laser flash photolysis experiments were carried out using an Applied Photophysics Model LKS-20 Laser Spectrometer using the third harmonic (355 nm, ~70 mJ/pulse) of a Qunta Ray GCR-12 series pulsed Nd:YAG laser with a pulse duration of ~8 ns .

3.5.2. Preparation of Carboxylated SWNT, SWNT-CO$_2$H

20 mg of purified sample of **SWNT** was treated with a mixture (3:1) of H$_2$SO$_4$ and HNO$_3$ (25 mL). The content was then refluxed for 24 h at 70°C in an oil bath. The carboxylated nanotubes were centrifuged for 4-5 times at 5000 rpm (20 min each) until the filtrate became neutral. The carboxylated nanotubes were then dried over vacuum for 12 h at 90°C. The product was characterized using FTIR (KBr): CO stretching at 1733 cm^{-1}.

3.5.3. Preparation of SWNT-COCl

The thionylation was carried out by treating 15 mg of **SWNT-CO$_2$H** with thionyl chloride (10 mL) with catalytic amount of dry DMF (0.5 mL). The reaction mixture was refluxed at 70°C for 24 h and then centrifuged for 4 times at 5000 rpm (20 min each). The thionylated nanotubes were dried over vacuum at 70°C for 12 h and used in the next step without further purification.

3.5.4. Preparation of SWNT-Ru^{2+}

The **Ru(bpy)$_3$$^{2+}$** functionalized **SWNT** was prepared through a thioester linkage by the reaction between **SWNT-COCl** (5 mg) and **Ru^{2+}-C$_7$-SH** (1.5 mg) in dry THF (5 mL). The reaction mixture was stirred at room temperature for 36 h. The reaction mixture was then centrifuged at 4000 rpm for 5 min and **SWNT-Ru^{2+}** was obtained as dark residue. **SWNT-Ru^{2+}** was then redispersed in THF and centrifuged until the supernatant layer did not show any absorption corresponding to **Ru^{2+}-C$_7$-SH**. Finally the residue was redispersed in spectroscopic acetonitrile and used for

further studies. **SWNT-Ru^{2+}** having low chromophoric loadings were prepared by reducing the concentration of **Ru^{2+}-C$_7$-SH** (0.5 mg in 5 mL of THF). FTIR (KBr): CO stretching (thioester) at 1682 cm^{-1}.

3.5.5. Preparation of Thiolated SWNT, SWNT-SH

The thiolated SWNTs were prepared by treating **SWNT-COCl** (15 mg) with 2-mercaptoethylamine hydrochloride (5 mL) in dry THF (5 mL). The reaction mixture was refluxed at 70°C for 24 h and then centrifuged for four times at 5000 rpm (20 min each). The thiolated nanotubes were dried over vacuum at 70°C for 12 h. FTIR (KBr): amide I band at 1686 cm^{-1} and amide II band at 1535 cm^{-1}.

3.5.6. Preparation of SWNT-Au-Ru^{2+}

SWNT-Au-Ru^{2+} was prepared by a place exchange reaction between **SWNT-SH** and **Au-Ru^{2+}** in dry THF (2 mL). After 36 h of room temperature stirring, the reaction mixture was centrifuged at 4000 rpm for 5 min and **SWNT-Au-Ru^{2+}** was obtained as dark residue. **SWNT-Au-Ru^{2+}** was then redispersed in dry THF and centrifuged until the supernatant layer did not show any absorption corresponding to **Au–Ru^{2+}**. Finally the residue was redispersed in spectroscopic acetonitrile and used for further studies.

3.6. References

(1)   (a) Barber, J.; Andersson, B. *Nature* **1994**, *370*, 31; (b) Ferreira, K. N.; Iverson, T. M.; Maghlaoui, K.; Barber, J.; Iwata, S. *Science* **2004**, *303*, 1831.

(2)   Deisenhofer, J.; Michel, H. *Angew. Chem. Int. Ed.* **1989**, *28*, 829.

(3)   (a) Huber, R. *Angew. Chem. Int. Ed.* **1989**, *28*, 848; (b) Bixon, M.; Fajer, J.; Feher, G.; Freed, J. H.; Gamliel, D.; Hoff, A. J; Levanon, H.; Mobius, K.; Nechushtai, R.; Norris, J. R.; Scherz, A.; Sessler, J. L.; Stehlik, D. *Isr. J. Chem.* **1992**, *32*, 369.

(4)   (a) Kavarnos, G. J. *Fundamentals of Photoinduced Electron Transfer*, VCH, New York, **1993**; (b) Grätzel M. (ed.), *Heterogeneous Photoinduced Electron Transfer*, CRC Rublishers, Boca Raton, FL, **1998**; (c) Marcus, R. A. *Angew. Chem. Int. Ed.* **1993**, *32*, 1111.

(5)   (a) Guldi, D. M.; Prato, M. *Acc. Chem. Res.* **2000**, *33*, 695; (b) Guldi, D. M.; Rahman, G. M. A.; Zerbetto, F.; Prato, M. *Acc. Chem. Res.* **2005**, *38*, 871; (c) Nazario, M. N.; Luis, S. L.; Herranz, M.; Beatriz, I. B.; Guldi D. M. *Acc. Chem. Res.* **2007**, *40*, 1025.

(6)   Thomas, K. G.; Kamat, P. V. *Acc. Chem. Res.* **2003**, *36*, 888.

(7)   Iijima, S.; Ichihashi, T. *Nature* **1993**, *363*, 603.

(8)   Bethune, D. S.; Klang, C. H.; de Vries, M. S.; Gorman, G.; Savoy, R.; Vazquez, J.; Beyers, R. *Nature* **1993**, *363*, 605.

(9)   Dresselhaus, M. S.; Dresselhaus, G.; Eklund, P. C. *Science of Fullerenes and Carbon Nanotubes*, Academic Press, San Diego, CA, 1996.

(10)   Vivekchand, S. R. C.; Govindaraj, A.; Rao, C. N. R. in *Nanomaterials Chemistry Recent Developments and New Directions*, (Eds: Rao, C. N. R.; Müller, A.; Cheetham, A. K.), WILEY-VCH, Weinheim, 2007, p 45.

(11)   Liz-Marzán, L. M. *Langmuir* **2006**, *22*, 32.

(12)   O'Connell, M. J.; Bachilo, S. M.; Huffman, C. B.; Moore, V. C.; Strano, M. S.; Haroz, E. H.; Rialon, K. L.; Boul, P. J.; Noon, W. H.; Kittrell, C.; Ma, J.; Hauge, R. H.; Weisman, R. B.; Smalley, R. E. *Science* **2002**, *297*, 593.

(13)   Avouris, P. *Acc. Chem. Res.* **2002**, *35*, 1026.

(14)   Ajayan, P. M. *Chem. Rev.* **1999**, *99*, 1787.

(15)   Wong, S. S.; Joselevich, E.; Woolley, A. T.; Cheung, C. L.; Lieber, C. M. *Nature* **1998**, *394*, 52.

(16)   Ebbesen, T. W.; Lezec, H. J.; Hiura, H.; Bennett, J. W.; Ghaemi, H. F.; Thio, T. *Nature* **1996**, *382*, 54.

(17)   Kovtyukhova, N. I.; Mallouk, T. E. *Adv. Mater.* **2005**, *17*, 187.

(18)   Kovtyukhova, N. I.; Mallouk, T. E.; Pan, L.; Dickey, E. C. *J. Am. Chem. Soc.* **2003**, *125*, 9761.

(19)   Rinzler, A. G.; Hafner, J. H.; Nikolaev, P.; Nordlander, P.; Colbert, D. T.; Smalley, R. E.; Lou, L.; Kim, S. G.; Tomanek, D. *Science* **1995**, *269*, 1550.

(20)   de Heer, W. A.; Châtelain, A.; Ugarte, D. *Science* **1995**, *270*, 1179.

(21)   Javey, A.; Guo, J.; Wang, Q.; Lundstrom, M.; Dai, H. *Nature* **2003**, *424*, 654.

(22)   Postma, H. W. C.; Teepen, T.; Yao, Z.; Grifoni, M.; Dekker, C. *Science* **2001**, *293*, 76.

(23)   Kauffman, D. R.; Star, A. *Small* **2007**, *3*, 1324.

(24)   Kauffman, D. R.; Star, A. *Nano Lett.* **2007**, *7*, 1863.

(25)   Allen, B. L.; Kichambare, P. D.; Star, A. *Adv. Mater.* **2007**, *19*, 1439.

(26)   Star, A.; Joshi, V.; Skarupo, S.; Thomas, D.; Gabriel, J. C. P. *J. Phys. Chem. B* **2006**, *110*, 21014.

(27)   Chichak, K. S.; Star, A.; Altoé, M. V. P.; Stoddart, J. F. *Small* **2005**, *1*, 452.

(28)   Pushparaj, V. L.; Shaijumon, M. M.; Kumar, A.; Murugesan, S.; Ci, L.; Vajtai, R.; Linhardt, R. J.; Nalamasu, O.; Ajayan, P. M. *Proc. Natl. Acad. Sci. U. S. A.* **2007**, *104*, 13574.

(29)   Guldi, D. M. *Nature* **2007**, *447*, 50.

(30)   Cioffi, C.; Campidelli, S.; Sooambar, C.; Marcaccio, M.; Marcolongo, G.; Meneghetti, M.; Paolucci, D.; Paolucci, F.; Ehli, C.; Rahman, G. M. A.; Sgobba, V.; Guldi, D. M.; Prato, M. *J. Am. Chem. Soc.* **2007**, *129*, 3938.

(31)   Guldi, D. M. *J. Phys. Chem. B* **2005**, *109*, 11432.

(32)   Campidelli, S.; Sooambar, C.; Lozano-Diz, E.; Ehli, C.; Guldi, D. M.; Prato, M. *J. Am. Chem. Soc.* **2006**, *128*, 12544.

(33)   Guldi, D. M.; Marcaccio, M.; Paolucci, D.; Paolucci, F.; Tagmatarchis, N.; Tasis, D.; Vázquez, E.; Prato, M. *Angew. Chem. Int. Ed.* **2003**, *42*, 4206.

(34)   Alvaro, M.; Aprile, C.; Ferrer, B.; Garcia, H. *J. Am. Chem. Soc.* **2007**, *129*, 5647.

(35)   Alvaro, M.; Atienzar, P.; delaCruz, P.; Delgado, J. L.; Troiani, V.; Garcia, H.; Langa, F.; Palkar, A.; Echegoyen, L. *J. Am. Chem. Soc.* **2006**, *128*, 6626.

(36)   Alvaro, M.; Atienzar, P.; Bourdelande, J. L.; Garcia, H. *Chem. Phys. Lett.* **2004**, *384*, 119.

(37)   Kongkanand, A.; Kamat, P. V. *ACS Nano* **2007**, *1*, 13.

(38)   Kamat, P. V. *J. Phys. Chem. C* **2007**, *111*, 2834.

(39)   Vietmeyer, F.; Seger, B.; Kamat, P. V. *Adv. Mater.* **2007**, *19*, 2935.

(40)   Robel, I.; Bunker, B. A.; Kamat, P. V. *Adv. Mater.* **2005**, *17*, 2458.

(41)   Kamat, P. V.; Thomas, K. G.; Barazzouk, S.; Girishkumar, G.; Vinodgopal, K.; Meisel, D. *J. Am. Chem. Soc.* **2004**, *126*, 10757.

(42)   Girishkumar, G.; Vinodgopal, K.; Kamat, P. V. *J. Phys. Chem. B* **2004**, *108*, 19960.

(43)   Hasobe, T.; Fukuzumi, S.; Kamat, P. V. *J. Phys. Chem. B* **2006**, *110*, 25477.

(44)   Hasobe, T.; Fukuzumi, S.; Kamat, P. V. *J. Am. Chem. Soc.* **2005**, *127*, 11884.

(45)   Katz, E.; Willner, I. *ChemPhysChem* **2004**, *5*, 1084.

(46)   Kam, N. W. S.; O'Connell, M.; Wisdom, J. A.; Dai, H. *Proc. Natl. Acad. Sci. U. S. A.* **2005**, *102*, 11600.

(47)   Kam, N. W. S.; Dai, H. *J. Am. Chem. Soc.* **2005**, *127*, 6021.

(48)   Singh, R.; Pantarotto, D.; Lacerda, L.; Pastorin, G.; Klumpp, C.; Prato, M.; Bianco, A.; Kostarelos, K. *Proc. Natl. Acad. Sci. U. S. A.* **2006**, *103*, 3357.

(49) Wu, W.; Wieckowski, S.; Pastorin, G.; Benincasa, M.; Klumpp, C.; Briand, J.-P.; Gennaro, R.; Prato, M.; Bianco, A. *Angew. Chem. Int. Ed.* **2005**, *44*, 6358.

(50) Georgakilas, V.; Gournis, D.; Tzitzios, V.; Pasquato, L.; Guldi, D. M.; Prato, M. *J. Mater. Chem.* **2007**, *17*, 2679.

(51) Sheeney-Haj-Ichia, L.; Basnar, B.; Willner, I. *Angew. Chem. Int. Ed.* **2005**, *44*, 78.

(52) Ioannides, T.; Verykios, X. E. *J. Catal.* **1996**, *161*, 560.

(53) Chen, X. H.; Moskovits, M. *Nano Lett.* **2007**, *7*, 807.

(54) Chen, X.; Lee, S. J.; Moskovits, M. *Appl. Phys. Lett.* **2007**, *91*, 082109.

(55) Grzelczak, M.; Correa-Duarte, M. A.; Salgueiriño-Maceira, V.; Giersig, M.; Diaz, R.; Liz-Marzán, L. M. *Adv. Mater.* **2006**, *18*, 415.

(56) Correa-Duarte, M. A.; Pérez-Juste, J.; Sánchez-Iglesias, A.; Giersig, M.; Liz-Marzán, L. M. *Angew. Chem., Int. Ed.* **2005**, *44*, 4375.

(57) Jiang, K.; Eitan, A.; Schadler, L. S.; Ajayan, P. M.; Siegel, R. W.; Grobert, N.; Mayne, M.; Reyes-Reyes, M.; Terrones, H.; Terrones, M. *Nano Lett.* **2003**, *3*, 275.

(58) Ellis, A. V.; Vijayamohanan, K.; Goswami, R.; Chakrapani, N.; Ramanathan, L. S.; Ajayan, P. M.; Ramanath, G. *Nano Lett.* **2003**, *3*, 279.

(59) Voggu, R.; Suguna, P.; Chandrasekaran, S.; Rao, C. N. R. *Chem. Phys. Lett.* **2007**, *443*, 118.

(60) Juris, A.; Balzani, V.; Barigelletti, F.; Campagna, S.; Belser, P.; von Zelewsky, A. *Coord. Chem. Rev.* **1988**, *84*, 85.

(61) Armaroli, N.; Balzani, V. *Angew. Chem. Int. Ed.* **2007**, *46*, 52.

(62) Hagfeldt, A.; Grätzel, M. *Acc. Chem. Res.* **2000**, *33*, 269.

(63) Haque, S. A.; Handa, S.; Peter, K.; Palomares, E.; Thelakkat, M.; Durrant, J. R. *Angew. Chem. Int. Ed.* **2005**, *44*, 5740.

(64) Myahkostupov, M.; Piotrowiak, P.; Wang, D.; Galoppini, E. *J. Phys. Chem. C* **2007**, *111*, 2827.

(65)   Lundqvist, M. J.; Galoppini, E.; Meyer, G. J.; Persson, P. *J. Phys. Chem. A* **2007**, *111*, 1487.

(66)   Galoppini, E. *Coord. Chem. Rev.* **2004**, *248*, 1283.

(67)   Kim, Y.; Lee, H.; Dutta, P. K.; Das, A. *Inorg. Chem.* **2003**, *42*, 4215.

(68)   Ledney, M.; Dutta, P. K. *J. Am. Chem. Soc.* **1995**, *117*, 7687.

(69)   Borja, M.; Dutta, P. K. *Nature* **1993**, *362*, 43.

(70)   Yonemoto, E. H.; Saupe, G. B.; Schmehl, R. H.; Hubig, S. M.; Riley, R. L.; Iverson, B. L.; Mallouk, T. E. *J. Am. Chem. Soc.* **1994**, *116*, 4786.

(71)   Morris, N. D.; Mallouk, T. E. *J. Am. Chem. Soc.* **2002**, *124*, 11114.

(72)   Wang, Y. S.; Liu, S. X.; Pinto, M. R.; Dattelbaum, D. M.; Schoonover, J. R.; Schanze, K. S. *J. Phys. Chem. A* **2001**, *105*, 11118.

(73)   Walters, K. A.; Trouillet, L.; Guillerez, S.; Schanze, K. S. *Inorg. Chem.* **2000**, *39*, 5496.

(74)   Pramod, P.; Sudeep, P. K.; Thomas, K. G.; Kamat, P. V. *J. Phys. Chem. B* **2006**, *110*, 20737.

(75)   Soller, T.; Ringler, M.; Wunderlich, M.; Klar, T. A.; Feldmann, J.; Josel, H. P.; Markert, Y.; Nichtl, A.; Kurzinger, K. *Nano Lett.* **2007**, *7*, 1941.

(76)   Liu, J.; Rinzler, A. G.; Dai, H.; Hafner, J. H.; Bradley, R. K.; Boul, P. J.; Lu, A.; Iverson, T.; Shelimov, K.; Huffman, C. B.; Rodriguez-Macias, F.; Shon, Y.-S.; Lee, T. R.; Colbert, D. T.; Smalley, R. E. *Science* **1998**, *280*, 1253.

(77)   Chen, J.; Hamon, M. A.; Hu, H.; Chen, Y.; Rao, A. M.; Eklund, P. C.; Haddon, R. C. *Science* **1998**, *282*, 95.

(78)   Andreas, H. *Angew. Chem. Int. Ed.* **2002**, *41*, 1853.

(79)   Tasis, D.; Tagmatarchis, N.; Bianco, A.; Prato, M. *Chem. Rev.* **2006**, *106*, 1105.

(80)   Kim, Y.-T.; Ohshima, K.; Higashimine, K.; Uruga, T.; Takata, M.; Suematsu, H.; Mitani, T. *Angew. Chem. Int. Ed.* **2006**, *45*, 407.

(81)   Accorsi, G.; Armaroli, N.; Parisini, A.; Meneghetti, M.; Marega, R.; Prato, M.; Bonifazi, D. *Adv. Funct. Mater.* **2007**, *17*, 2975.

(82) Lomoth, R.; Häupl, T.; Johansson, O.; Hammarström, L. *Chem.-- Eur. J.* **2002**, *8*, 102.

(83) Mulazzani, Q. G.; Emmi, S.; Fuochi, P. G.; Hoffman, M. Z.; Venturi, M. *J. Am. Chem. Soc.* **1978**, *100*, 981.

(84) Navon, G.; Sutin, N. *Inorg. Chem.* **1974**, *13*, 2159.

(85) Khairoutdinov, R. F.; Doubova, L. V.; Haddon, R. C.; Saraf, L. *J. Phys. Chem. B* **2004**, *108*, 19976.

CHAPTER 4

Exploring the Edge Effects in Gold Nanorods

4.1. Abstract

The stability of Au nanorods and nanoparticles was investigated in water-acetonitrile mixtures and correlated with their zeta potential (ζ) values. For Au nanorods, a sigmoidal plot was obtained on plotting ζ as a function of water-acetonitrile compositions. In water, nanorods are stable and possess a high positive ζ whose magnitude increases linearly with aspect ratio. On further increase in acetonitrile composition, ζ decreases and crosses through a zero value to high negative values. Variations in ζ by changing the solvent compositions are attributed to the collapse in the CTAB bilayer structure on the surface of nanorod, to monolayer and further results in the removal of organic molecules. In contrast, ζ of Au nanoparticles, protected with triethylene glycol thiol, varied linearly with particle size due to increase in their surface charge density, however not influenced by solvent composition changes. Based on theoretical studies, it is proposed that the electric field intensity is higher at the sharp edges of anisotropic nanostructures. These aspects were experimentally verified by investigating the interaction between the positively charged Au nanoparticles and negatively charged Au nanorods. A spontaneous

bathochromic shift in the longitudinal plasmon band of Au nanorods was observed on addition of Au nanoparticles whereas the position of transverse plasmon band remains unaffected. HRTEM studies showed a preferential close packing of Au nanoparticles at the edges of Au nanorods which leads to the changes in longitudinal plasmon oscillation frequency. A strong dependency on the nanoparticles' size on the relative shift in the longitudinal band was observed: a large shift for smaller nanoparticles which is correlated to their ζ values. The reactivity at the edges of Au nanorods was further investigated by linking them as dimers and oligomers. Plasmon coupling in dimers of Au nanorods was investigated as a function of their orientation using a flexible (**C₆DT**) and rigid (**PDT**) linkers. The plasmon coupling in **PDT** linked Au nanorod dimers is found to be more pronounced due to effective dipolar overlap along their long axes.

4.2. Introduction

Nanostructures of noble metals can convert photons into surface plasmon and within the propagation length, the surface plasmon modes can be decoupled back to light.[1-4] Since surface plasmons are not diffraction limited, this strategy offers numerous possibilities in the design of nanoscale optoelectronic and photonic devices.[1b,2-4] Organized nanostructures can be designed through the stepwise integration of various nanoscale building blocks such as nanoparticles, nanorods and nanotubes. Theoretical methods have been utilized for investigating electromagnetic interactions in arrays of spherical nanoparticles by varying their particle size, array spacing, array symmetry and polarization

direction.[6-10] These aspects were experimentally verified by linking nanoparticles into nanochains.[1b] However, isotropic nature of spherical nanoparticles prevent the selective binding of molecules on surfaces which limits the possibility of designing 1D nanomaterials by chemical functionalization methods. More recently, a notable success has been achieved in the linear organization of spherical nanoparticles by utilizing the singularities present in the rippled Au nanoparticles.[11] The present study focuses on two fundamental properties observed at the edges of Au nanorods, namely the high electric field and reactivity. These properties were effectively utilized for hierarchical integration of Au nanorods.

4.2.1. Electric Field at the Edges of Anisotropic Materials

It is well known that air around sharp points or edges may become ionized producing the corona discharge during thunderstorm.[12] Such corona discharges are often the precursors of lightning strike and termed as spark discharge from a charged conductor.[12] The phenomenon originates from the distribution of surface charges on anisotropic conductors. At sharp points and sharp edges, the surface charge density as well as the external electric field (which is proportional to the later one) may reach high value. The edge effect of metallic rods has been utilized for protecting buildings. The lightning rod has a sharp end and the lightning bolts pass through a conducting path in air to the rod, thus protecting the nearby structures from damage.

The divergence of the electric field and charge accumulation at the edges and corners of a conductor at a fixed potential is termed as "*edge*

effect.[13] Edge effect is a natural phenomenon which has a common use in day to day life. The baking of potato wedges constitutes a crunchy example of edge effects. which are usually demonstrated in electrostatics.[13] A simple model of the diffusive transport of water vapor around the potato wedges showed that the water vapor flux diverges at the sharp edges in analogy with its electrostatic counterpart. This increased evaporation at the edges lead to the crispy taste of these parts of the potatoes (Figure 4.1).
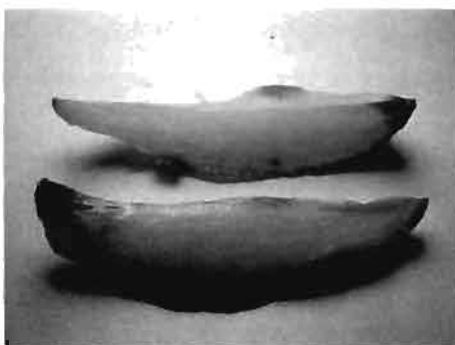

Figure 4.1. Two baked potato wedges. The edges are seen to be darker, showing dehydration in these regions. The effect is stronger at the extremities of the wedge (*adapted from reference 13*).

Nanostructured Materials: An experimental evidence for the edge effect in nanomaterials has been recently demonstrated in the case of MoS_2 wherein the active edge sites were involved in the electrochemical H_2 evolution.[14] By preparing MoS_2 nanoparticles of different sizes, the authors have systematically varied the distribution of surface sites on MoS_2 nanoparticles (deposited on Au(111); Figure 4.2), which were quantified with scanning tunneling microscopy. Electrocatalytic activity measurements

showed a linear correlation of H_2 evolution with the number of edge sites on the MoS_2 catalyst.
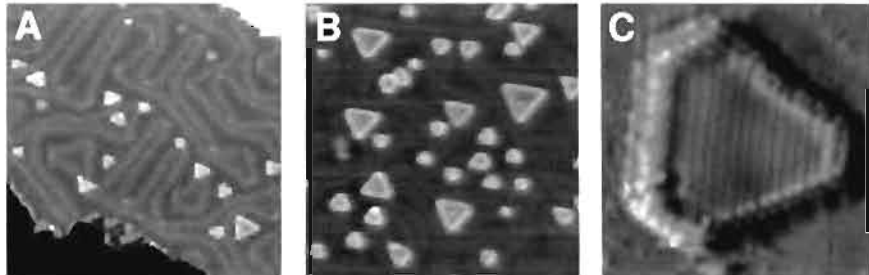

Figure 4.2. A series of STM images of MoS_2 nanoparticles on Au (111) surface at different surface coverage: (A) low coverage (B) high coverage and (C) atomically resolved MoS_2 particle showing the predominance of the sulfide Mo-edge (*adapted from reference 14*).

Electric field intensity enhancements at the edges of nanomaterials have been successfully demonstrated by theoretical methods.[15] Electric field intensity enhancement contours calculated using finite difference time domain (FDTD) for nanomaterials of various shapes are shown in Figure 4.3.[15] From these images, it is clear that the electric fields are more
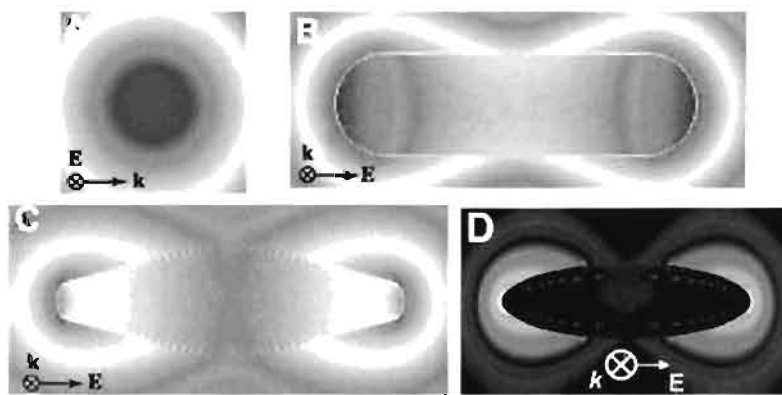

Figure 4.3. Electric field intensity enhancement contours along the longitudinal direction for a nanosphere, nanorod, nanobipyramid and nanorice obtained from FDTD calculation (*adapted from reference 15*).

concentrated on the edges and corners. The maximal field intensity enhancement of nanorod is found to be about one sixth of that of the bipyramid, indicating that the field enhancement is mainly determined by the shape of the nanoparticles.

Au Nanorods: One of the well accepted mechanisms for Au nanorod growth is based on the high electric field at their edges.[16] The mechanism proposed by Pérez-Juste *et al.*[16] suggested the reduction of Au(III) ions to Au(I) ions which further complexes with CTAB micelle. The slow collision frequency and the enhanced electric field at the tips allow the reduction of Au(I) almost exclusively, to take place at the termini (Figure 4.4).
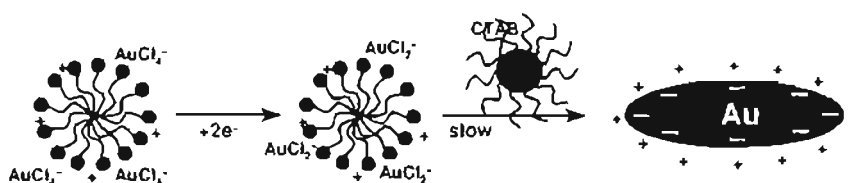

Figure 4.4. Suggested mechanism for gold nanorod formation. $AuCl_4$ ions are bound to cationic CTAB micelles, displacing Br⁻ ions (*adapted from reference 16*).

Zeta Potential: For the effective utilization of the electric fields concentrated at the edges, an understanding on the surface charges, zeta potential (ζ), of anisotropic nanostructures is very important. The development of a net charge at the particle surface affects the distribution of ions in the surrounding interfacial region. This results in an increased concentration of counter ions (ions of opposite charge to that of the particle) close to the surface. This results in the formation of an electrical double layer around each particle. Liquid layer surrounding the particle

exists as two parts (Figure 4.5): an inner region called *Stern layer* (colored
in white) where the ions are strongly bound and an outer *diffuse region*
(colored in brown) where they are less firmly associated. Within the diffuse
layer there is a notional boundary and inside this, ions and particles form a
stable entity. When a particle moves (e.g. due to gravity), ions within the
boundary also moves along with it and ions beyond the boundary stay with
the bulk dispersant. The double layer is formed in order to neutralize the
charged colloid. This, in turn, causes an electrokinetic potential between
the surface of the colloid and at any point in the mass of the suspending
liquid. This voltage difference is in the order of millivolts and referred as
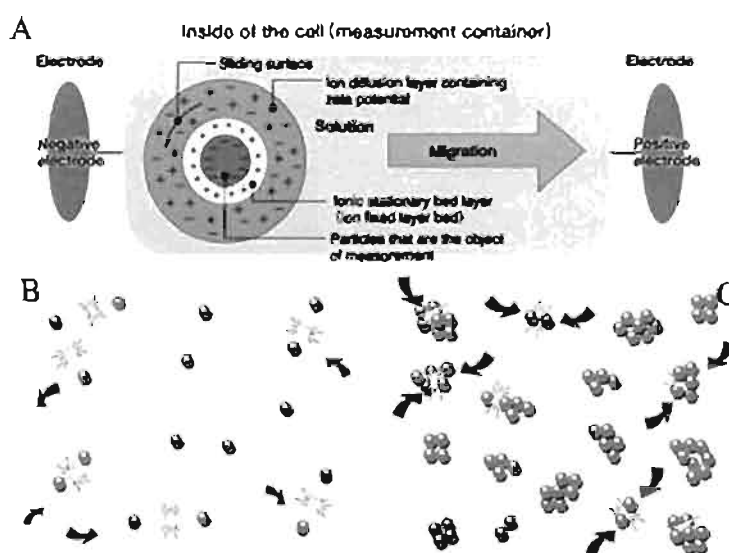surface potential.

Figure 4.5. (A) Schematic representation of double layer resulting in zeta
potential, (B) charged particles dispersed in a medium as they repel each other.
(C) uncharged particles are free to collide and aggregate (*adapted from
reference 17*).

A charged particle will move with a fixed velocity in a voltage field. This phenomenon is called *electrophoresis*. The mobility of particles is related to the dielectric constant and viscosity of the suspending liquid and to the electrical potential at the boundary between the moving particle and the liquid. This boundary is called the *slip plane* and is usually defined as the point where the *Stern layer* and the *diffuse layer* meet. The *Stern layer* is considered to be rigidly attached to the colloid, while the *diffuse layer* is not. As a result, the electrical potential at this junction is related to the surface charge of the particle and is called the "*zeta potential*".[17]

When a voltage is applied to the solution, the dispersed particles are attracted to the electrode of opposite polarity, accompanied by the stern layer and part of the diffuse double layer. Zeta potential can be quantified by measuring the electrophoretic mobility as the colloidal particle migrates in an applied field. Further, the electrophoretic mobility (U) is related to zeta potential (ζ) by Smoluchowski's formula (Equation 4.1),

$$\zeta = 4\pi\eta/\varepsilon \times U \times 300 \times 300 \times 1000 \qquad (4.1)$$

where 'η' is viscosity of the solution and 'ε' is the dielectric constant.

The magnitude of the zeta potential is an indicator of the potential stability of the colloidal system. If all the particles in suspension have a large negative or positive zeta potential then they will tend to repel each other (Figure 4.5B). However, if the particles have low zeta potential values then there will be no force which prevents the particles from approaching each other and flocculating (Figure 4.5C). The dividing line

between stable and unstable colloidal systems is generally taken as either +30 or -30 mV.[18]

High Edge Reactivity of Au Nanorods: On the basis of electron diffraction analysis and HRTEM studies, it is proposed that the end facets of Au nanorods are dominated by {111} planes and the side facets by {100} and {110} planes.[19-21] A surfactant-directed nanorod growth mechanism was proposed by Murphy and co-workers which involves the differential blocking of certain crystallographic facets of Au nanorod ({100} or {110}) by CTAB which promotes the anisotropic growth of the {111} edges (Figure 4.6).[19] It is reported that the thiol derivatives preferentially binds to the {111} planes of the Au nanorods and this specific interaction was further exploited for the organization of Au nanorods.[22-24]
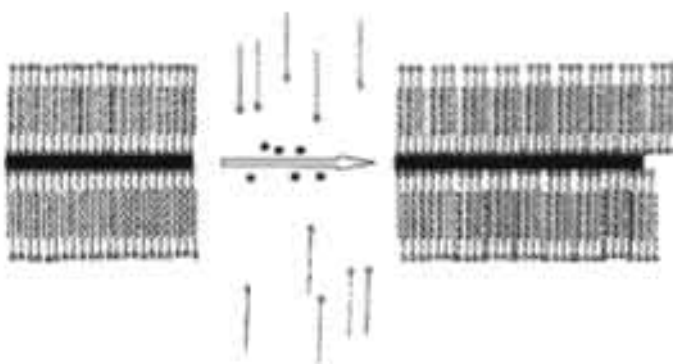

Figure 4.6. Cartoon illustrating the formation of the bilayer of CTAB molecules on the surface of Au nanorod (black rectangle) that may assist nanorod formation as more gold ions (black dots) are introduced *(adapted from reference 22).*

The preferential functionalization at the edges of Au nanorods lead to the formation of 1D nanochain in the longitudinal direction, which is well documented in the literature.[24-27] A detailed mechanistic investigation on

the end-to-end assembly of Au nanorods to nanochains using α,ω-dithiols has been carried out by Thomas and coworkers.[24c] On the basis of these studies, it is concluded that the nanochain formation proceeds through an incubation step followed by the dimerization and subsequent oligomerization of nanorods in a preferential end-to-end fashion (Scheme 4.1). During the incubation step, nanorods remain isolated and no changes in the plasmon absorption bands were observed. These results indicate that one of the thiol groups of α,ω-dithiols preferentially binds on to the edges of the nanorods in the incubation period, leaving the other thiol group free. After the incubation step, nanorods were brought together as nanochains through dithiol linkage, resulting in interplasmon coupling. The clear isosbestic point observed in the time dependent absorption spectrum
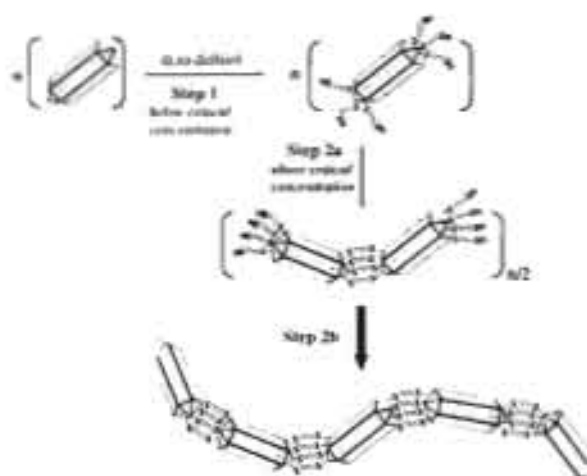
**Scheme 4.1.** Generalized scheme showing the stepwise formation of nanochains: step 1 denotes 'incubation step', step 2a denotes 'dimerization step' and step 2b denotes the 'oligomerization' of dimers to nanochains *(adapted from reference 24c)*.

and dimers observed in the TEM micrographs confirm the involvement of the dimerization step in the chain up process. The spectral changes were analyzed for a second-order kinetic process, and linearity in the initial period further supports the dimerization mechanism which deviates with time due to the contribution of other complex processes.

The studies presented above clearly indicate that the edges of Au nanorods are highly reactive and the electric field is concentrated more at the edges than the lateral faces. Herein, we report two novel approaches for exploiting these effects in Au nanorods: (i) the high electric field for the preferential assembly of nanomaterials at the edges through an electrostatic approach (Scheme 4.2) and (ii) the reactivity at the edges for covalent functionalization of nanorods as dimers and their plasmon coupling (Scheme 4.3).
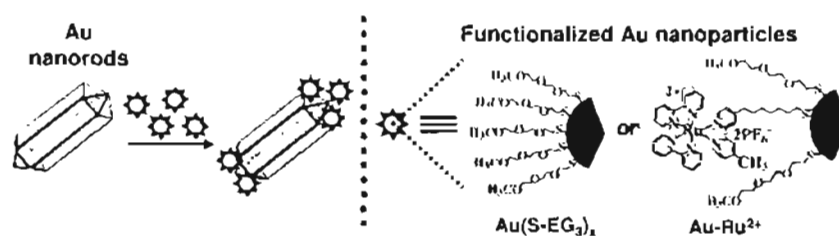
Scheme 4.2. Schematic representation for the site-specific functionalization of Au nanorods.
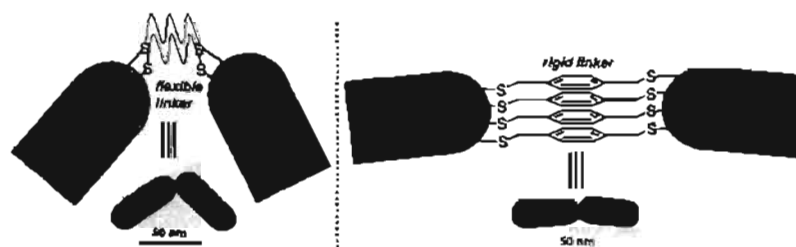
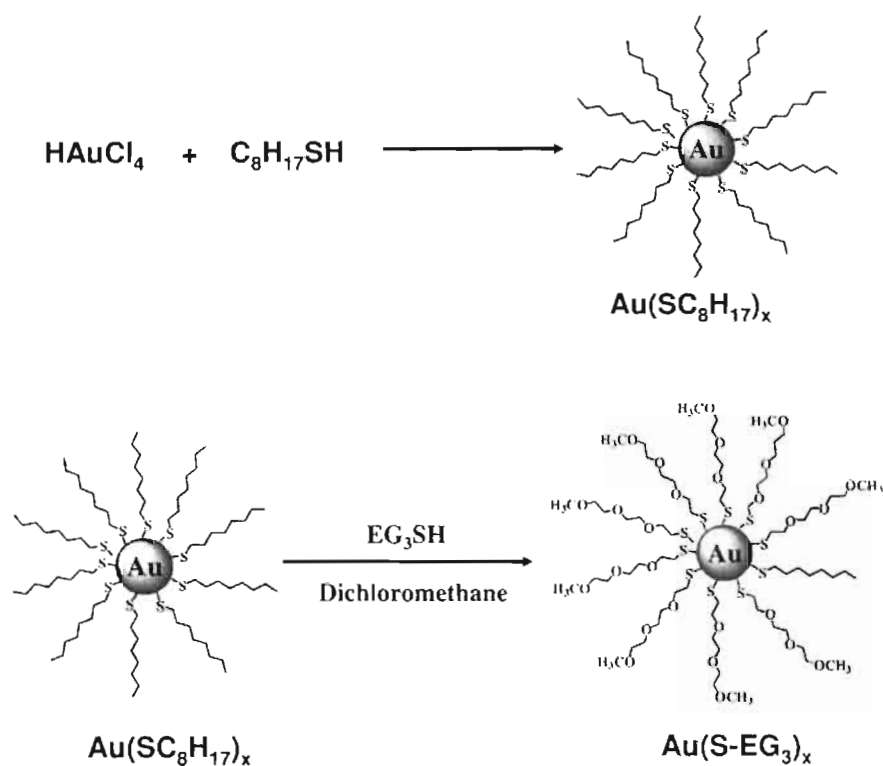**Scheme 4.3.** Plasmon coupling in dimers of Au nanorods.

4.3. Results and Discussion

4.3.1. Synthesis and Characterization

For investigating the high electric field observed at the edges of anisotropic nanostructures, we have selected two types of Au nanomaterials namely Au nanorods and spherical Au nanoparticles. Au nanorods of varying aspect ratios (~2.2, 2.7, 3.0 and 3.7) were synthesized by adopting a modified photochemical procedure.[28] Details of the synthetic procedure adopted are presented in Section 4.5. Spherical Au nanoparticles, of varying diameters (1.8-5.7 nm), protected by triethylene glycol thiol (**Au(S-EG$_3$)$_x$**) were synthesized according to a modified literature procedure.[29.30] Octylmercaptan protected Au nanoparticles of three different diameters (1.8, 2.7 and 5.7 nm) were first synthesized by following a literature procedure and place exchanged with triethylene glycol thiol (Scheme 4.4).[29] Experimental details adopted for the synthesis of **Au(S-EG$_3$)$_x$** nanoparticles having 4.5 nm diameter were presented earlier in Section 2.6.8. and remaining ones in Section 4.5. Au nanoparticles and nanorods were further characterized by high resolution transmission electron microcopy (HRTEM) and details are presented below.

4.3.2. HRTEM Characterization

HRTEM images of gold nanoparticles were obtained by drop casting dilute solution on to a formvar coated copper grid (Figure 4.7). It has been observed that nanoparticles are randomly distributed all over the grid and the average diameters of Au nanoparticles were estimated to be 1.8, 2.7, 4.5 and 5.7 nm.

$$HAuCl_4 \quad + \quad C_8H_{17}SH \quad \longrightarrow$$

$$Au(SC_8H_{17})_x$$

$$Au(SC_8H_{17})_x \quad \xrightarrow[\text{Dichloromethane}]{EG_3SH} \quad Au(S\text{-}EG_3)_x$$

$$Au(SC_8H_{17})_x \qquad\qquad\qquad Au(S\text{-}EG_3)_x$$

Scheme 4.4 Synthesis of triethylene glycol thiol protected gold nanoparticles with varying sizes (1.8, 2.7 and 5.7 nm) obtained through place exchange reaction.
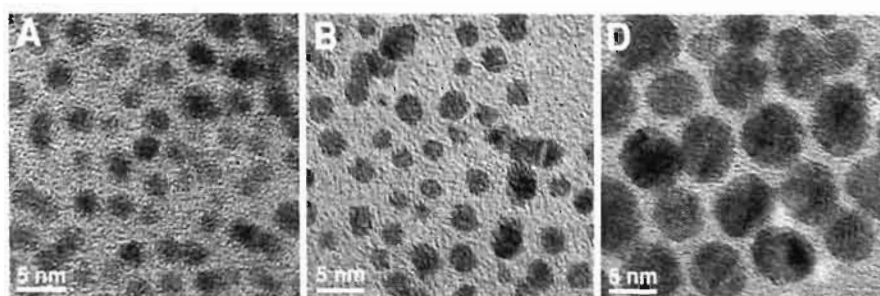

Figure 4.7. HRTEM images of (A) 1.8 nm, (B) 2.7 nm and (D) 5.7 nm $Au(S\text{-}EG_3)_x$. Samples were prepared by drop casting dilute solution on to a formvar coated copper grid.

Similarly, the morphology of Au nanorods was confirmed using HRTEM and the images are presented in Figure 4.8. The average length and aspect ratio of Au nanorods were estimated by analyzing ~80 nanorods (Figure 4.8).

4.3.3. Absorption Studies

The frequency of oscillation of metal nanoparticles is determined mainly by four parameters: density of the electron, effective mass of the electron and the shape and size distribution of the charge.[31] In the present case, the optical properties of Au nanomaterials (position and extinction coefficient of plasmon resonance band) were varied by tuning their size and shape. The surface plasmon absorption of **Au(S-EG$_3$)$_x$** with 4 different diameters are presented in Figure 4.9. Gold nanoparticles protected with triethylene glycol thiol, possess a characteristic surface plasmon absorption band centered at 520 nm.[30] The plasmon absorption in Au nanoparticles originates from the interaction of external electromagnetic radiation with the highly polarizable Au 5d^{10} electrons of gold atoms.[32,33] In the present case, a hypsochromic shift in the λ_{max} was observed from 520 nm to 515 nm on decreasing the diameter of the nanoparticle from 5.7 to 2.7 nm, whereas 1.8 nm Au nanoparticles does not show any characteristic peak.[34] It is well understood that Au nanoparticles of larger diameter absorbs at longer wavelength which is attributed to the electromagnetic retardation in larger nanoparticles.[6b] The sharp decrease in the intensity of surface plasmon band observed on decreasing the diameter (Figure 4.9A) may be attributed to the inset of quantum size effect.[35] The broadening and
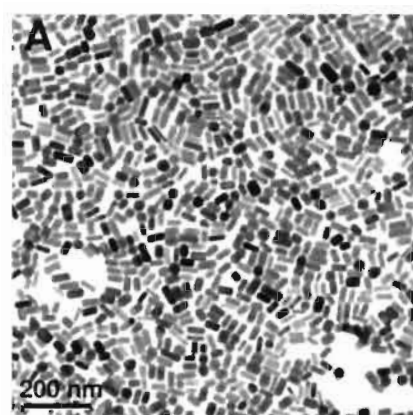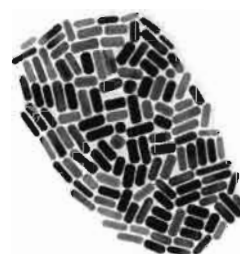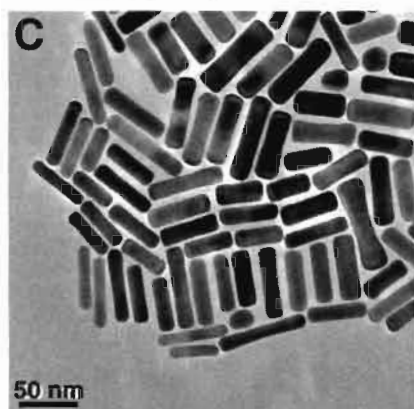
	A	B	
Av. length, nm (l)	= 42	Av. length, nm (l)	= 49
Av. width, nm (b)	= 19	Av. width, nm (b)	= 18
Av. aspect ratio (l/b)	= 2.2	Av. aspect ratio (l/b)	= 2.7
λ_{max}, nm (LSP)	= 625	λ_{max}, nm (LSP)	= 650
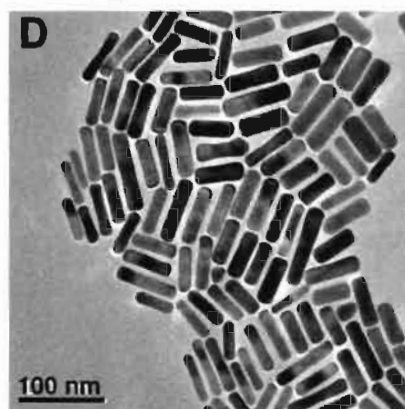
	C	D	
Av. length, nm (l)	= 52	Av. length, nm (l)	= 60
Av. width, nm (b)	= 17	Av. width, nm (b)	= 16
Av. aspect ratio (l/b)	= 3.0	Av. aspect ratio (l/b)	= 3.7
λ_{max}, nm (LSP)	= 700	λ_{max}, nm (LSP)	= 750

Figure 4.8. HRTEM images of Au nanorods having an average aspect ratio of (A) 2.2, (B) 2.7, (C) 3.0 and (D) 3.7. Samples were prepared by drop casting dilute solution on to a formvar coated copper grid.

dampening of surface plasmon bands with decrease in the size results from the surface scattering of conduction electrons which follows 1/radius.[1a]

Gold nanorods being anisotropic in structure, its interaction with electromagnetic radiation is inhomogeneous which results in the splitting of surface plasmon bands. Au nanorods possess two distinct surface plasmon absorption bands: one at around 520 nm and other at a longer wavelength depending on its aspect ratio (Figure 4.9B). The short wavelength band originates from the coherent oscillation of electrons along the short axis (transverse band) whereas, the longer wavelength band is more intense which results from the coherent electron oscillation along the longer axis of Au nanorods (longitudinal band). Electric field alignment studies by van der Zande *et al.* have unambiguously confirmed these aspects.[36] The longitudinal band undergoes a bathochromic shift with increase in the aspect ratio of nanorod as shown in Figure 4.9B. We have

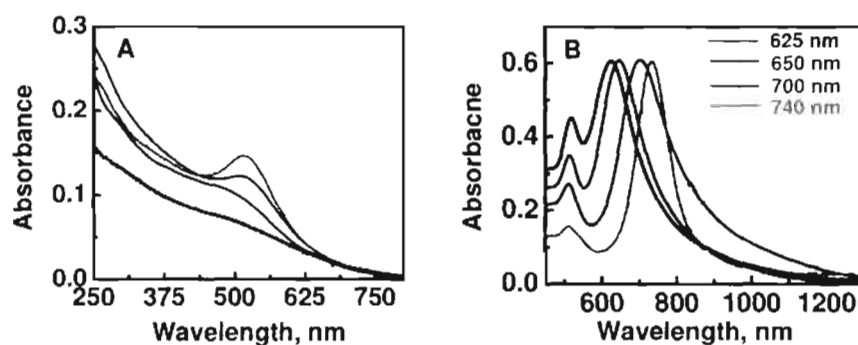**Figure 4.9.** (A) Absorption spectra of **Au(S-EG₃)ₓ** nanoparticles having an average diameter of 1.8 nm (black), 2.7 nm (blue), 4.5 nm (green) and 5.7 nm (red) in CH_3CN. (B) Normalized absorption spectra of Au nanorods having an average aspect ratio of 2.2 (black), 2.7 (blue), 3.0 (green) and 3.7 (red) in a mixture (1:4) of H_2O-CH_3CN.

have further investigated the stability of Au nanorods in various solvent systems and these aspects are presented below.

4.3.4. Stability of Au Nanorods

Stability of Au nanorods is an essential parameter for any physical measurement and was studied in mixtures of water and acetonitrile, by following their absorption spectrum as a function of time (Figure 4.10). The stability of nanorods was found to decrease with increase in the composition of acetonitrile. For example, Au nanorods of all aspect ratios were stable in water; however they readily precipitate in a mixture (1:4) of CH_3CN-H_2O. This is obvious from the absorption spectral profiles presented in Figure 4.10A. The spectral changes as a function of time, in mixtures of H_2O-CH_3CN, are presented in Figure 4.10B-E. More interestingly the stability of Au nanorods increased with further increase in the composition of acetonitrile and found to be stable in mixtures having more than 70% CH_3CN. Zeta potential (ζ) measurements were carried out to obtain a better insight on the unusual variations in the stability observed upon changing the solvent composition.

4.3.5. Zeta Potential Measurements

Deionized water was used for zeta potential measurements. In water, Au nanorods of all the four aspect ratios under investigation possess a positive ζ value.[37,38] Interestingly, the ζ values decreases with increase in the composition of acetonitrile and approaches zero in a mixture (1:4) of CH_3CN-H_2O. A representative zeta potential plot of Au
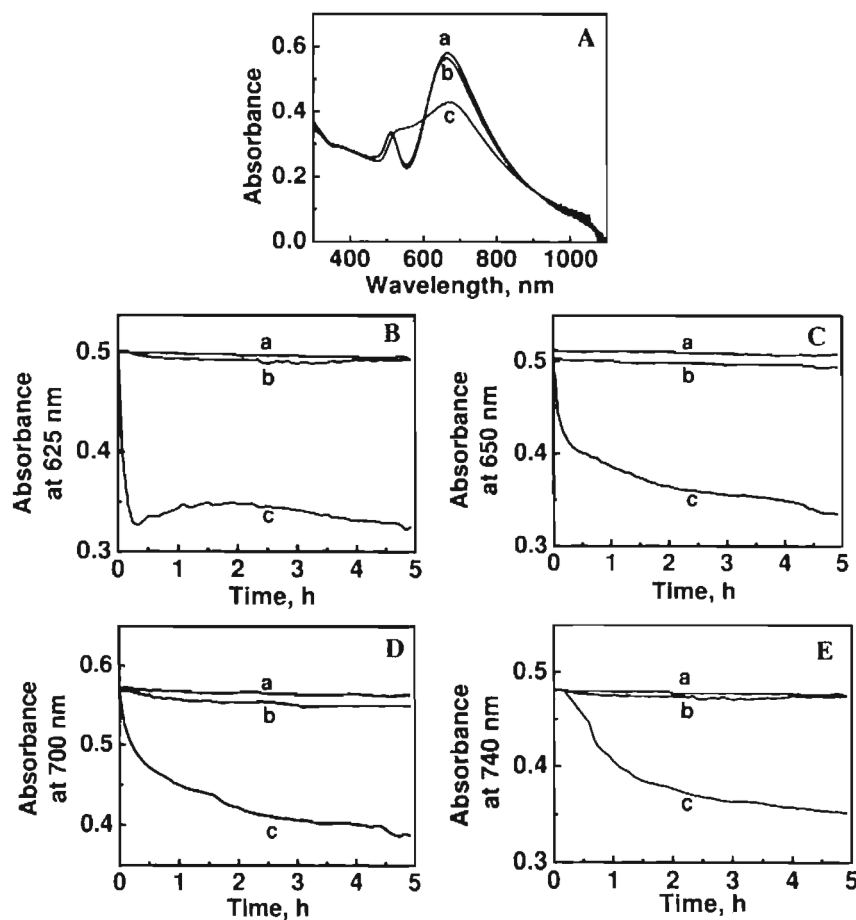
Figure 4.10. (A) Absorption spectra of Au nanorods having an average aspect ratio of 2.7 in different solvent mixtures: (a) H_2O, (b) (1:4) H_2O-CH_3CN and (c) (1:4) CH_3CN-H_2O. (B-E) Absorption-time changes in the longitudinal absorption band of Au nanorods [0.12 nM] of aspect ratio (B) 2.2, (C) 2.7, (D) 3.0 and (E) 3.7 in above mentioned solvent systems (a-c).

nanorods (aspect ratio of 2.7) in mixtures of water and acetonitrile are presented in Figure 4.11. It is interesting to note that the nanorods attain a negative ζ value on increasing the composition of acetonitrile, with an increase in its magnitude.
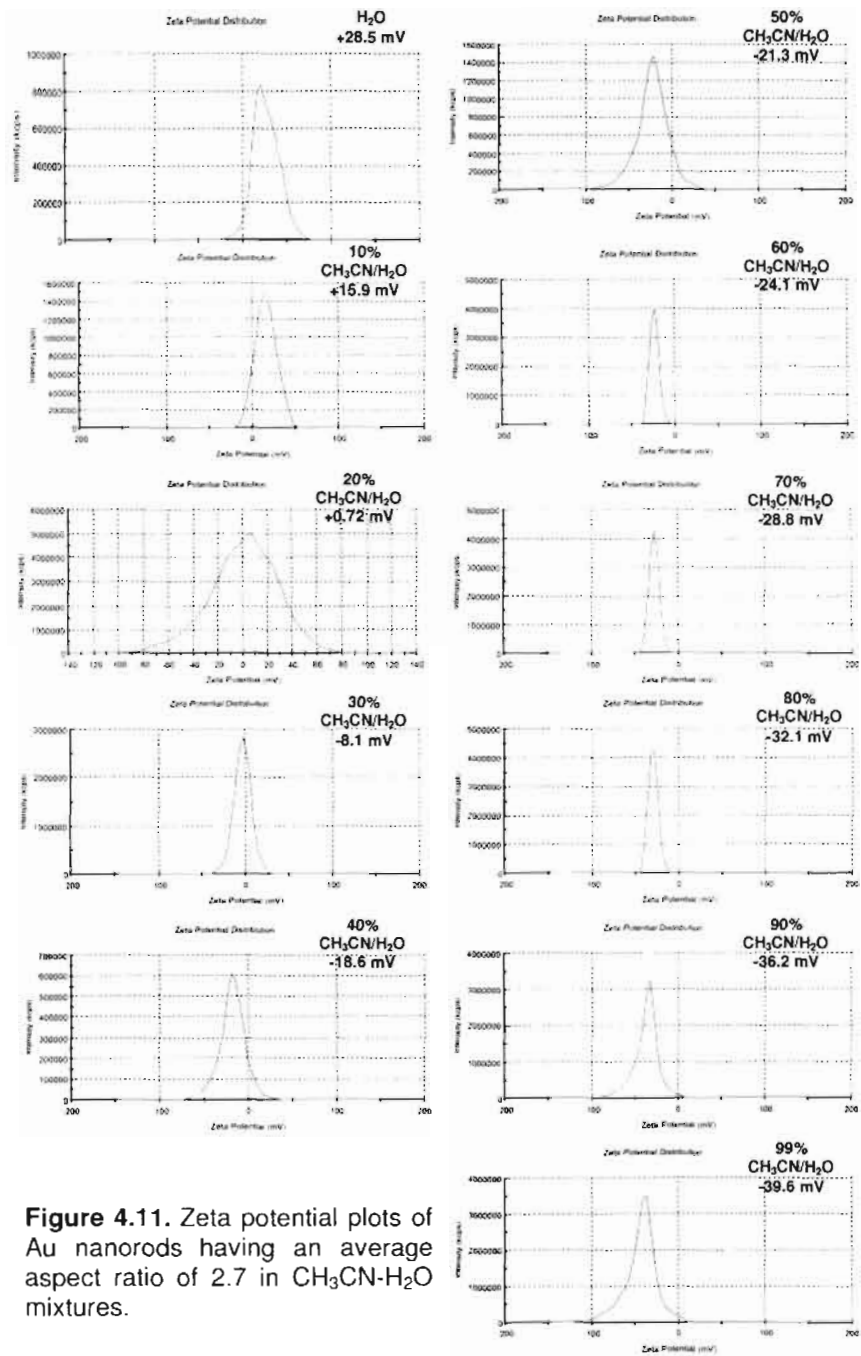
Figure 4.11. Zeta potential plots of Au nanorods having an average aspect ratio of 2.7 in CH_3CN-H_2O mixtures.
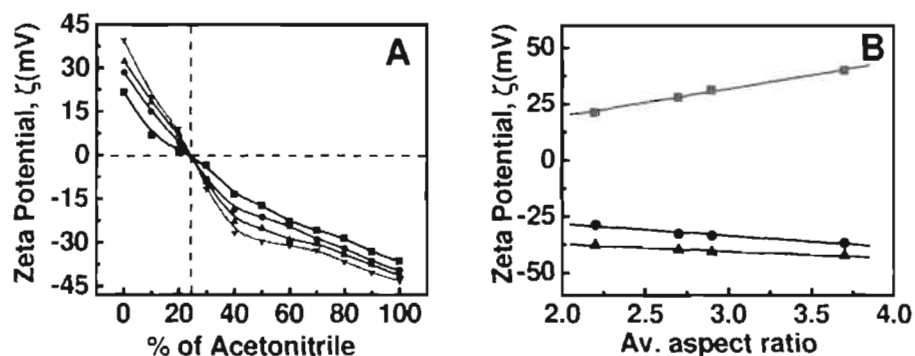
Figure 4.12. (A) Variation of zeta potential of Au nanorods (A) in H_2O-CH_3CN mixtures having an average aspect ratio of 2.2 (■), 2.7 (●), 3.0 (▲), 3.7 (▼) and (B) as a function of aspect ratio in various solvent mixtures: H_2O (■), (1:4) H_2O-CH_3CN (●) and (1:99) H_2O-CH_3CN (▲).

A sigmoidal plot was observed in all the cases, when the ζ values were plotted as a function of solvent composition (Figure 4.12A). Two conclusions can be derived from these sigmoidal plots: (i) ζ increases with increase in aspect ratio and (ii) positive ζ of nanorods first decreases with increase in CH_3CN composition and crosses through zero value to higher negative values (Figure 4.12A). Zeta potential of Au nanorods in (i) water, (ii) mixture (1:4) of H_2O-CH_3CN and (iii) mixture (1:99) of H_2O-CH_3CN are found to increase linearly with aspect ratio (Figure 4.12B).

Thus, the stability of Au nanorods in H_2O and CH_3CN rich solvents may be attributed to the large positive and negative ζ values. As the magnitude of zeta potential increases, the nanoparticle experiences interparticle repulsion and remain isolated in solution; higher the magnitude of zeta potential, greater the stability of nanoparticle system. From these results, it is also clear that the nanorods with larger aspect

ratios are more stable than short aspect ratios due to increase in surface charges. It is earlier proposed that, Au nanorods in water are covered by a bilayer[22,37,38] of CTAB molecules ('A' in Scheme 4.5). The excess positive charge originates from the polar head groups of CTAB molecules and the ζ value increases with aspect ratio. With increase in the composition of organic solvent, the bilayer structure collapse to monolayer resulting in the loss of CTAB from the surface of Au nanorods and a decrease in ζ was observed.[37,38] In a mixture (1:4) of CH_3CN-H_2O, the negative surface charge on Au nanorods may be completely neutralized by the CTAB molecules and ζ approaches zero ('B' in Scheme 4.5). Interestingly, a charge reversal from positive to negative ζ was observed with further increase in CH_3CN content. In acetonitrile rich solvents, the number of CTAB molecules protecting the Au nanorods may be much lower compared to that in a mixture (1:4) of CH_3CN-H_2O medium, resulting in a high negative zeta potential ('C' in Scheme 4.5).
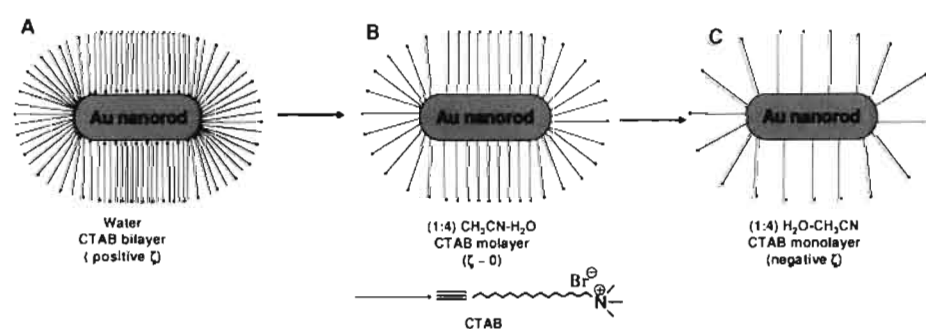
Scheme 4.5: Schematic representation of charge reversal in Au nanorods as a function of solvent composition.

The zeta potential of **Au(S-EG₃)ₓ** were investigated as a function of size and solvent composition. Interestingly, the ζ values varied linearly with particle size (+10 to +36 mV)[30] due to the increase in their surface charge density; however, the solvent composition (CH_3CN-H_2O mixtures) has only little effect. In the case of **Au(S-EG₃)ₓ** hybrid systems, monolayers are covalently bound to gold nanoparticles and hence not influenced by solvent composition changes. The zeta potential plots of **Au(S-EG₃)ₓ** of varying size, in a mixture (1:4) of H_2O-CH_3CN, is shown in Figure 4.13. Interestingly the ζ values varied linearly with particle size and the plot of zeta potential value against particle diameter is shown in the Figure 4.14A.
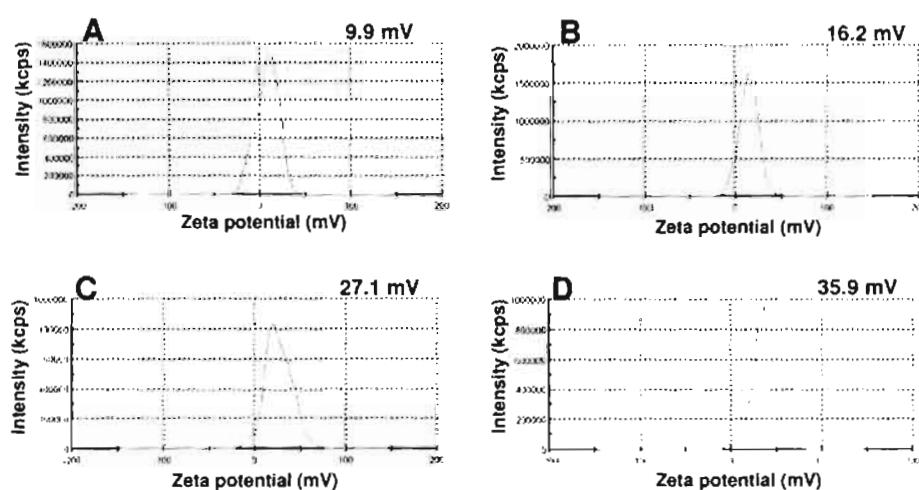

Figure 4.13. Zeta potential plots of **Au(S-EG₃)ₓ** nanoparticles having an average diameter of (A) 1.8 nm, (B) 2.7 nm, (C) 4.5 nm and (D) 5.7 nm in a mixture (1:4) of H_2O-CH_3CN.

4.3.6. Au Nanorod-Au Nanoparticle Interaction

As discussed in Section 4.2, theoretically it is proposed that the electric field at the edges of Au nanorods are very high compared to lateral faces.[15,16] In order to experimentally verify these aspects, we have studied the interaction between positively charged Au nanoparticles and negatively charged Au nanorods. From the zeta potential studies presented in the Section 4.3.5, it is clear that **Au(S-EG$_3$)$_x$** possess positive zeta potential whose magnitude increases with size (trace 'b' in Figure 4.14A) and is independent of solvent polarity. In a mixture (1:4) of H$_2$O-CH$_3$CN, Au nanorods possess negative zeta potential and its magnitude increases with aspect ratio (trace 'b' in Figure 4.14A). In order to investigate the edge effect in Au nanorods, we have studied the electrostatic interaction between the positively charged Au nanoparticles and negatively charged Au nanorods. Two possibilities exists depending on the distribution of charges on the surface of Au nanorods; if the charges are distributed uniformly on the rods, the binding may be uniform (Scheme 4.6A) whereas, if it is concentrated at the edges, assembly may result in the accumulation of nanoparticles at the edges as shown in Scheme 4.6B.
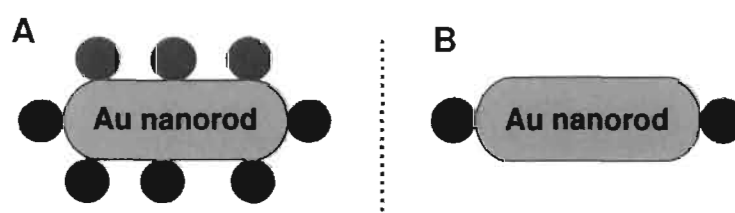
Scheme 4.6: Two possible electrostatic interactions between Au nanorods and nanoparticles.

The interaction between Au nanorods and Au nanoparticles was investigated by following the UV-visible spectroscopic changes and HRTEM analysis. Microlitre quantities of 1.8 nm sized Au nanoparticles (0-10 nM) were added to Au nanorods in a mixture (1:4) of H_2O-CH_3CN and the absorption spectral changes were monitored. Interestingly, a spontaneous bathochromic shift in the longitudinal plasmon band of Au nanorods was observed on addition of Au nanoparticles; however, the position of the transverse plasmon band remained unaffected. The enhanced intensity of the transverse band around 520 nm is due to the presence of excess nanoparticles in the solution, which absorbs in the same spectral region (Figure 4.14B). A bathochromic shift of ~60 nm was observed on the addition of 10 nM of Au nanoparticles (1.8 nm) to Au nanorods (average aspect ratio 3.7; Figure 4.14B).

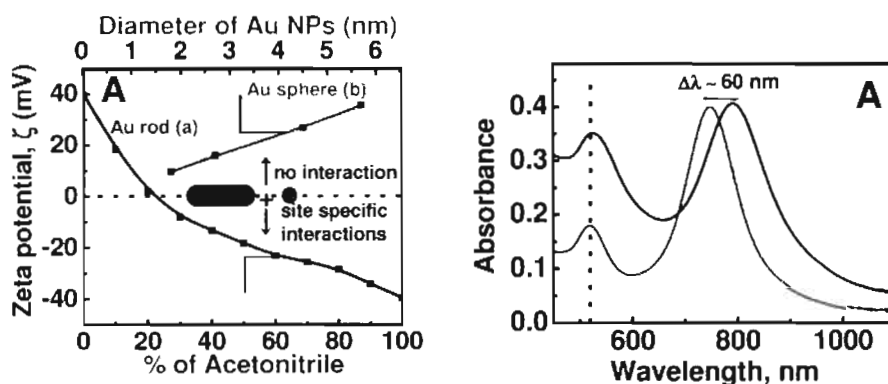**Figure 4.14.** (A) Variation of ζ of (blue) Au nanorods (average aspect ratio of 3.7) at different compositions of CH_3CN-H_2O and (red) Au nanoparticles in a mixture (1:4) of H_2O-CH_3CN as a function of diameter. (B) Absorption spectral changes of Au nanorods (average aspect ratio of 3.7) in a mixture (1:4) of H_2O-CH_3CN on addition of 0 nM (blue) and 10 nM (red) 1.8 nm Au nanoparticles.

HRTEM studies were carried out to obtain better insight on the mechanism of the spectral shift observed. HRTEM images of Au nanorods recorded both in the absence and presence of Au nanoparticles, under identical conditions, are presented in Figure 4.15. Nanorods remain isolated and randomly distributed in the absence of nanoparticles. A preferential close packing of Au nanoparticles on the edges of Au nanorods was observed in the presence of Au nanoparticles. The preferential assembly of particles at the edges causes a change in the frequency of longitudinal plasmon oscillation resulting in the bathochromic shift in the longitudinal band.
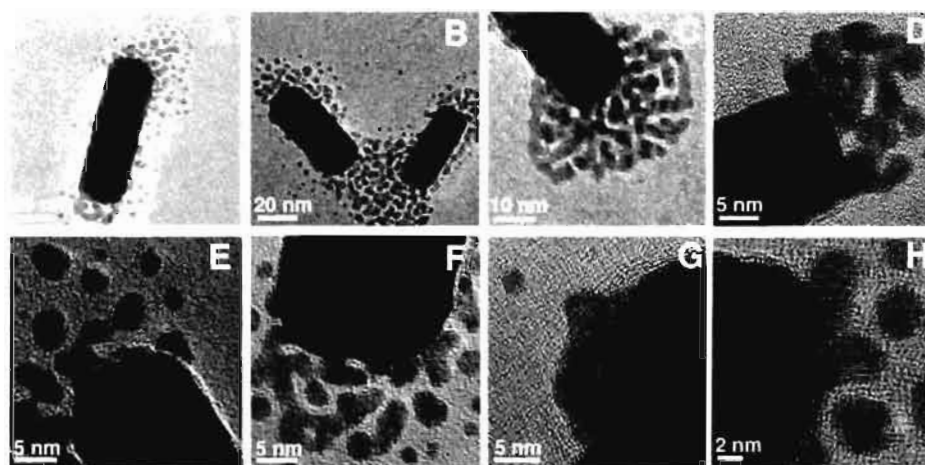
Figure 4.15. (A-H) HRTEM images of Au nanorods (average aspect ratio of 3.7) recorded in the presence of Au nanoparticles (diameter, 1.8 nm) from different locations of the grid. Samples were prepared by drop casting dilute solution on to a formvar coated copper grid.

Further, the interaction of Au nanorods (aspect ratio 3.7) with Au nanoparticles of varying diameters (2.7, 4.5 and 5.7 nm) were investigated. Addition of 2.7 nm sized Au nanoparticles resulted in a bathochromic shift

of ~35 nm in the longitudinal plasmon band whereas, 4.5 nm sized nanoparticles resulted in ~10 nm shift (Figure 4.16A&B). Interestingly, no spectral shifts were observed on addition of 5.7 nm sized Au nanoparticles (Figure 4.16C). To obtain more insight, we have further investigated the
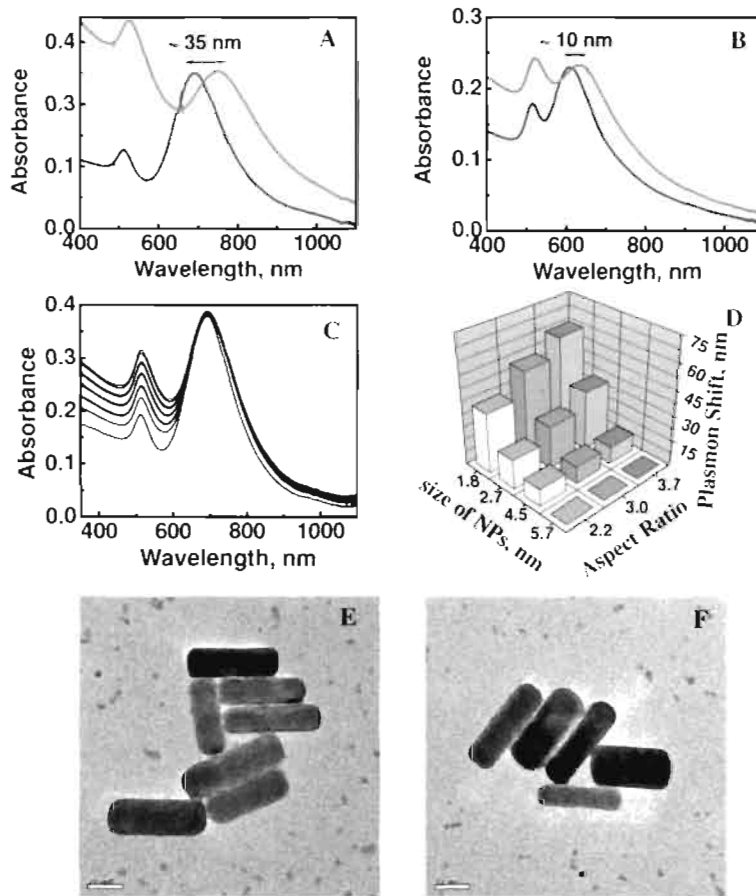
Figure 4.16. Absorption spectral changes of Au nanorods of (average aspect ratio of 3.7) in a mixture (1:4) of H_2O-CH_3CN on addition of 0 nM (blue) and 10 nM (red) Au nanoparticles of varying sizes (A) 2.7 nm, (B) 4.5 nm and (C) 5.7 nm. (D) 3D plot showing longitudinal plasmon shift of Au nanorods of different aspect ratio on addition of Au nanoparticles of varying diameters. (E,F) HRTEM images of Au nanorods on addition of 5.7 nm Au nanoparticles.

interaction of Au nanorods having an average aspect ratio of 2.2 and 3.0 with Au nanoparticles of varying diameters. Similar absorption changes were obtained indicating a dependency of nanoparticles' size on the relative shift in the longitudinal plasmon absorption band. The variation of plasmon shift as a function of Au nanoparticle size and Au nanorod aspect ratio is presented in the 3D plot showed in Figure 4.16D. It is clear from the 3D plot that the bathochromic shift in the longitudinal plasmon band ($\Delta\lambda$) is more pronounced for nanoparticles having smaller diameters, irrespective of the aspect ratio of Au nanorods. It is surprising to note that no spectral shifts were observed on addition of 5.7 nm sized nanoparticles to Au nanorods (Figure 4.16C).

In order to obtain quantitative information on the spectral shift, we have estimated the maximum number of nanoparticles that can be accommodated at the edge of nanorods as a function of their size (based on a close-packing model, the approximate numbers for 1.8, 2.7, 4.5, and 5.7 nm nanoparticles calculated were 350, 145, 75, and 30, respectively). The interparticle repulsion between the nanoparticles is much lower in the case of 1.8 nm nanoparticles (+10 ± 0.5 mV), and nanorods can accommodate relatively more nanoparticles at the edges due to their smaller size, resulting in a larger plasmon shift. In contrast, the enhanced interparticle repulsion experienced by 5.7 nm sized nanoparticles (ζ of +36 ± 0.5 mV) prevents them from binding on to the edges (Figure 4.16E,F).

Further, all the above experiments were carried out in water wherein both nanorods and nanoparticles possess positive ζ values and no

spectral changes were observed. This clearly indicates that the spontaneous plasmon shift observed in mixture (1:4) of H_2O-CH_3CN is exclusively due to the electrostatic attractive interaction between positively charged Au nanoparticles and negatively charged Au nanorods.

The shift in the longitudinal plasmon absorption band can result either through an interplasmon coupling or a preferential binding of Au nanoparticles at the edges of Au nanorods. It has been recently reported that the interplasmon coupling in Au nanorods results in a gradual decrease in the longitudinal plasmon absorption along with concomitant formation of a new red-shifted band through a clear isosbestic point. In the present case, a spontaneous red-shift in the longitudinal plasmon band was observed and the mechanism involving the interplasmon coupling was ruled out. In an earlier report, Gluodenis and Foss[10] have theoretically proposed a red-shift in the longitudinal plasmon band of Au nanorods when nanoparticles approach in an end-to-end fashion. In the present case, the bathochromic shift in the longitudinal plasmon band is attributed to the selective binding of nanoparticles on to the edges of Au nanorods, leading to their preferential growth in the longitudinal direction. The obvious question is why do the nanoparticles preferentially bind on to the edges of Au nanorods? As discussed in Section 4.2.1., the electric field in Au nanorods is more concentrated at the edges than the lateral face. In the present case nanorods have negative ζ values (in 1:4 H_2O-CH_3CN), and the enhanced potential at their edges preferentially attracts the positively charged nanoparticles, leading to the selective growth of Au nanorods in the longitudinal direction (Scheme 4.7).
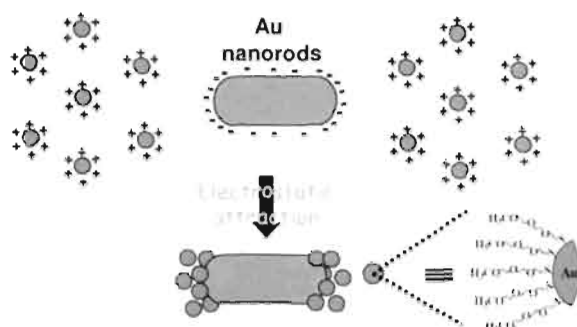
Scheme 4.7. Preferential end functionalization of Au nanorods with nanoparticles through electrostatic interaction.

Similar spectral changes were observed with octylmercaptan protected Au nanoparticles; however, the stability of the hybrid system was much lower compared to that of the ethylene glycol protected Au nanoparticles. Assembly based on octylmercaptan-capped Au nanoparticles precipitated in 15 min whereas, the assembly based on **Au(S-EG$_3$)$_x$** nanoparticles was found to be stable for more than 3 h (slow precipitation was observed at longer periods). The polar ethylene glycol moieties present on the surface of Au nanoparticles stabilize these hybrid nanostructures in polar solvent compared to the alkyl groups.

The possibility of functionalizing chromophores selectively on to the edges of Au nanorods was investigated by adding ruthenium trisbipyridine (**Ru(bpy)$_3$$^{2+}$**) capped Au nanoparticles (Figure 4.17). As in the earlier case, a spontaneous red shift in the longitudinal plasmon band was observed with no shift in the transverse plasmon band. The corresponding emission spectrum of **Ru(bpy)$_3$$^{2+}$** functionalized hybrid system is presented in the inset of Figure 4.17B.
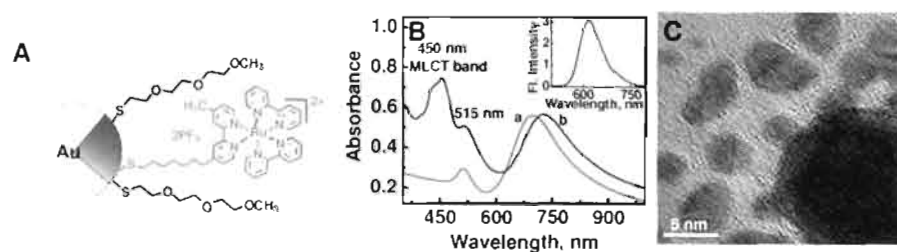
Figure 4.17. (A) Chemical structure of **Au-Ru²⁺**, (B) absorption spectral changes of Au nanorods on addition of **Au-Ru²⁺** nanoparticles (diameter, 4.5 nm) in a mixture (1:4) of H_2O-CH_3CN: (a) 0 nM and (b) 10 nM (the inset shows the corresponding luminescence spectrum) and (C) the corresponding HRTEM image.

4.3.7. Dimers of Au Nanorods and Plasmon Coupling

As mentioned in Section 4.2.1., plasmon coupling in Au nanorods was experimentally verified by integrating them into 1D assembly through supramolecular and covalent approaches.[4] As the number of Au nanorods in a chain increases, several possible orientations exist between the nanorods in a chain. Such variations in orientation between the nanorods in a nanochain can influence the effective plasmon coupling and hence difficult to quantify. Plasmon coupling mainly depends on the interparticle distance and the orientation between Au nanorods. hence more conclusive results can be obtained from studies based on their dimers. Recently El-Sayed and coworkers have theoretically proposed that the orientation between the nanorods play a decisive role in plasmon coupling.[64] The authors have calculated the discrete dipole approximation (DDA) simulated extinction efficiency spectra of Au nanorod dimers as a function of the orientation between the long axes of the nanorods. As the orientation between the Au nanorods increases, the longitudinal plasmon band shifts

to lower energy region confirming the role of effective dipolar overlap in plasmon coupling.[6a] In order to experimentally verify the role of orientation on plasmon coupling, we have selected an aromatic dithiol namely 1,2 phenylenedimethanethiol (**PDT**), which is more or less rigid in nature, and these results were compared with aliphatic dithiol, namely 1,6 hexanedithiol (**C₆DT**). Aliphatic dithiols are flexible in nature and hence prefers a folded conformation in polar solvents, which can influence the plasmon coupling due to the mismatch in the polarization axes of nanorods. Solvent systems rich in acetonitrile are ideal for the synthesis of dimers due to the higher stability of nanorods and the better solubility of the linker groups. In the present case, we have selected a mixture (1:4) of H_2O-CH_3CN for interplasmon coupling studies.

Au nanorods [0.12 nM] having an average aspect ratio of ~2.7 were used for the dimerization studies and oligomerization process was controlled by decreasing the concentration of α,ω-dithiols to 0.8 µM. Upon addition of **C₆DT/PDT**, a gradual decrease in the longitudinal plasmon band with a concomitant formation of a new red shifted band was observed through an isosbestic point (Figures 4.18A and 4.19A). In order to confirm the dimer formation, TEM studies were carried out by drop casting nanorod solutions onto a formvar coated copper grid. In the presence of dithiols, Au nanorods were found to be predominantly as dimers and evenly distributed in various locations of the grid. Representative TEM images of dimers having **PDT** and **C₆DT** as linkers are shown in Figures 4.18 and 4.19, respectively. Thus based on the TEM and absorption spectral studies, the
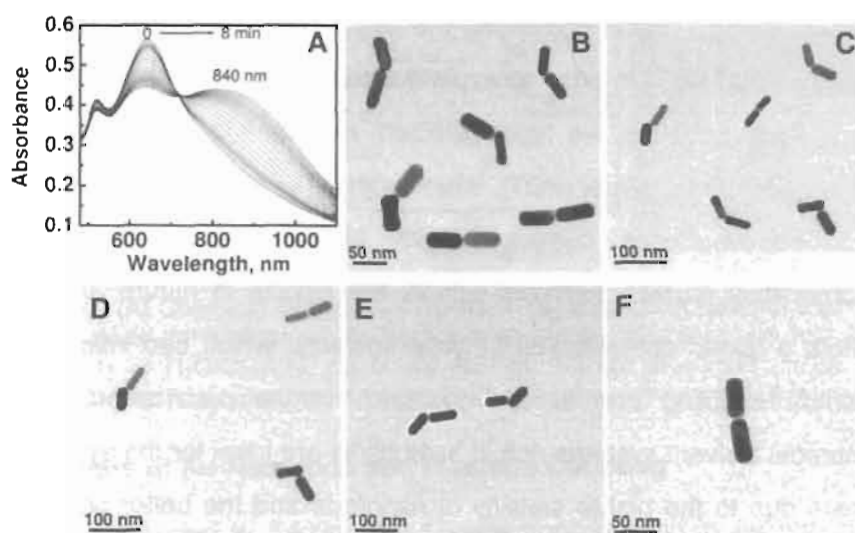
Figure 4.18. (A) Absorption spectral changes of Au nanorods [0.12 nM] having an average aspect ratio of 2.7 on addition of [0.8 µM] of **PDT** in a mixture (1:4) of H_2O-CH_3CN and (B-F) the corresponding TEM images of Au nanorod dimers linked using **PDT** (8 min after the addition of **PDT**, a dilute solution was drop casted on to a formvar coated copper grid).

newly formed band is assigned as the coupled plasmon band of Au nanorod dimers. Deviations from the isosbestic point and shift in λ_{max} observed at longer time durations, particularly at higher concentrations of linker molecules, may be due to the formation of oligomers of Au nanorods (*vide infra*).

Interestingly the angle between the nanorod dimers is different when **C₆DT** and **PDT** were used as linkers: 92° in the case of **C₆DT** and 146° in the case of **PDT** (averaged for 20 dimers). From TEM images it is clear that the **PDT** linked Au nanorod dimers are more linear due to the rigidity induced by the aromatic dithiols. We believe that the **PDT** linked Au nanorod dimers may be more linear in solution than what we observe in
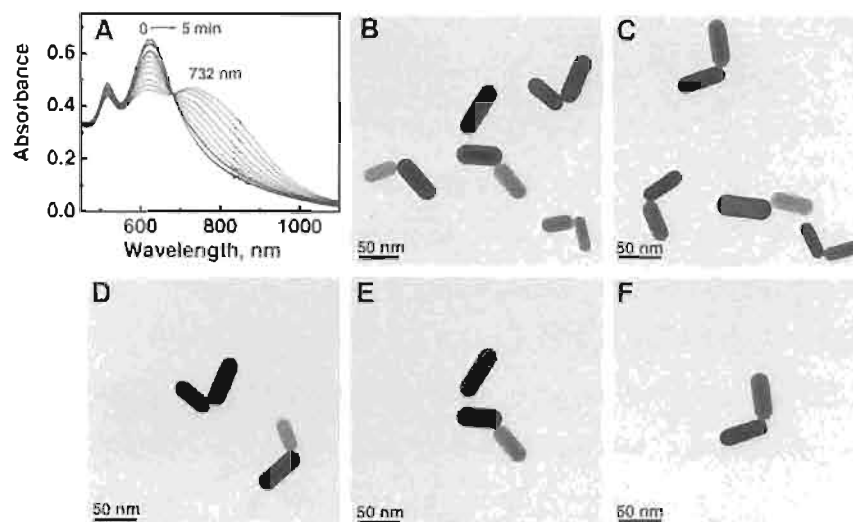
Figure 4.19. (A) Absorption spectral changes of Au nanorods [0.12 nM] having an average aspect ratio of 2.7 on addition of [0.8 μM] of C_6DT in a mixture (1.4) of H_2O-CH_3CN and (B-F) the corresponding TEM images of Au nanorod dimers linked using C_6DT (5 min after the addition of C_6DT. dilute solution was drop casted on to a formvar coated copper grid).

TEM images and the deviation observed may be due to the changes occurring during the solvent evaporation. Theoretically it has been proposed that the plasmon coupling is more effective when the polarization axes of two nanorods are linear with the light polarization axis.[6a] Thus the plasmon coupling in **PDT** linked Au nanorod dimers should be more effective compared to C_6DT (Scheme 4.8). This is very clear from the absorption spectral features of **PDT**/C_6DT linked Au nanorods: the λ_{max} of **PDT** and C_6DT linked Au nanorod dimers were observed at 840 nm and 732 nm, respectively (Figures 4.18A and 4.19A). The λ_{max} of the dimers of Au nanorods (aspect ratio 2.7) linked using 1,5-pentanedithiol (C_5DT),
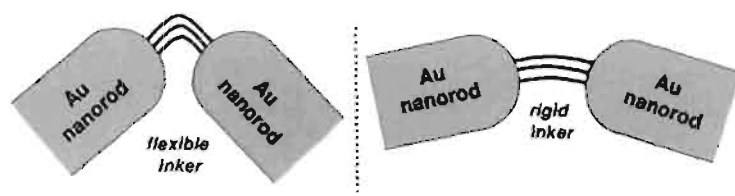
Scheme 4.8. Orientation of dimers of Au nanorods possessing flexible and rigid linkers

1,8-octanedithiol (**C₈DT**) and 1,9-nonanedithiol (**C₉DT**) were observed at 733 nm, 732 nm and 722 nm, respectively (Figure 4.20) The aliphatic dithiols discussed above may form a folded geometry in polar solvents and hence the λ_{max} of Au nanorod dimers are observed at around same region The large red shift of ~110 nm, observed in the case of **PDT** linked Au nanorod dimers compared to that of aliphatic dithiols may be attributed to the effective plasmon coupling
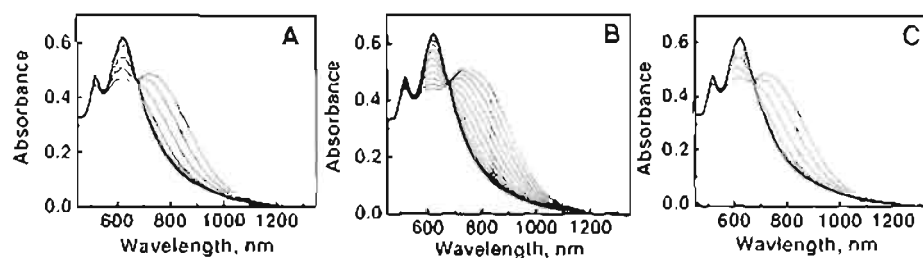
Figure 4.20. Absorption spectral changes of Au nanorods [~0.12 nM] of average aspect ratio 2.7 upon the addition of α,ω dithiols [0 8 μM] at time intervals from 0-10 min in a mixture (1:4) of H₂O-CH₃CN: (A) C₉DT, (B) C₈DT and (C) C₅DT.

Another interesting point of discussion is the mechanism of dimer formation. It has been earlier reported that the edges of Au nanorods are not thickly packed with thiol groups in the incubation step.[24c] Above the critical concentration, Au nanorods interlock to form dimers as shown in

Scheme 4.9 (type I). However, another possibility of dimerization through the disulfide formation also exists as shown in Scheme 4.9 (type II). TEM studies indicated that the average distance between the Au nanorods is less than 1 nm which is in close agreement with the molecular length of PDT (0.83 nm). Presence of oxygen can lead to disulfide formation and experiments carried out in argon saturated solution showed similar absorption spectral changes as presented in Figure 4.21A. Thus, based on TEM and absorption spectral studies, the disulfide formation was ruled out confirming that the dimer formation proceeds through an interlocking mechanism.
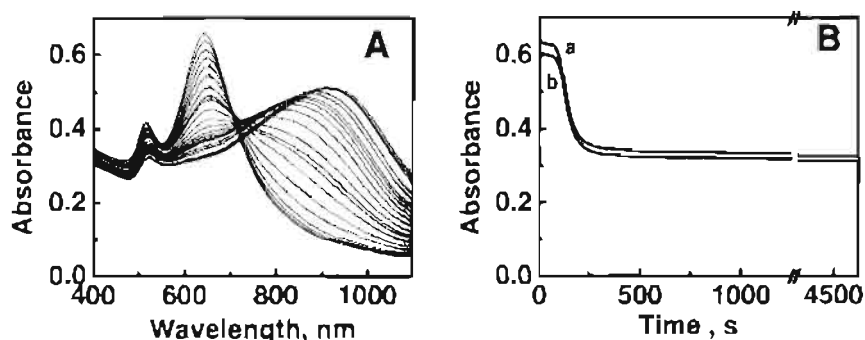
Figure 4.21. (A) Absorption spectral changes of Au nanorods [~0.12 nM] of average aspect ratio 2.7 in argon saturated solution of a mixture (1:4) of H_2O-CH_3CN, upon the addition of PDT [2 μM] at time intervals from 0-20 min and (B) Absorption-time changes in the longitudinal absorption band of Au nanorods [~0.12 nM] upon the addition of (a) **PDT** and (b)C$_6$DT.

We have further investigated the plasmon coupling by increasing the concentration of linker molecules to 2 μM. Absorption spectral changes were more rapid and the newly formed band shifts to longer wavelength with time. The absorption spectral changes on addition of PDT and C$_6$DT
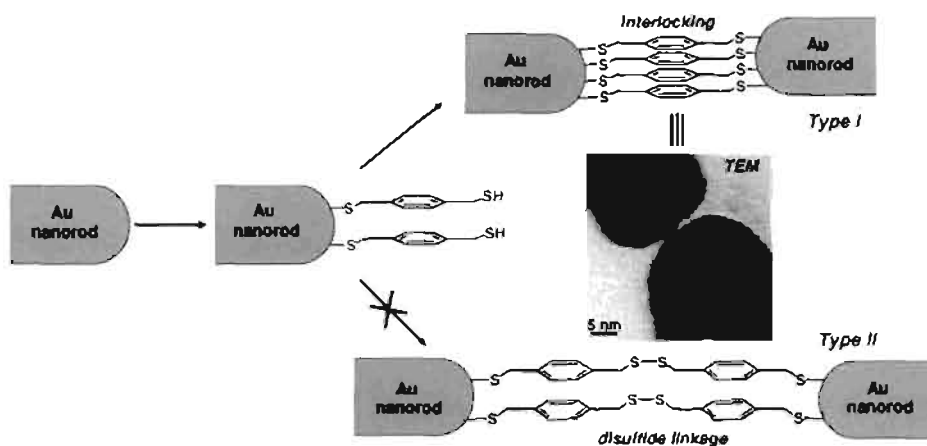
Scheme 4.9. Two possible mechanisms leading to plasmon coupling in Au nanorods.

are presented in Figures 4.22A and 4.23A.Time dependant changes of the longitudinal absorption of Au nanorods at 650 nm were followed in the presence of PDT/C_6DT (Figure 4.21B). A sigmoidal plot was observed in both the cases and the oligomerization process was found to be over in ~20 min. Further, no spectral shifts were observed for several hours indicating that the Au nanochains are stable under the experimental condition. TEM images of Au nanochains obtained by drop casting the solution on to a formvar coated copper grid (after 20 min of addition of dithiols), are presented as Figures 4.22 and 4.23.

The stability of Au nanorods at the incubation, dimerization and oligomerization steps was investigated by measuring the zeta potential. During the incubation period, the ζ decreases from -32.1 mV to -26.4 mV, which further drops to -8.1 mV at the end of oligomerization step. The ζ of Au nanorod dimers was found to be -18.6 mV under controlled conditions

Figure 4.22. (A) Absorption spectral changes of Au nanorods [0.12 nM] having an average aspect ratio of 2.7 on addition of 2 µM of **PDT** in a mixture (1:4) of H$_2$O·CH$_3$CN and (B-F) the corresponding TEM images of Au nanochains using **PDT** as the linker (20 min after the addition of **PDT**, dilute solution was drop casted on to a formvar coated copper grid).

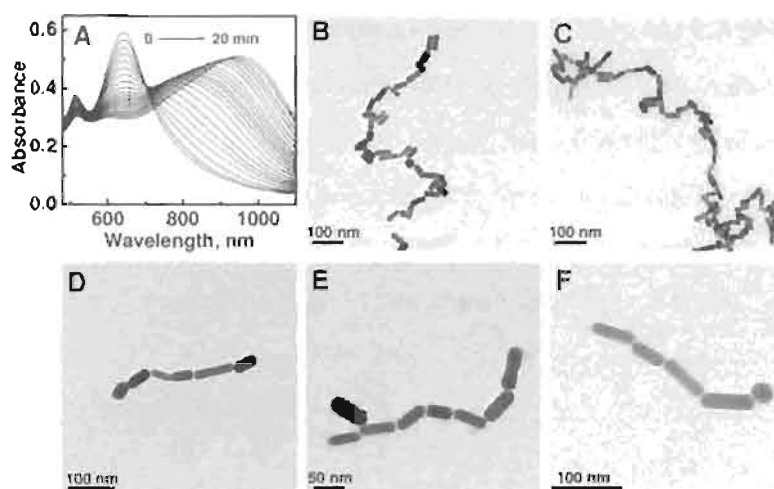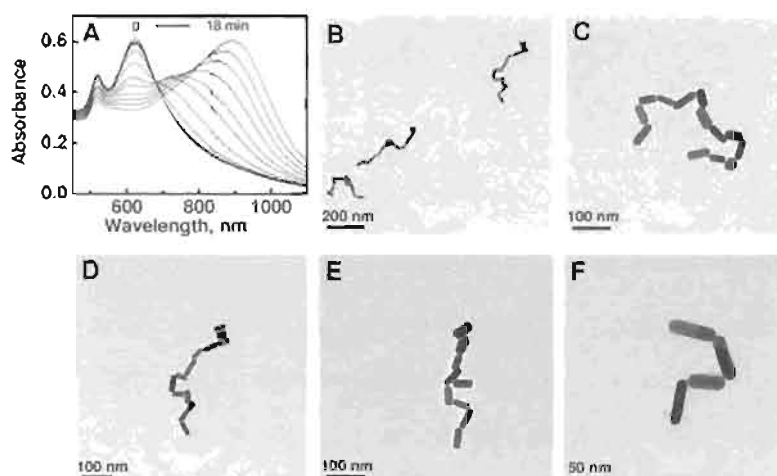**Figure 4.23.** (A) Absorption spectral changes of Au nanorods (0.12 nM) having an average aspect ratio of 2.7 on addition of 2 µM of **C$_6$DT** in a mixture (1:4) of H$_2$O·CH$_3$CN and (B-F) the corresponding TEM images of Au nanochains using **C$_6$DT** as the linker (20 min after the addition of **C$_6$DT**, dilute solution was drop casted on to a formvar coated copper grid).

by adding 0.8 µM of **PDT**. The zeta potential distribution of Au nanorods in the absence and presence of PDT are presented in Figure 4.24. The ζ distribution is narrow for Au nanorods, which broadens with increase in concentration of **PDT** indicating the presence of oligomers of various chain lengths at the end of the reaction.
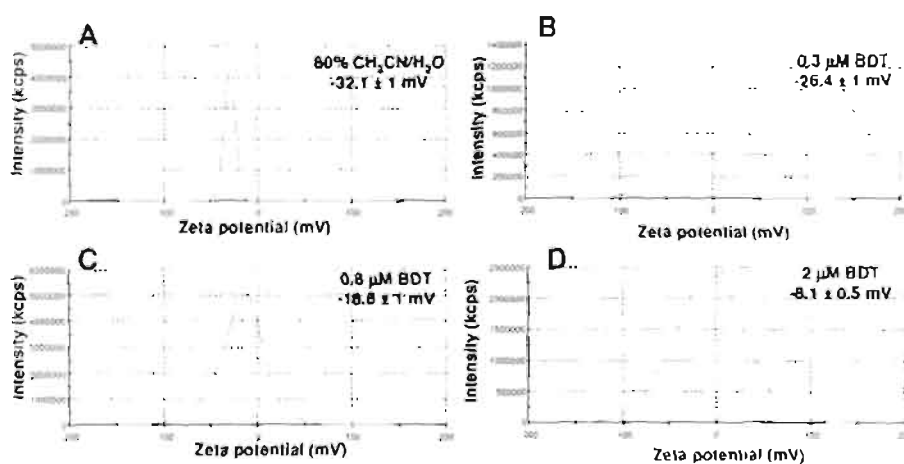
Figure 4.24. Zeta potential plots for 2.7 aspect ratio Au nanorods in a mixture (1:4) of H_2O-CH_3CN upon addition of different concentrations of PDT: (A) 0 (B) 0.3, (C) 0.8 and (D) 2.0 µM.

4.3.8. Disassembly of Au Nanochains

Place exchange or ligand exchange reactions on Au nanoparticles have been extensively utilized for designing hybrid nanomaterials.[39,40] In the present study, we have investigated the stability of Au nanochains by varying the temperature and in the presence of excess Au nanorods and alkyl thiols (for e.g., 1-pentyl mercaptan). Nanochains were prepared by adding 2 µM of **PDT** to nanorods as discussed earlier (Figure 4.22A). To

this solution, varying concentrations of Au nanorods (0.0-0.3 nM) were added. Nanochains possess a broad absorption band in the near infra-red region, which became narrow (decrease in the full width half maximum) and underwent a gradual blue shift on successive additions of Au nanorods (Figure 4.25A). The normalized absorption spectrum of the resultant band, on addition of ~0.3 nM of Au nanorods, matches well with that of isolated nanorods indicating the disruption of nanochains which was confirmed through TEM studies (Figure 4.25B). These results indicate that the dithiol molecules in Au nanochains undergo ligand exchange with the

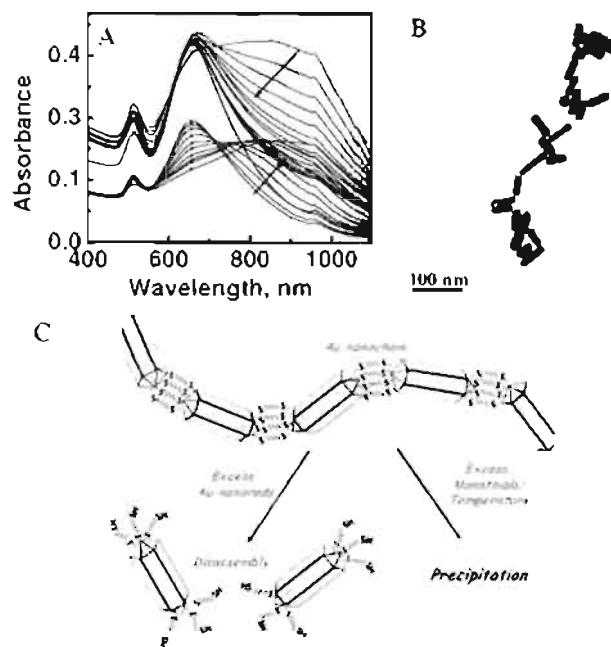Figure 4.25. (A) Absorption spectral changes of Au nanorods on addition of PDT (2 μM) illustrating the longitudinal plasmon coupling and the corresponding spectral changes (normalized) on addition of Au nanorods (0 nM to 0 3 nM), (B) TEM images after the addition of 0.3 nM of Au nanorods and (C) schematic representation of the disassembly of Au nanochains

added Au nanorods leading to the breakage of nanochains. Addition of excess 1-pentyl mercaptan as well as the increase in temperature resulted in the precipitation of nanochains (Figure 4.25C).

4.4. Conclusions

Two fundamental properties observed at the edges of Au nanorods, namely high electric field and reactivity were effectively utilized for hierarchical integration of Au nanorods. The stability of Au nanorods in water and water-acetonitrile mixtures, containing more that 70% acetonitrile, is attributed to the large positive and negative ζ which varied linearly with increase in aspect ratio. The high electric field observed at the edges of Au nanorods was experimentally verified by assembling oppositely charged Au nanoparticles and further extended for the site specific functionalization of molecules. Site specific functionalization methodology presented here may have potential application in the nanoscale fabrication of optoelectronic devices. Similarly Au nanorod dimers linked through a flexible (C_6DT) and rigid (PDT) linker groups were prepared and the plasmon coupling in these systems was investigated as a function of their orientation. The plasmon coupling in **PDT** linked Au nanorod dimers is found to be more pronounced due to effective dipolar overlap along their long axes. Thus, it is concluded that the orientation between the nanorods plays a crucial role in plasmon coupling which can be modulated by varying the nature of the linker group.

4.5. Experimental Section

4.5.1. Materials and Instrumental Techniques

Solvents and reagents used were purified and dried by standard methods. Photophysical studies were carried out using spectroscopic grade solvents. The zeta potential values were measured in a zetasizer Nanoseries (M3-PALS) Malvern-ZEN 3600. ζ were taken as an average from 3 measurements and in all cases the deviation was between ±0.5 - ±1.0. The electronic absorption spectra were recorded on a Diode Array UV-visible spectrophotometer (Agilent 8453). For HRTEM studies, samples were prepared by drop casting dilute solution from the cuvette on a carbon coated Cu grid and the solvent was allowed to evaporate and specimens were examined on a FEI-Tecnai 30G^{2}S-Twin or with a 300 kV (JEOL 3010) transmission electron microscope operated at an accelerating voltage of 100 kV or 200 kV, respectively. The emission spectra were recorded on a Spex-Fluorolog, F112-X equipped with a 450W Xe lamp and a Hamamatsu R928 photomultiplier tube. The spectra were recorded by keeping a 90° geometry and a slit width of 1 nm in the excitation and emission monochromators at an exciting wavelength of 453 nm.

4.5.2. Synthesis of Au Nanorods

A growth solution was prepared by dissolving 440 mg of cetyltrimethylammonium bromide and 4.5 mg of tetraoctylammonium bromide in 15 mL of water in a cylindrical quartz tube (length 15 cm and diameter 2 cm). To this solution, 1.25 mL of 0.024 M $HAuCl_4$ solution was

added along with 325 μL of acetone and 225 μL of cyclohexane. It is reported that $AgNO_3$ is essential for synthesizing Au nanorods and controlling their aspect ratio. To the above solution, 325 μL of 0.01 M $AgNO_3$ was added for synthesizing Au rods of aspect ratio 2.2 , 400 μL of 0.01 M $AgNO_3$ was added for synthesizing Au rods of aspect ratio 3.0 and 450 μL of 0.01 M $AgNO_3$ was added for synthesizing Au rods of aspect ratio 3.7. The quartz tube was closed with a rubber stopper through which a glass rod was inserted (15 cm length and 1 cm diameter). The glass rod helps in reducing the effective thickness of the solution and increases the light absorbance. A photochemical reaction was carried out under 300 nm irradiation in a Rayonet photochemical reactor for 18 h. Gold nanorods prepared by a photochemical method were first purified by centrifugation. The residue obtained after 10 min of centrifugation (7000 rpm) was dispersed in 2 mL of 0.7 M CTAB solution and kept undisturbed for 12 h. The supernatant solution was carefully decanted and the residue was suspended in water. The solution was kept at 5 °C for 2 h to remove excess CTAB. Upon cooling, excess CTAB crystallized out which was separated by filtration. The filtrate contains monodisperse Au nanorods that were used directly for various studies.

4.5.3. Synthesis of 1.8 nm, 2.7 nm and 5.7 nm Au Nanoparticles

Au nanoparticles were prepared by adopting a place exchange reaction between the octylmercaptyl protected Au nanoparticles and triethylene glycol thiol.[30] In a typical synthesis, octylmercaptyl protected Au nanoparticles (**Au(S-C₈H₁₇)**) of 1.8 nm was prepared by following the two

phase reduction method. The product was place exchanged with 5 equivalents of triethylene glycol thiol in dichloromethane by stirring for 12 h at room temperature. The reaction mixture was evaporated to remove excess of solvent and the residue was then washed with hexane to remove unreacted triethylene glycol thiol and the product was dried. Product was then dissolved in acetonitrile and used for further studies. ^{1}HNMR studies indicate that the surface of place exchanged nanoparticles consist of triethylene glycol as capping agent (~99 %).

4.6. References

(1)   (a) Kreibig, U.; Vollmer, M. in *Optical Properties of Metal Clusters*, Springer-Verlag, New York, 1995; (b) K. G. Thomas, in *Nanomaterials Chemistry*, (Eds: Rao, C. N. R.; Müller, A.; Cheetham, A. K.), Wiley-VCH, Weinheim, Germany, 2007, p 185.

(2)   (a) Barnes, W. L.; Dereux, A. ; Ebbesen, T. W. *Nature* **2003**, *424*, 824 ; (b) Girard, C.; Dujardin, E. *J. Opt. A: Pure Appl. Opt.* **2006**, *8*, S73.

(3)   (a) Burda, C.; Chen, X.; Narayanan, R.; El-Sayed, M. A. *Chem. Rev.* **2005**, *105*, 1025; (b) Daniel, M. -C.; Astruc, D. *Chem. Rev.* **2004**, *104*, 293.

(4)   (a) Hutter, E.; Fendler, J. H. *Adv. Mater.* **2004**, *16*, 1685; (b) Maier, S. A.; Kik, P. G.; Atwater, H. A.; Meltzer, S.; Harel, E.; Koel, B. E.; Requicha, A. A. G. *Nature Mater.* **2003**, *2*, 229.

(5)   (a) Liz-Marzán, L. M.; *Langmuir* **2006**, *22*, 32; (b) Murphy, C. J.; Sau, T. K.; Gole, A. M.; Orendorff, C. J.; Gao, J.; Gou, L.; Hunyadi, S. E.; Li, T. *J. Phys. Chem. B* **2005**, *109*, 13857.

(6)   (a) Jain, P. K.; Eustis, S.; El-Sayed, M. A. *J. Phys. Chem. B* **2006**, *110*, 18243; (b) Jain, P. K.; Lee, K. S.; El-Sayed, I. H.; El-Sayed, M. A. *J. Phys. Chem. B* **2006**, *110*, 7238; (c) Eustis, S.; El-Sayed, M. A. *J. Phys. Chem.*

B **2005**, *109*, 16350; (d) Link, S.; Mohamed, M. B.; El-Sayed, M. A. *J. Phys. Chem. B* **1999**, *103*, 3073.

(7)   (a) Kelly, K. L.; Coronado, E.; Zhao, L. L.; Schatz, G. C. *J. Phys. Chem. B* **2003**, *107*, 668; (b) Haynes, C. L.; McFarland, A. D.; Zhao, L.; Duyne, R. P. V.; Schatz, G. C.; Gunnarsson, L.; Prikulis, J.; Kasemo, B.; Käll, M. *J. Phys. Chem. B* **2003**, *107*, 7337.

(8)   (a) Wang, H.; Brandl, D. W.; Nordlander, P.; Halas, N. J. *Acc. Chem. Res.* **2007**, *40*, 53; (b) Brandl, D. W.; Mirin, N. A.; Nordlander, P. *J. Phys. Chem. B* **2006**, *110*, 12302; (c) Prodan, E.; Radloff, C.; Halas, N. J.; Nordlander, P. *Science* **2003**, *302*, 419; (d) Hao, F.; Nordlander, P. *Chem. Phys. Lett.* **2007**, *446*, 115.

(9)   (a) Brioude, A.; Jiang, X. C.; Pileni, M. P. *J. Phys. Chem. B* **2005**, *109*, 13138; (b) Zhong, Z.; Patskovskyy, S.; Bouvrette, P.; Luong, J. H. T.; Gedanken, A. *J. Phys. Chem. B* **2004**, *108*, 4046.

(10)   Gluodenis, M.; Foss, C. A. *J. Phys. Chem. B* **2002**, *106*, 9484.

(11)   DeVries, G. A.; Brunnbauer, M.; Hu, Y.; Jackson, A. M.; Long, B.; Neltner, B. T.; Uzun, O.; Wunsch, B. H.; Stellacci, F. *Science* **2007**, *315*, 358.

(12)   Halliday, D.; Resnick, R.; Walker, J. in *Fundamentals of Physics*, Wiley, Weinheim, Germany, 8th Edition.

(13)   Bocquet, L. *Am. J. Phys.* **2007**, *75*, 148.

(14)   Jaramillo, T. F.; Jørgensen, K. P.; Bonde, J.; Nielsen, J. H.; Horch, S.; Chorkendorff, I. *Science*, **2007**, *217*,100.

(15)   Kou, X.; Ni, W.; Tsung, C.-K.; Chan, K.; Lin, H.-Q.; Stucky, G. D.; Wang, J. *Small*, **2007**, 3, 2103.

(16)   Pérez-Juste, J.; Liz-Marzán, L. M.; Carnie, S.; Chan, D. Y. C.; Mulvaney, P. *Adv. Funct. Mater.* **2004**, *14*, 571.

(17)   For zeta potential description, http//:www.malvern.com

(18)   (a) Lin, S.-Y.; Wu, S.-H.; Chen, C.-H. *Angew. Chem. Int. Ed.* **2006**, *45*, 4948; (b) Muller, R. H.; Jacobs, C.; Kayser, O. *Adv. Drug Delivery Rev.* **2001**, *47*, 3.

(19)   Murphy, C. J.; Sau, T. K.; Gole, A. M.; Orendorff, C. J.; Gao, J.; Gou, L.; Hunyadi, S. E.; Li, T. J. *J. Phys. Chem. B* 2005, 109, 13857.

(20)   (a) Wang, Z. L.; Mohamed, M. B.; Link, S.; El-Sayed, M. A. *Surf. Sci.* 1999, *440*, L809; (b) Wang, Z. L.; Gao, R. P.; Nikoobakht, B.; El-Sayed, M. A. *J. Phys. Chem. B* 2000, *104*, 5417.

(21)   Johnson, C. J.; Dujardin, E.; Davis, S. A.; Murphy, C. J.; Mann, S. *J. Mater. Chem.* 2002, *12*, 1765.

(22)   Nikoobakht, B.; El-Sayed, M. A. *Langmuir* 2001, *17*, 6368.

(23)   Chang, J.-Y.; Wu, H.; Chen, H.; Ling, Y.-C.; Tan, W. *Chem. Commun.* 2005, 1092.

(24)   (a) Thomas, K. G.; Barazzouk, S.; Ipe, B. I.; Joseph, S. T. S.; Kamat, P. V. *J. Phys. Chem. B* 2004, *108*, 13066; (b) Sudeep, P. K.; Joseph, S. T. S.; Thomas, K. G. *J. Am. Chem. Soc.* 2005, *127*, 6516. (c) Joseph, S. T. S.; Ipe, B. I.; Pramod, P.; Thomas, K. G. *J. Phys. Chem. B* 2006, *110*, 150.

(25)   Caswell, K. K.; Wilson, J. N.; Bunz, U. H. F.; Murphy, C. J. *J. Am. Chem. Soc.* 2003, *125*, 13914.

(26)   (a) Salant, A.; Sadovsky, E. A.; Banin, U. *J. Am. Chem. Soc.* 2006, *128*, 10006; (b) Zareie, M. H.; Xu, X.; Cortie, M. B. *Small* 2007, *3*, 139. (c) Pierrat, S.; Zins, I.; Breivogel, A.; Sonnichsen, C. *Nano Lett.* 2007, *7*, 259.

(27)   (a) Gole, A.; Orendorff, C. J.; Murphy, C. J. *Langmuir* 2004, *20*, 7117; (b) Correa-Duarte, M. A.; Pérez-Juste, J.; Sanchez-Iglesias, A.; Giersig, M.; Liz-Marzán, L. M. *Angew. Chem. Int. Ed.* 2005, *44*, 4375. (c) Grzelczak, M.; Pérez-Juste, J.; Garcia de Abajo, F. J.; Liz-Marzán, L. M. *J. Phys. Chem. C* 2007, *111*, 6183.

(28)   Kim, F.; Song, J. H.; Yang, P. *J. Am. Chem. Soc.* 2002, *124*, 14316.

(29)   Foos, E. E.; Snow, A. W.; Twigg, M. E.; Ancona, M. G. *Chem. Mater.* 2002, *14*, 2401.

(30)   Zheng, M.; Li, Z. G.; Huang, X. Y. *Langmuir* 2004, *20*, 4226.

(31)   Kelly, K. L.; Coronado, E.; Zhao, L. L.; Schatz, G. C. *J. Phys. Chem. B* 2003, *107*, 668.

(32)   Alvarez, M. M.; Khoury, J. T.; Schaaff, T. G.; Shafigullin, M. N.; Vezmar, I.;
        Whetten, R. L. *J. Phys. Chem. B* **1997**, *101*, 3706.

(33)   Bohre, C. F.; Huffman, D. R. *Absorption and Scattering of Light by Small
        Particles*, Wiley, 1983.

(34)   Hostetler, M. J.; Wingate, J. E.; Zhong, C.-J.; Harris, J. E.; Vachet, R. W.;
        Clark, M. R.; Londono, J. D.; Green, S. J.; Stokes, J. J.; Wignall, G. D.;
        Glish, G. L.; Porter, M. D.; Evans, N. D.; Murray, R. W. *Langmuir* **1998**, *14*,
        17.

(35)   Templeton, A. C.; Pietron, J. J.; Murray, R. W.; Mulvaney, P. *J. Phys.
        Chem. B* **2000**, *104*, 564.

(36)   van der Zande, B. M. I.; Koper, G. J. M.; Lekkerkerker, H. N. W. *J. Phys.
        Chem. B* **1999**, *103*, 5754.

(37)   (a) Gole, A.; Murphy, C. J. *Langmuir* **2007**, *24*, 266; (b) Gole, A.; Murphy,
        C. J. *Chem. Mater.* **2005**, *17*, 1325;

(38)   Takahashi, H.; Niidome, Y.; Niidome, T.; Kaneko, K.; Kawasaki, H.;
        Yamada, S. *Langmuir* **2006**, *22*, 2.

(39)   (a) Song, Y.; Murray, R. W. *J. Am. Chem. Soc.* **2002**, *124*, 7096; (b)
        Templeton, A. C.; Wuelfing, W. P.; Murray, R. W. *Acc. Chem. Res.* **2000**,
        33, 27.

(40)   (a) Kassam, A.; Bremner, G.; Clark, B.; Ulibarri, G.; Lennox, R. B. *J. Am.
        Chem. Soc.* **2006**, *128*, 3476; (b) Ionita, P.; Gilbert, B. C.; Chechik, V.
        Angew. Chem. Int. Ed. **2005**, *44*, 3720; (c) Montalti, M.; Prodi, L.;
        Zaccheroni, N.; Baxter, R.; Teobaldi, G.; Zerbetto, F. *Langmuir* **2003**, *19*,
        5172; (d) Stellacci, F.; Bauer, C. A.; Meyer-Friedrichsen, T.; Wenseleers,
        W.; Marder, S. R.; Perry, J. W. *J. Am. Chem. Soc.* **2003**, *125*, 328.

List of Publications:

1. Preferential End Functionalization of Au Nanorods Through Electrostatic Interactions,

   P. Pramod, S. T. S. Joseph and K. George Thomas
   J. Am. Chem. Soc. **2007**, *129*, 6712.

2. Ruthenium(II) Trisbipyridine Functionalized Gold Nanorods. Morphological Changes and Excited State Interactions,

   M. Jebb, P. K. Sudeep, **P. Pramod**, K. George Thomas and P. V. Kamat
   J. Phys. Chem. B **2007**, *111*, 6839.

3. Photochemistry of Ruthenium Trisbipyridine Functionalized on Gold Nanoparticles,

   P. Pramod, P. K. Sudeep, K. George Thomas and P. V. Kamat
   J. Phys. Chem. B **2006**, *110*, 20737.

4. Gold Nanorods to Nanochains: Mechanistic Investigations on Their Longitudinal Assembly using α,ω-Alkanedithiols and Interplasmon Coupling,

   S. T. S. Joseph, B. I. Ipe, **P. Pramod**, and K. George Thomas
   J. Phys. Chem. B **2006**, *110*, 150.

5. Plasmon Coupling in Dimers of Au Nanorods,

   P. Pramod and K. George Thomas
   Adv. Mater. (under revision).

6. Gold Nanoparticle Functionalized Carbon Nanotubes for Light Induced Electron Transfer Process,

   P. Pramod, C. C. Soumya and K. George Thomas
   ACS Nano (communicated).

Posters and Oral Presentations at Conferences:

1. Exploring the Edge Effects in Au Nanorods,
   P. Pramod and K. George Thomas

   In "*10th National Symposium in Chemistry*" by CRSI held at IISc, Bangalore, February 01-03, 2008, (**Received the Best Poster Award**)

2. Preferential End Functionalization of Au Nanorods,
   P. Pramod and K. George Thomas

   In *"Indo-Japan Cooperative Science Programme"*, held at Trivandrum, January, 20-22, 2008.

3. Gold Nanoparticle Functionalized Carbon Nanotubes for Light Induced Electron Transfer Process.

   P. Pramod, C. C. Soumya and K. George Thomas
   In *"JNC Research Conference on Chemistry of Materials"* held at Munnar, Kerala, September 28-October 01, 2007.

4. Tuning the Optical Properties of Gold Nanorods,

   P. Pramod and K. George Thomas
   In *"International Winter School on the Chemistry of Materials"* held at Bangalore, December, 12-19, 2006.

5. Chromophore Functionalized Gold Nanoparticles: Effect of Spacer, Core Size and Redox Properties.

   P. Pramod, P. K. Sudeep, K. George Thomas and P. V. Kamat
   In *"International Conference on Nanoscience and Technology (ICONSAT)"* held at Delhi, March, 16-18, 2006.